# NEARSHORE MODELLING OF LONGSHORE SEDIMENT TRANSPORT IN THE APPLICATION TO CLIMATE CHANGE STUDIES AT NINETY MILE BEACH, AUSTRALIA

**Julian George O'Grady**

**BSc (The Flinders University of South Australia)**

**This thesis is submitted in the fulfilment of the requirements for the degree of**

**Doctor of Philosophy**

**Faculty of Engineering & Industrial Sciences**

**Swinburne University of Technology**

**2018**

## Abstract

Understanding changes in the shoreline is important information used to support the planning of coastal mitigation measures for public and private infrastructure, particularly under the influence of anthropogenic climate change. It is shown that Lakes Entrance, a township located at the northern end of Ninety Mile Beach in south-eastern Australia, is situated in a region that may experience noticeable future changes in longshore winds, waves and ocean currents, which could alter the supply of sediments to the shoreline.

The goal of this study is to identify possible future changes to an improved datasets of present-day longshore transport climate. This is done by investigating bathymetric surveys and then setting-up and validating a coastal-area numerical model (TELEMAC). A Global Climate Model (GCM) downscaling method is then used to investigate the longshore transport climate of a high impact future greenhouse gas scenario.

Analysis of thirty-year model hindcast datasets of winds, coastal currents and waves are shown to agree well with available observations and provide a long-term dataset of the regional climate variability. Hindcasts of coastal ocean currents and waves indicate that while the annual net mean wave and current transport are in opposing directions, their seasonal adjusted monthly anomalies are positively correlated. Furthermore they are also correlated with the position of the Subtropical Ridge (STR) Location index. On seasonal to annual time scales a weak connection between the transport variables and Southern Oscillation Index is found.

Four GCMs are analysed in the early parts of this study and indicate a southward shift in the STR for most months under a high emission future. During Austral summer months, the STR is located over the study site. The projected change in the STR is therefore suggested to have a direct influence on longshore transport in summer months, resulting in increased westward transport normalised climate changes. During Austral winter months, the STR is remote from the study sites. Changes in winter months are less related to the STR location and it is discussed that the contraction and increased intensity of the westerly storm belt, linked to Southern Annular Mode, could possibly influence the transport. In the final parts of this thesis, downscaled sediment transport models indicate a larger monthly transport climate in winter. Consequently, the moderate normalised change in wave-driven transport during winter, has the largest impact on annual net transport.

Repeat bathymetric surveys measurements, which were conducted months apart, provides the measured variability of a larger storm-bar and trough bedform, which is controlled by storm events. These measurements are used as a bed-evolution validation dataset for numerical sediment transport modelling. Repeat multi-beam surveys show submarine dune sized bedforms moving in

the longshore direction between the 11-16m depth contours. Tracking of the dune bedform crests provided an opportunity to measure sediment transport by approximating the stoss-to-lee transport (depending on flow direction). The bedform tracking measurements, provides a plausible indication of the direction of longshore sediment transport, but differs from modelled transport by two orders of magnitude, and shows little correlation to the modelled transport magnitude.

Two types of sediment transport models are used: The simple empirical coastline-type model (CERC equation), and a detailed numerical coastal area-type model (TELEMAC). The two models resolve transport in very different ways, nevertheless came to similar conclusions on the annual net longshore sediment transport rate. The TELEMAC model, with the Soulsby-Van Rijn formulation, shows the importance of the contribution of storm events to transport. The CERC equation estimates more transport during the period between storms. The TELEMAC modelled waves, hydrodynamics and bed-evolutions are shown to agree well with the available observations.

A semi-empirical (NMB-LM) equation is designed to extrapolate the TELEMAC, storm dominated transport estimates, to the longer hindcast climate. It shows that the shorter TELEMAC modelled period had a higher storm climate, and hence twice as large net longshore sediment transport climate. The CERC equation does not pick up this difference in the different climate periods. Discussion is provided on the limitations of the models and how the projected changes could indicate sediment transport changes in the nearshore zone which could impact the coastline position.

## Acknowledgements

I would like to thank my supervisors Alexander Babanin and Kathleen McInnes for the years of support and advice. I am also truly grateful for the help, advice and friendship of my colleagues, Frank Colberg, Mark Hemer and Ron Hoeke. I would like to give a special thanks to Tony Hersbach and Andrew Francis O'Grady for their help editing this thesis.

Support for this work was provided by the Australian Climate Change Science Program, funded jointly by the Department of the Environment, the Bureau of Meteorology and CSIRO. I would like to thank Mark Spykers from Gippsland Ports for the use of the observational datasets and Tom Durrant and Claire Trenham for access to the modelled wave hindcast datasets. Thanks also go to the Victorian Government 'future coast project' for use of the LiDAR dataset and anonymous journal reviewers for their constructive comments.

The source of my inspiration came from my Mum, thank you for the instilling in me the importance of never giving up on reaching higher education. This thesis would not be possible without the love of my wife Elizabeth, and the encouragement of our family and friends.

## Declaration

I hereby declare that the thesis entitled "NEARSHORE MODELLING OF LONGSHORE SEDIMENT TRANSPORT IN THE APPLICATION TO CLIMATE CHANGE STUDIES AT NINETY MILE BEACH, AUSTRALIA", and submitted in fulfilment of the requirements for the Degree of Doctor of Philosophy in the Faculty of Engineering and Industrial Sciences of Swinburne University of Technology, is my own work and that it contains no material which has been accepted for the award to the candidate of any other degree or diploma, except where due reference is made in the text of the thesis. To the best of my knowledge and belief, it contains no material previously published or written by another person except where due reference is made in the text of the thesis.

Julian O'Grady

February 2018

Table of Contents

## List of Figures

## List of Tables

## List of Acronyms and Abbreviations

| | |
|---|---|
| **ADCP** | Acoustic Doppler current profiler |
| **ACCESS** | Australian Community Climate and Earth System Simulator (GCM) |
| **BJ1978** | Depth-induced wave breaking model |
| **CERC** | Coastal Engineering Research Center longshore transport equation. |
| **CAWCR** | Collaboration for Australian Weather and Climate Research |
| **CF** | Change Factor (downscaling method) |
| **CFSR** | Climate Forecast System Reanalysis |
| **CMIP5** | Coupled model Intercomparison Project |
| **CNPG** | Coastline Normalised Profile Grid. |
| **CNRMCM5** | National Centre for Meteorological Research (GCM) |
| **COWCLIP** | Coordinated Ocean Wave Climate Project |
| **CST** | Cross shore transport |
| **CW** | Clockwise direction |
| **CCW** | Counter clockwise direction |
| **DMG** | Dredge Material Grounds |
| **ENSO** | El Niño-Southern Oscillation |
| **GCM** | Global Climate Model or General Circulation Model |
| **GHG** | Greenhouse Gas |
| **GPS** | Global Positioning System |
| **HADGEM** | Hadley Centre Global Environment Model (GCM) |
| **IH1984** | Depth-induced wave breaking model |
| **INMCM4** | Institute for Numerical Mathematics, (GCM) |
| **ICOLLs** | Intermittently Closed and Open Lakes and Lagoons |
| **IPCC** | Intergovernmental Panel on Climate Change |
| **JONSWAP** | Joint North Sea Wave Project |
| **LiDAR** | Light Detection And Ranging |
| **LST** | Longshore transport |
| **MSL** | Mean Sea Level |
| **MSLP** | Mean Sea Level Pressure |
| **NMB** | Ninety Mile Beach. |
| **NMB-LTM** | Semi-empirical Ninety Mile Beach Longshore Transport Model |
| **RCP** | Representative Concentration Pathways |
| **RCM** | Regional Climate Model |

| | |
|---|---|
| **RMS** | Root Mean Square |
| **ROMS** | Regional Ocean Modelling System |
| **SAM** | Southern Annual Mode |
| **SISYPHE** | TELEMAC-based sediment transport model. |
| **SL, SLR** | Sea Level Rise |
| **SOI** | Southern Oscillation Index |
| **STR** | Subtropical Ridge |
| **STR-L** | Subtropical Ridge Location |
| **TELEMAC** | Suite of finite element computer program |
| **TELEMAC2D** | TELEMAC-based Two dimensional hydrodynamic model |
| **TOMAWAC** | TELEMAC-based Operational Model Addressing Wave Action Computation (wave model) |
| **UTM** | Universal Transverse Mercator coordinates. |
| **WW3** | Wave Watch three (wave model) |

**Symbol Definitions**

## Hydrodynamic variables

| | | |
|---|---|---|
| $\vec{U} = \langle u, v \rangle$ | m/s | Depth averaged velocity vector |
| $\mathrm{div}(\vec{U}) = \frac{\partial u}{\partial x} + \frac{\partial v}{\partial y}$ | - | Divergence of a vector field |
| $\overrightarrow{\mathrm{grad}}(u) = \left(\frac{\partial u}{\partial x}, \frac{\partial u}{\partial y}\right)$ | - | Gradient of a scalar field |
| $h$ | m | Depth of water |
| $x, y$ | m | Cartesian coordinates |
| $u, v$ | m/s | Velocity components in x, y directions. |
| $g = 9.8$ | $m/s^2$ | Gravitational acceleration |
| $\upsilon = 10^{-6}$ | $m^2/s$ | Kinematic viscosity of clear water |
| $\mu = \rho\upsilon$ | kg/m/s | Molecular/dynamic viscosity |
| $\upsilon_t = 10^{-6}$ | $m^2/s$ | Horizontal momentum diffusion coefficient, (molecular-viscosity plus turbulent-viscosity[eddy-diffusivity]) |
| $Z$ | m | Free surface elevation |
| $t$ | s | Time |
| $S_i = \tau_{bi} + \tau_{wi} + BC_i$ | $m/s^2$ | Source and sink terms from bottom friction $\tau_{bi}$, wave stress $\tau_{wi}$, and lateral boundary conditions, where $i$ indicates in the direction $x, y, h$ |
| $C_{dN}$ | - | Nikuradse drag coefficient |
| $\rho = 1020$ | $kg/m^3$ | Water density |
| $k_{sN} = 0.05$ | m | Tuneable bed roughness coefficient |

## Spectral wave variables

| | | |
|---|---|---|
| $\tilde{F}(x, y, f_r, \theta, t)$ | $m^2/s/rad$ | Directional variance spectrum |
| $f_r$ | Hz or 1/s | Spectral relative wave frequency |
| $\theta$ | rad | Spectral wave propagation direction in radians |
| $\tilde{Q}(x, y, f_r, \theta, t)$ | $m^2/s^2/rad$ | Source and sink terms. |
| $\vec{V} = \langle \dot{x}, \dot{y}, \dot{f_r}, \dot{\theta} \rangle$ | $<m/s, m/s, s^{-2}, rad/s>$ | Transfer rates by currents |
| $\tilde{B} = \frac{c_g}{(2\pi)^2 k f_r}$ | $m^2$ | Factor to express $\tilde{Q}$ in terms of $\tilde{F}$ |
| $c_g = n\frac{\sigma}{k}$ | m/s | Wave group speed |

| | | |
|---|---|---|
| $n = \frac{1}{2}\left(1 + \frac{2kh}{sinh\,2kh}\right) = \frac{c_g}{c}$ | - | Ratio of group ($c_g$) to phase speed ($c$) |
| $\sigma = \omega - \vec{k} \cdot \vec{U}$ | rad/s | Relative angular frequency |
| $\omega = 2\pi f$ | rad/s | Absolute angular frequency |
| $k = \frac{2\pi}{L}$ | $m^{-1}$ | Wave number |
| $L = \frac{2\pi g}{(2\pi f_r)} \tanh\left(\frac{2\pi h}{L}\right)$ | m | Wavelength from dispersion relation |
| $\vec{k} = \langle k_x, k_y \rangle$ $= \langle k \sin\theta, k\cos\theta \rangle$ | m | Wave number vector |
| $\dot{x}, y^{\cdot}$ | m/s | Transfer x and y coordinates |
| $\dot{f_r}$ | Hz/s or $1/s^2$ | Transfer frequency by Doppler effect due to non-zero currents. |
| $\dot{\theta}$ | rad/s | Transfer propagation directions by refraction from bathymetry (1st term) and currents (2nd term) |
| $\overrightarrow{G_N} = \langle \cos\theta, -\sin\theta \rangle$ | - | Normal vector |
| $\overrightarrow{G_T} = \langle \sin\theta, \cos\theta \rangle$ | - | Tangential vector |
| $H_s = H_{m0} = 4\sqrt{m_0}$ | m | Spectral significant wave height |
| $m_0 = \int_{f_r=0}^{\infty} \int_{\theta=0}^{2\pi} \tilde{F}\, \mathrm{d}f_r \mathrm{d}\theta$ $= \int_{f=0}^{2\pi} S\, \mathrm{d}f$ | m | Zero order moment of the spectrum |
| $f_c = \frac{\int_{f=0}^{\infty} f S^5\, \mathrm{d}f}{\int_{f=0}^{\infty} S^5\, \mathrm{d}f}$ | Hz | Intrinsic peak frequency from Read's method to order 5 |
| $T_p = 1/f_c$ | s | Peak wave period |
| $\theta p$ | rad | Wave direction associated with the peak spectral energy, clockwise from true north |
| $\tilde{Q}_{bf}$ | $m^2/s^2$/rad | Bottom friction-induced energy dissipation |
| $\tilde{Q}_{bb}$ | $m^2/s^2$/rad | Bathymetric-induced breaking energy dissipation |
| $\tilde{Q}_{cb}$ | $m^2/s^2$/rad | Current-induced breaking energy |
| $\tilde{Q}_{tr}$ | $m^2/s^2$/rad | Non-linear triad (three wave) interactions |
| $\Gamma = 0.038$ | $m^2/s^{-3}$ | JONSWAP constant |
| $H_m$ | m | Maximum wave height |

| | | |
|---|---|---|
| $\gamma$ | - | Depth-induced wave breaking parameter |
| $Q_b$ | - | The fraction of breaking waves |
| $T_{ii}$ | $m^3/s^2$ | Wave radiation stress tensor in the ith (x or y) coordinate |
| $\tau_{wi}$ | $m/s^2$ | Wave radiation force in the ith (x or y) coordinate |
| $U_o$ | m/s | Wave, near-bed orbital velocity |
| $\theta_i$ | rad | Incident wave angle CW from shore nomal angle. |
| $\theta_N$ | rad | Angle of the shore normal (CW from North) |
| $\theta_R$ | rad | Angle of the coastline CCW from the UTM x axis |
| $U_L = \vec{U} \cdot \langle cos\theta_R, sin\theta_R \rangle$ | m/s | Longshore current velocity (scalar projection) |

## Sediment transport variables

| | | |
|---|---|---|
| $q_T$ | $m^3/m/s$ | Total volumetric sediment transport rate per unit width of the bed in the direction of flow |
| $\overrightarrow{q_T} = q_T \frac{\vec{U}}{\lvert\vec{U}\rvert}$ | $m^3/m/s$ | Total volumetric sediment transport rate $q_T$ vector. |
| $q_{T,L} = \overrightarrow{q_T} \cdot \langle cos\theta_R, sin\theta_R \rangle$ | $m^3/m/s$ | Total volumetric sediment transport rate $q_T$ in the longshore direction. (scalar projection) |
| $Z_f$ | m | Bottom elevation |
| $\phi = 0.4$ | - | Bed porosity |
| $q_b$ | $m^3/m/s$ | Bedload sediment transport rate per unit width of the bed |
| $q_s$ | $m^3/m/s$ | Suspended sediment transport rate per unit width of the bed |
| $A_b$ | - | Bedload transport coefficient |
| $A_s$ | - | Suspended load transport coefficient |
| $U_{cr}$ | m/s | Critical sediment entrainment/mobility speed |
| $C_{dS}$ | - | Soulsby drag coefficient |
| $k_{sS} = 0.006$ | m | Soulsby bed roughness length |
| $P_i$ | - | Spatially varying available sediments from each class |
| $d_{50,i}$ | m | Median grain size within each class (i) |
| $D_{50}$ | m | Median grain size |
| $D_{90}$ | m | $90^{th}$ percentile grain size. |
| $D_*$ | - | Non-dimensional grain diameter |

| | | |
|---|---|---|
| $\rho_s = 2650$ | kg/m$^3$ | Sediment density |
| $Q_w$ | m$^3$/s or m$^3$/yr | CERC derived longshore transport per width of surf zone |
| s=2.6 | - | Ratio of sediment to water density |
| $Q_{wu}$ | m$^3$/s | NMB-LM derived longshore transport per width of surf zone |
| $\delta$ | - | Symbol indicating time interval transport has been intergrated or accumulated over a, e.g. between surveys |
| $K_s$ | - | CERC transport coefficient |
| $\theta_\Delta$ | rad | Wave-transport-directional CF |
| $D_i$ | - | Calibrated values of the NMB-LM |
| $\lambda$ | m | Bedform wavelength, between troughs |
| $Ty_i$, $Tz_i$ | m | Bedform trough longshore location and depth |
| $Cy_i$, $Cz_i$ | m | Bedform crest longshore location and depth |
| $h_B$ | m | Bedform height |
| $\Lambda$ | - | Bedform asymmetry |
| $V_{err} = V_{dep}$ | m$^3$ | Bedform volume eroded and deposited |
| $q_v$ | m$^3$/m/yr | Bedform identified sediment transport rate per unit bedform crest length. |
| $Q_v$ | m$^3$/yr | Bedform identified longshore sediment transport rate per width in cross-shore direction |

## Climate analysis variables

| | |
|---|---|
| $A$ | Normalised climate model anomalies, for winds, waves and currents. |
| $F_i$ | Future period, subscript '*G*' is for GCM derived, subscript '*H*' is for hindcast derived, subscript '*U*' is for coastal currents, '*Q*' is for wave-transport., '*M*' is for monthly mean and '*A*' is for annual mean. |
| $B_i$ | Baseline period, has the same subscripts as the future F variable. |

# 1. INTRODUCTION

The nearshore zone is situated at the intersection of the coastal-ocean and beach zones (Figure 1.1 and Figure 1.2). It can be defined by the location of strong depth-induced dissipation processes of wind-driven surface-gravity waves, which have periods less than approximately 30 seconds. In the rest of this document these are referred to simply as ‘waves’. The seaward extent of the nearshore zone is the approximate depth of significant morphodynamic activity from the effect of waves, which is referred to as the closure depth. The closure depth is just seaward of the point where the largest storm waves break due to shallowing water depths and drive flow. The landward boundary is the location that swash can reach up the beach-face from the contribution of; 1) individual waves (runup), 2) time-averaged setup of infragravity waves with periods greater than 30s (setup), 3) astronomical tide, 4) coastal atmospheric-driven storm surge and 5) steric sea level (Figure 1.1). The nearshore zone covers many time scales of fluid processes, including laminar flow and non-linear turbulence.

When waves approach the coastline at an oblique angle, they dissipate in the shallowing water and create a force in the direction parallel to the shoreline, which if strong enough can result in longshore sediment transport (Figure 1.2). Longshore sediment transport is a combination of; 1) Longshore currents driven by these depth-induced wave forces, as well as tidal and wind driven flow and 2) Beach drift from the swash action of individual waves running up and falling the coastline at an angle in a zig zag pattern (Figure 1.2).

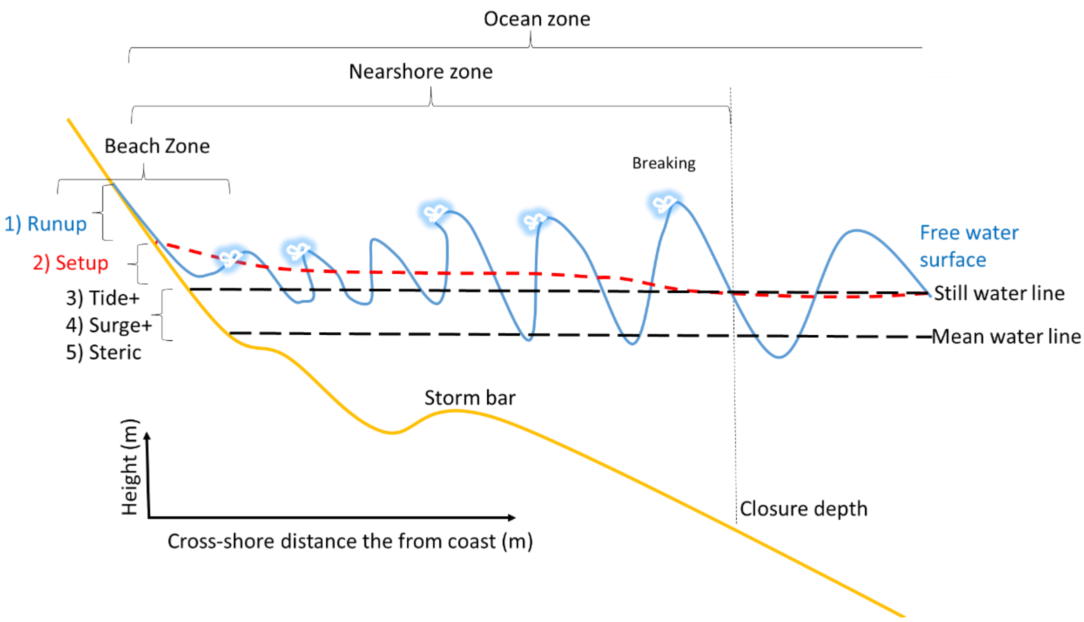


**Figure 1.1. Cross-shore diagram of the nearshore zone.**

In the text above the nearshore is defined by the location of strong depth-induced dissipation processes of waves. The diagram shows a cross-section of the bathymetry (yellow line), example locations of breaking waves (blue line) and the contributors to landward reach of the water up the beach (dashed lines).

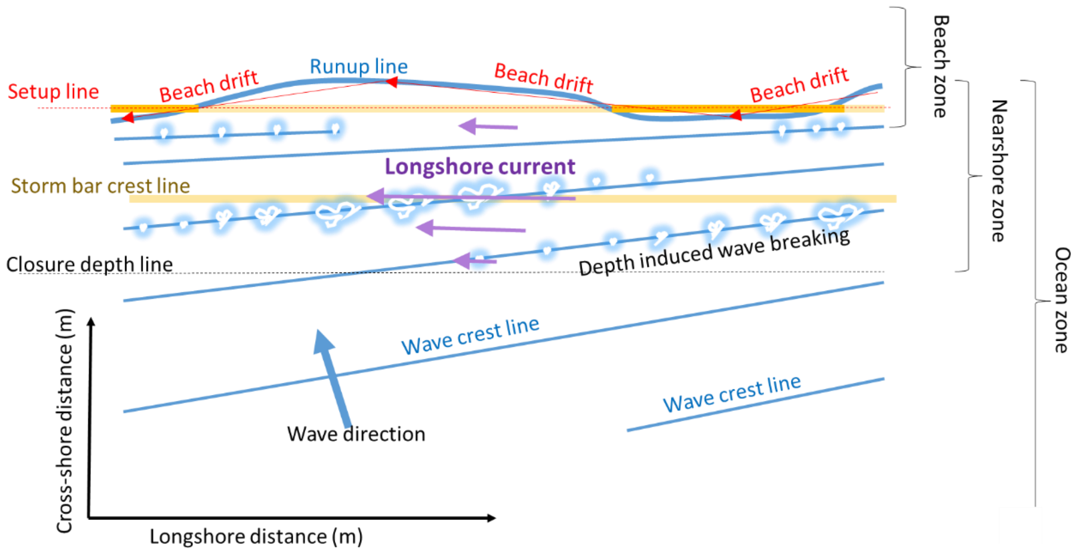


**Figure 1.2. Map diagram of the nearshore zone and longshore transport.**

Map view of nearshore zone corresponding to Figure 1.1. Waves (blue crest lines) approaching from the bottom-right, refracting towards the coastline, dissipating (white squiggles) on the storm bar and shoreline generating a longshore current to the right (purple arrows). The runup line (thick blue line) at the top shows the landward extent of the nearshore zone, and the zig zag pattern of the beach drift (red arrows).

## 1.1 Motivation

The motivation for studying the processes within the nearshore zone is to be able to understand what is controlling shoreline position. Understanding and predicting changes in the shoreline is important information used to support the planning of coastal mitigation measures for public and private infrastructure from severe storms, particularly under the influence of anthropogenic climate change (Wong et al., 2014).

The global scientific community has come to a consensus: "Warming of the climate system is unequivocal. Since the 1950s, many of the observed changes are unprecedented over decades to millennia. The atmosphere and ocean have warmed, the amounts of snow and ice have diminished, and sea level has risen… [greenhouse gas] effects, together with those of other anthropogenic drivers, have been detected throughout the climate system and are *extremely likely* to have been the dominant cause of the observed warming since the mid-20$^{th}$ century" (IPCC, 2014).

Governments around the world are working to mitigate the global change effects from future high greenhouse gas (GHG) concentrations. However, some risks from climate damages are unavoidable, even with mitigation and adaptation (IPCC, 2014). Predicting the possible local changes as a result of anthropogenic climate change is challenging as it relies on foreign influences within a global connected climate system to resolve localised effects.

The study site, Ninety Mile Beach, has significant financial and environmental value (Russell et al., 2013). The intention of this thesis is to investigate the upper limit of GHG concentration forced global change at a region that has been identified to have a larger Global Climate Model (GCM) predicted change than the global average. The thesis steps through the process of downscaling the GCM change signal to the nearshore zone by applying a sediment transport model and simulating a future scenario of the transport change. Furthermore, the accuracy of the sediment transport model and the uncertainty in this simulated scenario, will be detailed and quantified at each stage of the investigation. This process will provide evidence towards understanding the potential impact of climate change at the local scale.

## 1.2 Global Climate Change Models

A global climate model or general circulation model (GCM) simulates the dynamic interactions of the atmosphere, oceans, land surface and ice from radiative forcing, to represent the Earth's climate. GCMs are used to simulate possible future climates from changes to the radiative forcing. The complexity of simulating the Earth's climate means that there can be multiple GCM outcomes, which can be used to measure model uncertainty. The uncertainty measurement provides a probabilistic indication of the outcomes for impact assessment.

A GCM employs mathematical equations to simulate the general circulation of a planetary atmosphere or ocean. Circulation in the atmosphere and ocean are predicated on numerical approximations of the Navier-Stokes partial differential equations (PDE). These are solved using a three dimensional grid over the globe. This grid typically has a horizontal resolution of between 100 and 150 km, 10 to 20 vertical layers in the atmosphere and sometimes as many as 30 layers in the ocean. At this coarse resolution many small-scale physical processes cannot be directly resolved. These include vertical convection and cloud formation, where simplified equations (parametrisations) are used to capture the processes at the sub-grid scale. These equations are based on measured relationships (empirical equations) or theoretically modelled relationships (semi-empirical equations). Parametrisation is one source of uncertainty in GCM ensemble simulation. This uncertainty can be readily quantified because different modelling groups around world have used slightly different parametrisations in their mode simulations, submitted to the fifth phase of the Coupled model Intercomparison Project (CMIP5).

GCM simulations conducted in the CMIP5 experiment were also run with different future Representative Concentration Pathways (RCP) scenarios. These were based on the historic greenhouse gas concentrations and their residence in the system and possible future GHG emissions (and GHG removal from the system). Multiple future estimates of GHGs concentrations in the global system is another major source of uncertainty in GCM simulations.

Investigation of future projected GCM impacts at the local scale requires some method of adjusting the large-scale gridded GCM-predictions down to the small-scale, a process known as downscaling (Fowler *et al.*, 2007). There are different approaches to downscaling GCM data, each with a different level of complexity and accuracy:

1) *Dynamical downscaling* utilises a direct time series of gridded GCM output to force a high resolution nested GCM (or RCM). The RCM can then be coupled to other models (e.g. waves and sediment transport) to resolve processes not directly modelled by the GCM. This processes produces the most resolved recreation of historic (baseline) and future climates.
2) *Statistical downscaling* uses a simpler method by taking the observed spatial pattern of variability and applies statistical techniques to infer local-scale changes from large-scale changes generated by GCMs.
3) The *Change Factor* (CF) *downscaling* method is the simplest method. It takes a time series of the observed climate and applies an offset based on the difference between the models future and baseline mean periods. The CF method is usually a single value of

change applied to the observed time series, but could be applied as a seasonal or monthly mean change value.

## 1.3 Sediment Transport Processes

Sediment moves in coastal waters under the action of waves or currents (wind-, wave- or tide-driven) or both. Sediment processes can be explained by *entrainment*, *transportation* and *deposition*, which can occur at the same time and may interact with each other (Soulsby, 1997):

1) *Entrainment* is a result of wave and/or current friction mobilising the weight and structure of the stationary sediment on the seabed.
2) *Transportation* moves the sediment by rolling, hopping and sliding along the seabed (bedload transport). Alternatively if the action is strong enough sediment will be lifted into the water column and will move with the flow (suspended load transport).
3) *Deposition* occurs when wave and/or current action is reduced and the sediment comes to a rest (bedload) or settles out of suspension (suspended load).

Shoreline position can be defined as the boundary of land and water that varies with tidal and seasonal storm climate. The primary driver of the seasonal change in position is wave action, followed by the coincidence (or added effect) of tides and storm surge. These effects along with bedform features (e.g. bar and trough) can be used to classify beach type (Short, 2006; Wright and Short, 1984). Furthermore, sediment transport is also controlled by natural features including headlands, channels and estuaries and man-made structures within the coastal zone (Figure 1.3). These include breakwaters, groynes and channel entrances, used to control erosion processes, including beach drift, to maintain shoreline position.

Considering a natural, uninterrupted beach coastline, the sediment transport processes extend from the beach dune out to deep water. These transport processes can be better explained by separating transport into orthogonal components in the *cross-shore* and *long-shore* directions. Cross-shore transport processes can rework the shore-face (surf zone and beach) profile to result in a steeper or gentler profile as a response to changing sea levels or wave energy climates. The position of the shoreline can either be maintained, or shift accordingly. Longshore transport by wind, wave and storm-tide flow can control the long-term availability of marine sediments within a coastal section. This will either nourish or deplete the near-shore profile and in turn impact the shoreline position.

The ability of sediments to be reworked within a section of beach also depends on what offshore depth sediments can be reworked by different climate forcing, referred to as the active closure depth (Nicholls et al., 1998). In engineering practice the depth of closure is fixed for a return-level wave height given the design life of a structure. For longer climate change studies under which future changes are the consequent global GHG concentrations, the depth of closure will be time dependent on sea level rise and changes in extreme events. Depending on the change, more sediments from deeper water could supply sediments to the shore. Conversely, sediments near the active closure depth could be separated from the active sediment region.

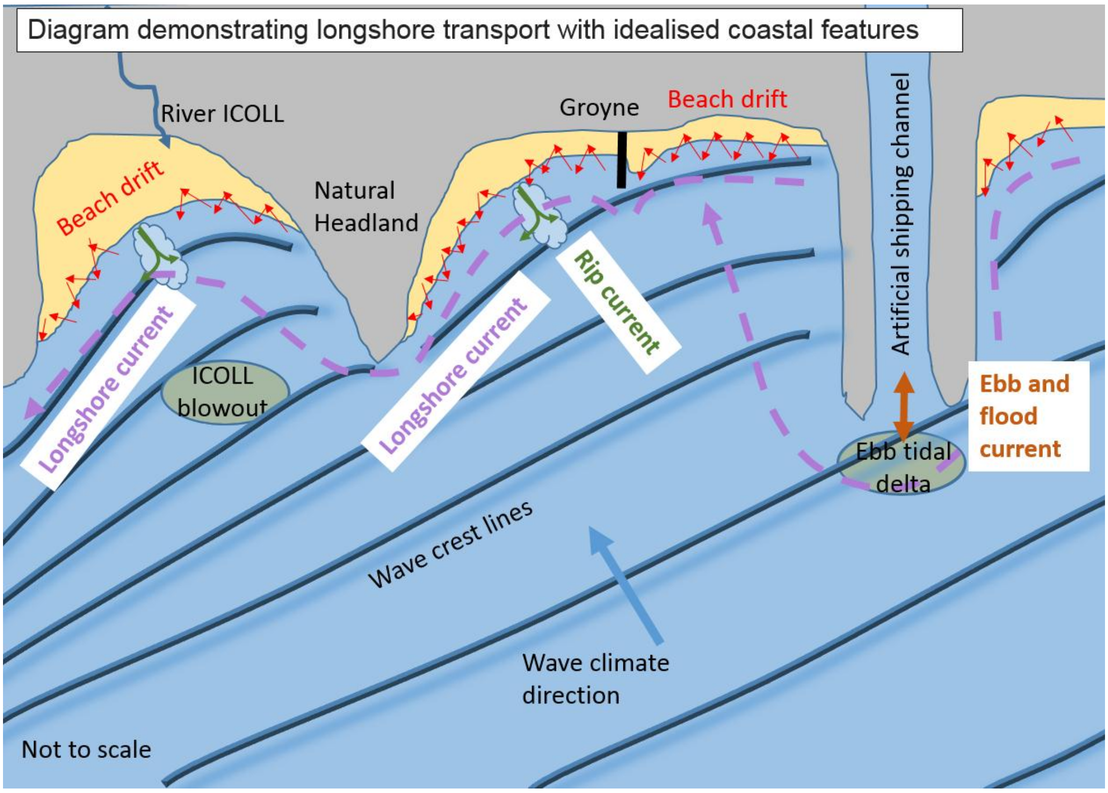


**Figure 1.3. Diagram of the longshore transport for a complicated coastline.** Longshore transport is shown here for a wave climate approaching from the bottom right, pushing sediment towards the left along the shore face (beach drift) in a zig zag pattern (red arrows) and below the water surface (longshore current) following the contours of the coastline (purple dashed lines and arrows). Directly incident waves onto the shoreline can generate rip currents (green arrows), ebb and flood channel currents (brow arrows) can generate a delta deposit and large river flow (blue arrow) can 'blow out' an ICOLL and deposit sediments offshore.

The size and distribution of sediments is also critical in determining the transport mobility. The orbital motions under wave and laminar flow can generate bedforms. The bedforms can then in turn interact with the transport processes by increasing friction (Nielsen, 1992).

Although observations of sediment transport in nearshore waters are difficult to acquire, they have been measured by fluorescent tracers, inferred grain-size trend analysis techniques, acoustic or optical backscatter instruments and sediment traps (Cartier *et al.*, 2012; Tonk, 2004). Larger bedforms on the seabed (length scale of tens-of-metres and high scale of tens of centimetres; dunes) can be tracked in repeat surveys and can also provide evidence of transport direction (Duffy and Hughes-Clarke, 2012).

## 1.4 Sediment Transport Models

For practical application, mathematical modelling of sediment transport relies heavily on parametric equations to solve the chaotic behaviour of sediment particles. Working from the basis of extensive empirical research for river flows, both *empirical* and *semi-empirical* equations have been formulated since the 1970s to include the theory of wave effects on transport. Empirical equations are designed to represent the simplest mathematical representation of an observed process, in the form of a time-series or statistical relationship. Semi-empirical equations can be derived as a simplified form of complex mathematical simulation based on scientific theory. When these equations are tested against flume and tank experiments (real and virtual), many different formulations are generated. When these equations are applied to field studies questions that need to be considered are: 1) How scalable are tank experiments when applied to field studies? 2) Have all wave-flow-sediment processes have been observed? 3) Have extreme weather conditions been observed? The parameters of the equations are found (calibrated) by fitting (optimising) the equation to the *in situ* field observations, tank experiments or high-resolution model output. As a result, simplified empirical equations using basic wave and morphological parameters require high quality observations and extensive calibration to define the true sediment transport at a given field location. When a calibrated equation is applied to different coastlines around the world, it will need to resolve the differing contribution of wave and current processes to sediment transports and have the ability to resolve unforeseen processes and effects, such as changes in bed slope.

With more computer power, the numerical solutions to the Navier-Stokes PDEs (numerical models) are able to solve fluid process to higher and higher resolutions. However, there is a limit to how small the time step can be physical processed on computers. Numerical models represent a more dynamic solution and can solve transport processes in more detail. However, there remains a conundrum: numerical PDE models still require the use of empirical equations to resolve the physical sediment transport process for large-scale coastal studies. Similarly, like the parametrisation in GCMs, empirical equations are a source of uncertainty in model prediction.

Numerical models can take on many forms, from 1D-profile modelling, to 2D-depth averaged Navier-stokes to 3D-Navier-Stokes, each with its own advantage of resolving the physics flow at the expense of computational resources. A clear distinction between empirical equations (used on their own) and PDE numerical modelling is that the latter is able to resolve the updating of the seabed evolution (e.g. Exner PDE). This method takes into account transport budgets and seabed evolution (erosion and accretion). The situation could arise where empirical models could estimate the longshore transport of sediment for many years. In reality, the source of sediments could be exhausted after one year, so no transport is a distinct possibility after one year in reality. While the numerical method is more sophisticated in managing this transport budget, it has the added complexity of cumulative transports errors creeping into the solution. This is another source of internal model uncertainty in the prediction.

## 1.5 Scope of the Study and Thesis Outline

The goal of this study is to better resolve the present-day longshore transport climate by, investigating bathymetric surveys and then setting-up and validating a coastal-area numerical model. The model is then used to investigate the longshore transport climate of a high impact future GHG scenario.

The thesis is woven around three themes and divided into eight chapters. The three themes are: 1) *climate variability and climate change*, 2*) morphology and morphodynamics* and 3) *sediment transport models*. The key discussion points for each theme are summarised for each chapter in Table 1-1. The objectives of each chapter is outline below:

- *Chapter 1* introduces the motivation and three organising themes.
- *Chapter 2* provides a review of the scientific literature and identifies the research gaps that are then explored throughout the thesis (i.e. Chapters 3-8).
- *Chapter 3* compiles the relevant dataset (measured and modelled) to describe the climate. It then goes on to detail the modelling and analysis methodology.
- *Chapter 4* provides the analysis of longshore transport parameters from a ~30 yr hindcast and 2 x ~20yr GCM. This chapter focuses on the following research questions:
    - How do the modelled climates compare to the measured?
    - What is the longshore wave and current (wind- and tide- driven) climate? What are the climate drivers/indices (e.g. sub-tropical ridge location, Southern Oscillation Index) influencing the variability?
    - What is the projected change? Does it vary seasonally? What is causing the change?
- *Chapter 5* provides an analysis of two bathymetric survey types. The first analysis is of a large-scale survey to quantify the *spatial variability* of the cross-shore profile along the entire Ninety Mile Beach (NMB) coastline. The second analysis of repeat surveys of the profile near Lakes Entrance to quantify *the temporal variability* of the profile. This chapter focuses on the following research questions:

- Can analysis of repeat survey provide a validation dataset for the modelling of bed evolution?
- Do bedforms move between repeat surveys and can they predict the transport magnitude and direction?

- *Chapter 6* explores the internal model sensitivity within the setup of the ~3.7 yr TELEMAC simulations and compares the model predictions with the validation datasets from the previous chapter (surveys) and Chapter 3 (*in situ* instruments). This chapter focuses on the following research questions:
  - What is the best way to nest TELEMAC in the hindcast wave and current (wind- and tide- driven) simulations?
  - What is the effect of including waves in the hydrodynamic simulations?
  - How do different formulations of depth-induced wave breaking effect sediment transport?
  - What is the modelled transport sensitivity of different sediment characteristics?
  - What is the spatial pattern of transport and net estimate of transport over the ~3.7 yr TELEMAC simulated period?
  - How does TELEMAC compare with empirical equations (e.g. CERC)?
  - Can a new semi-empirical equation, tuned to TELEMAC ~3.7 yr results, extrapolate transport to the ~30 yr hindcast datasets? What is the full ~30 yr hindcast transport climate?
- *Chapter 7* utilises the validated models in the previous chapter with the GCM predicted climate downscaled values to predict future climate change. This chapter focuses on the following research questions:
  - What is the effect of re-running the ~3.7 yr TELEMAC simulations with increasing water levels as an analogue to sea level rise?
  - What is the effect of rerunning the ~3.7 yr TELEMAC simulations with modified wave and current (wind and tide drive) forcing as an analogue to the longshore transport changes predicted by the GCMs?
  - How does the ~3.7 yr TELEMAC re-run simulations compare to empirical equations with the change values? What is the change predicted using the 30 yr hindcast and the empirical equations?
- *Chapter 8* addresses and summarises the key findings from the thesis.
- *Chapter 9* discusses the wider implications of this work and recommends avenues for future work.

**Table 1-1 Summary layout of the thesis chapters.**

The main points listed for each chapter are categorised into three key themes (column headings). Theme and thesis results are highlighted in bold boxes.

| Chapter | | Climate variability & change | Morphodynamics | Sed.-transport models |
|---|---|---|---|---|
| **1** | Introduction | IPCC, GCM & RCPs | Cross-shore and long-shore processes | Empirical & PDE equations |
| **2** | Literature review | Regional climate SE- Australia | Geology of NMB | Profile- coastline- area- models. TELEMAC |
| **3** | Measurements, data & method | Observations, Hindcast, GCM | Repeat surveys, bedform tracking | TELEMAC: Source terms & boundary conditions. CERC eq. |
| **4** | Climate variability & change | **Longshore wave & flow GCM & GCM projection** | | CERC empirical transport equation |
| **5** | Morphology Morphodynamics | | **Temporal- spatial- var. of NMB. Meas. transport** | |
| **6** | Sediment-model hindcast | | Validation data | **TELEMAC sensitivity and accuracy. New empirical eq.** |
| **7** | Sediment-model climate sims | **CF Downscaled GCM Transport.** | | Validated TELEMAC & new empirical eq. |
| **8** | Conclusion | From Chapters 4, 6 & 7 | From Chapters 5,6 | From Chapters 6, 7 |

# 2. LITERATURE REVIEW

This chapter reviews the published scientific literature detailing the transport climate of the study site and its geological history. It then provides a review of sediment transport modelling and goes on to introduce the model selected for the investigation.

## 2.1 Drivers of the Longshore Transport Climate in South-Eastern Australia

Ninety Mile Beach (NMB) is a 144 km long barrier dune system located in south-eastern Australia bounded on its western side by Wilsons Promontory (Figure 2.1). Corner Inlet, a system of sandy tidal flats situated on the eastern side of Wilson's Promontory, acts as a geological sediment reservoir for NMB. At the eastern end of the beach is a man-made ocean entrance to the Gippsland Lakes, located at the township of Lakes Entrance (Figure 2.1).

The channel connecting the Gippsland Lakes to Bass Strait was first opened in 1889 (Figure 2.2) and has established a flood tide delta which requires ongoing dredging to maintain the passage of fishing vessels to the largest fishing port in the state of Victoria (Wheeler et al., 2010). The coastline on the ocean side of the entrance is highly dynamic, changing over the time scales of a storm, season or a few years and can be controlled by marine formations such as temporary nearshore bars, observed to move up to 10 m per day (Wright et al., 1982). The appearance of bars can reposition the dissipation of the wave energy across the surf zone to positions away from the beach face.

Ocean waves are able to mobilise and suspend and transport sediments along and on- or offshore and therefore are the main driver of sediment transport in the littoral zone. Large-scale interannual atmospheric changes can cause significant wave climate and coastline changes. For example, a positive trend in the Southern Annual Mode (SAM) over the past two decades, (amounting to a strengthening and poleward shift of the extratropical cyclone storm track; Thompson and Solomon, 2002), has been associated with a positive trend in significant wave heights (*Hs*) in the southern ocean (Hemer et al., 2009; Young et al., 2012) with subsequent impacts along the Western Australian coastline (Bosserelle *et al.*, 2011; Wandres *et al.*, 2017). Variations in both the SAM and the El Niño Southern Oscillation (ENSO) have been shown to influence wave climate and coastline orientation within embayments in eastern Australia (Harley et al., 2010; Ranasinghe et al., 2004).

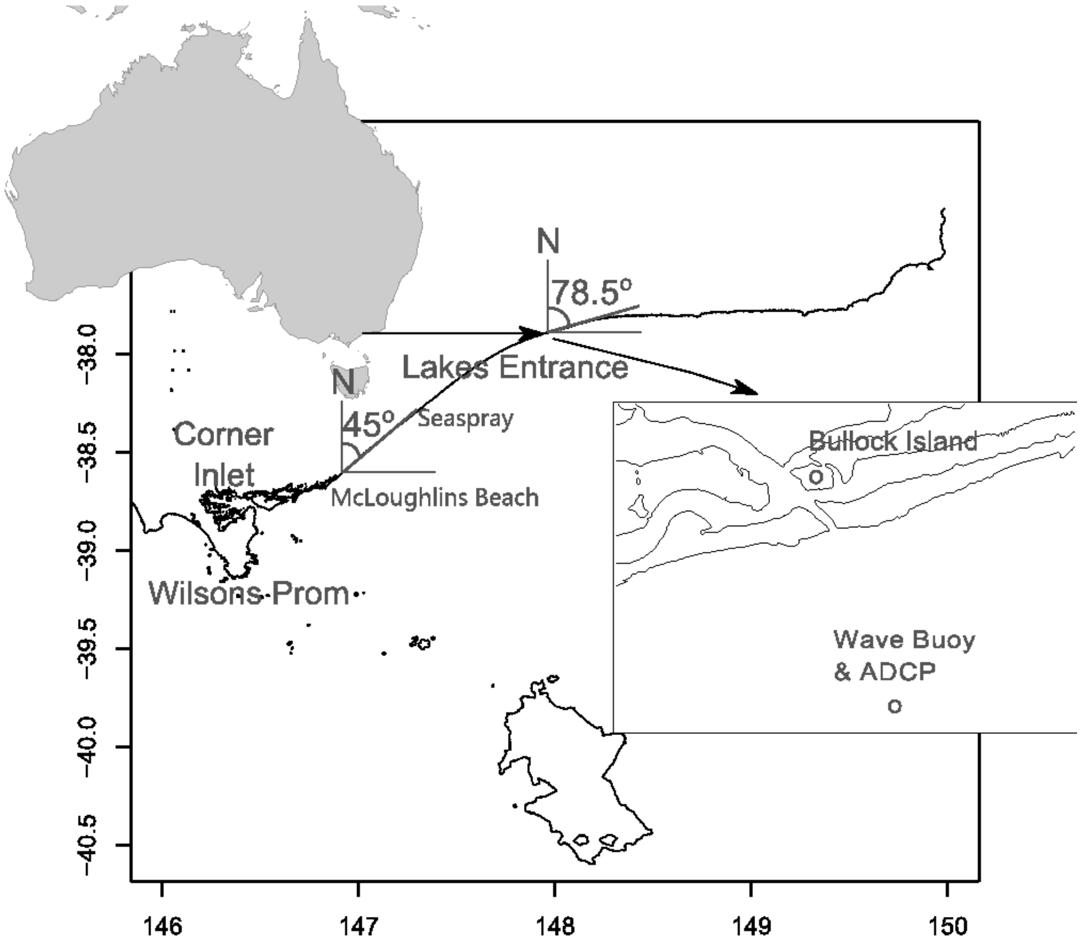


**Figure 2.1. Map of Ninety Mile Beach (NMB) with the horizontal arrow indicating its location on the Australian mainland southeast coast.**
The insert shows detail of Lakes Entrance and the location of the wave and current measurements. The coastline angle relative to true north, used in longshore energy flux calculations, is also indicated.

**Figure 2.2 Photograph of the newly constructed breakwaters and breaching of the Gippsland lakes, *circa* 1890.**

The Dredge Wombat (centre-left) cutting through the barrier dune from the ocean side (top right), between the two newly constructed breakwaters. Source: State Library of Victoria, circa 1890.

The southern hemisphere subtropical ridge (STR) is a large-scale climate feature defining the latitudinal boundary of the easterly trade winds to the north and the westerly storm belt to the south and is situated at approximately 30°S in the austral winter and 40°S during austral summer (Kent et al., 2011). The sub-tropical ridge is related to the frequency and strength of the extra-tropical storms and frontal systems (Kent et al., 2011) that occur in the region, which in turn relate to wave and storm surge conditions in Bass Strait (McInnes and Hubbert, 2003; O'Grady and McInnes, 2010). The location of the STR between about 40°S to 38°S in eastern Bass Strait in summer (fig 1) suggests that changes in the position of the STR as a result of climate change could lead to large changes in wind regime in this region. For example, Global Climate Model (GCM) simulations indicate that by the end of the century under a high greenhouse gas emission scenario, a decrease in mean westerly wind and waves at latitudes just south of the ~30°S STR line, in association with a southward contraction and intensification of the southern ocean storm belt could occur (Hemer et al., 2013c; McInnes et al., 2011). Hemer et al., (2013a) show that future increases in wave height in the Southern Ocean adjacent to the study area are some of the most robust projected changes over the 21st Century in current global wave climate projection studies. In the centre of eastern Bass Strait, where high wave events are most commonly caused by westerly winds (O'Grady and McInnes, 2010), a future shift in the STR could change the balance between easterly and westerly winds to one of a reduced westerly and increased easterly mean wind climate with subsequent impacts on the nearshore wave climate. Such changes could lead to a regime shift in sediment movement along this coast. In general, extreme winds which drive transport are anticipated to be similar to changes in mean wind changes (CSIRO and Bureau of Meteorology, 2015).

Coastal currents associated with the combination of astronomical tides (tide) and meteorological forcing (together referred to as wind-tide currents) further contributes to the transport of sediments. Previous modelling studies indicate strong wind-tide- driven currents in Eastern Bass Strait (Fandry, 1983; Sandery and Kämpf, 2007). Attempts have been made to estimate climate change impacts of sediment transport from wave energy for NMB (Charteris and Sjerp, 2009) but have been limited due to lack of available observational data and have not included the influence of the considerable wind-tide currents in this region.

The direction and magnitude of longshore sediment transport along NMB has been debated as there are no long-term observations (Wheeler et al., 2010). NMB has experienced significant changes to the position of the coastline in the past (Riedel and Sjerp, 2007). Analysis of aerial photography shows parts of the coastline at the western end of NMB (McLoughlins Beach to Seaspray) has exhibited periods of both retreat and advance over a few surveys (two or three depending on the section of coastline) spanning the years 1941 to 2006. It is also worth noting that over this 64-year period global mean sea level has risen on the order of 0.12 m (Church and White, 2011), yet this has not resulted in a continued six to 12 meters of shoreline retreat that is predicted by the Brunn Rule (Bruun, 1962). This suggests that other processes in addition to rising sea levels are influencing the coastline response in this region.

Sea level rise has been considered the defining driver of coastline change with long-term climate change since the inception of the simple assumption of maintaining the cross-shore profile (Bruun, 1962). While important, some recent regional studies have shown longshore transport to be more important to barrier erosion than sea level rise, e.g. for the Danish North Sea coast (Aagaard and Sørensen, 2013), and on the Florida coast in the U.S. (Houston and Dean, 2014) where coastlines have advanced (accreted) instead of retreated at a rate that would be attributable to recorded sea level rise.

A recently developed thirty-year hindcast of ocean waves (Durrant et al., 2014) and updated hydrodynamic simulations to those reported in Colberg *et al.*, (2017) provide an opportunity to view the long-term variability of the currents and waves beyond the few years of the *in-situ* direct measurements at NMB. Further to this, future projected changes in waves (Trenham et al., 2013) and hydrodynamics have been determined using GCM forcing from a subset of IPCC CMIP5 models (Taylor et al., 2012).

## 2.2 Geology of Ninety Mile Beach

The underlying geomorphic foundation of the Gippsland Basin is attribu*ted to* the rifting of Australia and Antarctica, which opened the Southern Ocean and Tasman Sea during the late Cretaceous and early Tertiary periods ~ 60Ma (Harris et al., 2005; Mitchell et al., 2007). The rifting also caused the crust on the Australian continent to thin and this thin-crust was warped by the hot shallow mantle, which has shaped to form the Great Dividing Range (Eastern Highlands) to the north of the Gippsland Basin.

The formation of the Gippsland Lakes is attributed to continual alluvial deposits from the Great Dividing Range and marine deposits during sea level transgressions. Today the top surface of the underlying Tertiary base slopes seaward from the foot of the marginal bluff (backing the Gippsland lakes system to the north) beneath a wedge of ~2Ma Quaternary deposits at a depth of about 18 m at the NMB shoreline, then emerging to form the sea floor beyond the 18 m (10 fathom) depth contour (Bird, 1978; Thom, 1984). The wedge of Quaternary sediments was deposited over successive glaciations and sea level transgressions during the Pleistocene (~2Ma-2.5ka). As sea levels rose sediments were brought from the sea floor to the coast, depositing successive barriers. These barriers held in the alluvial runoff and formed the Gippsland Lakes (Bird, 1994). During the latest Holocene transgression (~2.5ka-present) rising sea levels deposited the final outer barrier dune system defining the present-day NMB coastline. Possible paleo-rivers systems and barrier dune systems have been observed in magnetic and seismic imagery (Holdgate *et al.*, 2003) .

The height of two thousand year old ancient Roman fish tanks indicate that there is little net change in sea levels from 2ka until the start of the 19th century. *In situ* tide measurements reveal that there has been approximately 0.21m of global sea level rise over the past century (CSIRO sea level rise website). Bird, (1978) compared a 1968 coastline survey of NMB with the earliest description of the coastline surveyed by Thwaites in May 1879. He described a straight coastline, prior to opening of the man-made channel in 1890. The 1968 survey shows changes to the coastline, within 2km on either side of the channel changes occurred as a result of the man-made channel, with accretion on the Eastern Beach and erosion of the Western Beach. This morphodynamic change is sometimes referred to as a 'rotated' coastline and is still present in recent LiDAR surveys and aerial photography. Bird went on to note that the 1968 coastline had retreated 100m at distances more than two 2km away from the channel. Additionally, at another site, Ocean Grange, he postulated that the wide spread retreat could not be attributed to the artificial channel, but possibly global sea level rise. However the estimation of 100m retreat seems uncertain for two reasons. The first is that the accuracy of coastline charting methods prior to Global Position System (GPS) surveying have large errors. The second reason is that between the Thwaites and Bird surveys (1890 to 1968), global sea level are estimated to have increased by 0.12m (Church and White 2011), yet the Bruun rule (Bruun 1962) predicts only 6-12m of coastline recession. More recent analysis of aerial photography shows parts of the coastline at the western end of NMB (McLoughlins Beach to Seaspray) both retreating and advancing over three to four surveys spanning the years 1941 to 2006 (Riedel and Sjerp, 2007). Over this 64yr period, global mean sea levels have also risen by around 0.12 cm (Church and White 2011). This rise has not resulted in a continual six to 12m of retreat predicted by the Bruun Rule. This observation suggests that other transport processes, besides rising sea levels, such as onshore and longshore marine and terrestrial transport, are balancing the sediment budget and the coastline position. The interpretation of this review suggests that the position of the larger NMB coastline (away from the channel) has significant variability, but there is not enough evidence to state that the mean position has shifted over the last century.

The natural Gippsland Lakes system would be an Intermittently Closed and Open Lakes and Lagoons (ICOLLs) system if not for the man-made entrance. Since the opening of the channel, an ebb tidal delta, called ‘The Bar’, on the ocean side of the entrance has formed, and it is the largest bedform feature in the nearshore zone. The high-energy beach has rhythmic bars and troughs and the terrestrial foredune has shown significant erosion variability (Bishop and Womersley, 2014). During storm conditions, typically in winter months, an offshore storm-bar and trough can form. At the small-scale, sand-ripple-sized bedforms have been observed on the seabed between 5-20m depths (Black and Oldman, 1999; Wright et al., 1982).

## 2.3 Sediment Transport Models

Sediment transport models designed for river flows have been around for many years, since the 1980s they have been applied to the coastal domain with the important inclusion of wave effects (Van Rijn et al., 2013). As introduced in the last chapter (Section 1.4) models can take on different mathematical representation of the real world using a combination of numerical solutions to PDE on grids and empirical equations for sub-grid processes.

Coastal sediment transport models, implemented in software packages, can be separated into three types based on the resolving of a sub-set of processes (Roelvink and Reniers, 2011). The first type, *coastal profile models,* focus mainly on 1D cross-shore processes. The second type, *coastline models* focus on 1D longshore sediment budget changes and make simplified assumptions on the cross-shore profile. The third type, *coastal area models*, resolve both cross- and longshore 2D or 3D processes. The choice of model type depends on the scale of study, from beach change due to individual storm event to the evolution of a coastline including climate change impacts. The choice of model also depends on the complexity of the coastline, from a simple uniform sandy beach, to a coastline with longshore hard structures (breakwaters and groins), to tidal basins, mega renourishment and land reclamations. Careful consideration must be made about the type of model to use and the value of resources allocated to running the model so as to make efficient predictions or to study detailed processes.

The first two model types, provide practical prediction of sediment changes at sites calibrated to detail field measurements. Splinter et al., (2014) provide a good example of the coastline profile model that is able to predict beach change, where waves are the direct force. Szmytkiewicz et al., (2000) give a good example of a coastline model prediction of longshore beach accretion upstream of a harbour. However, when the simple 1D models are applied to locations with different wave-flow-morphological configurations, the simple assumptions, ignoring the second dimension in the long- or cross-shore direction are challenged by other transport processes (such as a strong coastal current).

The third type of model, *coastal area models*, typically employ computational fluid dynamics, through numerical computations of partial differential equations on a horizontal grid, to solve both the longshore and cross-shore dynamics (e.g. ADCIRC, ROMS, MIKE-21, XBEACH and TELEMAC see model comparison in Roelvink and Reniers, (2011)). For practical application of numerical models, sediment transport typically occurs at the sub-grid (particle) scale. For this reason, they still require parameterisation from empirical equations just like all types of sediment transport models. The main advantage being that the hydrodynamic flow and waves are more accurately resolved and that sediment budget can be balanced over the entire coastal area.

At the most basic end of the spectrum of sediment transport models, empirical equations have been used to find the simplest relationship (or pattern of behaviour) between sediment transport and wave and current parameters (e.g. Bayram *et al.*, 2007; Kamphuis *et al.*, 1986; Komar, 1971; Mil-homens *et al.*, 2013; Tomasicchio *et al.*, 2013; Van Rijn, 2014). Some empirical equations have been calibrated to locations where transport is almost exclusively controlled by waves and therefore do not account for flow parameters (e.g. CERC, 1984). These equations may underestimate the contribution of wind- and tide- driven currents when applied to regions of strong currents (Bayram *et al.*, 2007). In this study the CERC energy flux equation is investigated, as it is the most widely used, and it is applied in the dredging program at the field site (GHD, 2013).

Towards the more sophisticated end of the spectrum of transport models, a suite of three coupled models can be used. Each model employing PDEs and empirical equations to resolve the hydrodynamic flow, wave field and sediment transport (e.g. ADCIRC, MIKE-21, XBEACH and

TELEMAC). The coupled models can take on the challenge of the most complex hydrodynamic processes in the nearshore region, including the effect of depth-induced wave breaking. When ocean waves enter the nearshore region, they feel the shallowing depths, steepen as they slow down until they eventually break. Along with generating turbulence, the effect of this breaking results in a stress applied to the water column causing rips- and longshore- currents which scatter sediment particles (Longuet-Higgins and Stewart, 1964).

A practical method to resolve this nearshore wave field is to utilise a spectral wave model (e.g. SWAN, XBEACH and TOMAWAC). Spectral wave models are efficient in propagating wave energy using PDEs, resolving wave generation and dissipation and importantly the depth-induced wave breaking. The resulting wave-driven forces can be passed to a hydrodynamic model to generate currents and transport sediments (Longuet-Higgins, 1970).

Hydrodynamic models (e.g. ROMS, Delft2D-FLOW and TELEMAC2D) propagate mean circulation around a domain. Flow is driven by changes in the pressure gradient from the atmosphere and astronomical tide, surface wind friction and bottom friction. Importantly for nearshore studies, and where there is strong coastal flow, hydrodynamic models can simulate the additional currents driven by depth-induced wave breaking.

Superimposed on the mean circulation field is the orbital motion of waves, which can mobilise sediments. Wave orbital motion occurs at the sub-grid-scale for practical model applications, and is typically formulated from linear wave theory (Van Rijn, 2007). The modelling of sediment transport is dependent on the flow or stress (quadratic flow/stress law) exceeding a critical threshold to mobilise sediments. For this reason, the coincidence of strong wave orbital flow with wind-, wave- and tide- driven currents above a critical flow threshold will result in sediment transport.

Downscaling the GCM-derived data to a transport model requires that the transport model is capable of inputting the right parameters. These parameters include the increased water levels as an analogue to sea level rise or changes to the longshore current as an analogue to future flow conditions.

The process of evaluating models has led to choosing the *coastal area* model for the present application. This is because we want to capture the detailed processes of the strong longshore current and its effect on longshore transport, on the scale of climate change, on a moderately complex coastline. Of the coastal area models, (e.g. DELF3D, MIKE-21, ADCIRC) the TELEMAC suite of models was chosen for personal preferences, as it is open source, with unstructured grid configuration, all model packages (wave-hydrodynamic-sediment) have two-way coupling, the high quality code formatting conventions across all files within the system and detailed model documentation with an active user community forum.

## 2.4 TELEMAC Sediment Transport Model

OpenTELEMAC, TELEMAC-MASCARET or just TELEMAC is a suite of finite element numerical programs to solve geophysical fluid dynamics (Hervouet, 2007). Since January 2010 the software suite became open source and now has a strong community supporting it.

A summary of TELEMAC ability to model sediment transport is given in Villaret *et al.*, (2013). The TELMAC package has been shown to provide similar results to the proprietary Mike-21 model for the Italian coast (Samaras *et al.*, 2016). An example of models to preform multiyear, decadal longer timescales has been studied for the German coastline (Putzar and Malcherek, 2012). Climate change downscaling of RCMs with TELEMAC has been conducted for the English coast (Chini and Stansby, 2015). These regional studies demonstrate the variety of approaches, high degree of empiricism and challenges of modelling long-term sediment transport with limited computational resources.

Three programs from the TELEMAC (version 7.1r1) suite are required to model sediment transport in the nearshore region. The first is *TELEMAC2D* to model the flow hydrodynamics, the second is *TOMAWAC* to model the sea-swell waves and the third is *SISYPHE* to model sediment transport. The design of the model coupling, forcing and validation setup is provided in Figure 2.3.

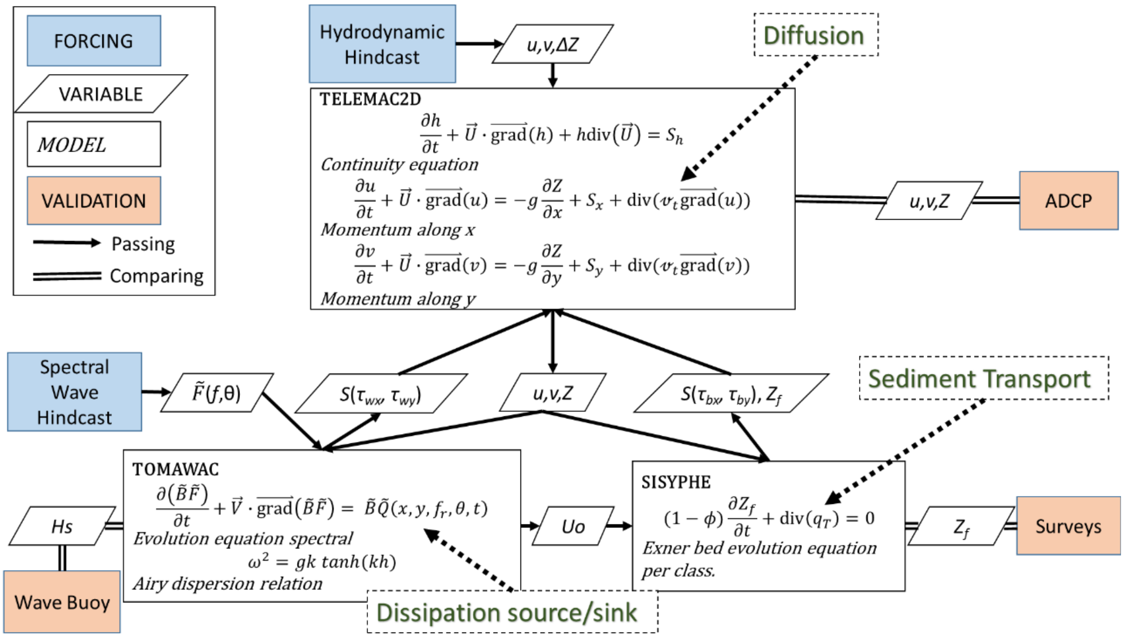


**Figure 2.3 Diagram of TELEMAC model forcing, coupling and validation.** White boxes represent the three TELEMAC version 7.1r1 models. Blue boxes represent the forcing from the wave and hydrodynamic hindcast data. The Parallelograms indicate model variables. Red boxes represent the measured wave current and bathymetric validation datasets. Green boxes represent the main tuning parameters. Arrows indicate the direction of variable input between models and double lines indicate validation. Dashed arrows point to the main tuning parameters in each model.

### 2.4.1 Hydrodynamics

The TELEMAC2D code solves depth-averaged free surface flow Navier-Stokes equations (Equations 2-1 to 2-3) also referred to as the Saint-Venant equations (Saint-Venant, 1871). The model simulates depth averaged velocities and free surface height on an unstructured grid using finite element numerical schemes. Important to our investigation, the model is able to simulate the propagation of long wave (surge tide) boundary conditions, and parametrise wave-induced current. The Saint-Venant equations are;

$$\frac{\partial h}{\partial t} + \vec{U} \cdot \overrightarrow{\mathrm{grad}}(h) + h\mathrm{div}(\vec{U}) = S_h \tag{2-1}$$

$$\frac{\partial u}{\partial t} + \vec{U} \cdot \overrightarrow{\mathrm{grad}}(u) = -g\frac{\partial Z}{\partial x} + S_x + \mathrm{div}(\nu_t \overrightarrow{\mathrm{grad}}(u)) \tag{2-2}$$

$$\frac{\partial v}{\partial t} + \vec{U} \cdot \overrightarrow{\mathrm{grad}}(v) = -g\frac{\partial Z}{\partial y} + S_y + \mathrm{div}(\nu_t \overrightarrow{\mathrm{grad}}(v)) \tag{2-3}$$

,where $h$ is the water depth, $Z$ is the free surface elevation, $u$ and $v$ are the velocity components of the depth averaged velocity vector $\vec{U}$, $S_x, S_y$ are the two components of the source term from the sum of bottom friction and wave radiation stress and $\upsilon_t$ is the turbulence diffusion which is used to tune the model.

### 2.4.2 Waves

Wave are resolved with TOMAWAC, a third generation spectral wave model (Benoit et al., 1996). Third generation models explicitly represent all the physics relevant for the development of the sea state in two dimensions. The model solves the directional spectrum of wave action density equation;

$$\frac{\partial(\tilde{B}\tilde{F})}{\partial t} + \vec{V} \cdot \overrightarrow{\mathrm{grad}}(\tilde{B}\tilde{F}) = \tilde{B}\tilde{Q}(x, y, f_r, \theta, t) \tag{2-4}$$

,where $\tilde{F}$ is the density variance spectrum, $\tilde{Q}$ is the source and sink terms of wave generation and dissipation, $\tilde{B}$ is a factor which allows $\tilde{Q}$ to be expressed as a function of $\tilde{F}$, where from linear wave theory the terms to be solved are;

$$\tilde{B} = \frac{c_g}{(2\pi)^2 k f_r} \tag{2-5}$$

$$\vec{V} = \langle \dot{x}, \dot{y}, \dot{f_r}, \dot{\theta} \rangle \tag{2-6}$$

$$\dot{x} = c_g \sin\theta + u \tag{2-7}$$

$$\dot{y} = c_g \cos\theta + v \tag{2-8}$$

$$\dot{f_r} = \frac{1}{2\pi}\left[\frac{\partial\sigma}{\partial h}\left(\frac{\partial h}{\partial t} + \vec{U} \cdot \overrightarrow{\mathrm{grad}}(h)\right) - c_g\vec{k} \cdot \frac{\partial\vec{U}}{\partial\overrightarrow{G_T}}\right] \tag{2-9}$$

$$\dot{\theta} = \frac{1}{k}\frac{\partial\sigma}{\partial h}\frac{\partial h}{\partial\overrightarrow{G_N}} - \frac{\vec{k}}{k} \cdot \frac{\partial\vec{U}}{\partial\overrightarrow{G_N}} \tag{2-10}$$

, where $Cg$ is the wave group velocity, $f_r$ is the spectral-relative wave frequency, $k$ is the wave number, $\theta$ is the spectal-relative wave direction, $\vec{V}$ is the transfer rate due to currents, with the transferred spatial and spectral coordinates due to currents refracton and doppler effects are accented with a dot above, $G_N$ and $G_T$ are the normal and tangental wave vectors respectivly.

Third generation spectral wave models take a variety of inputs for wave generation and dissipation over different domains (oceanic and nearshore). Wind dissipation (e.g. white-capping) and generation are ocean scale processes, so for the nearshore application we will only consider the following wave source terms are considered;

$$\tilde{Q} = \tilde{Q}_{bf} + \tilde{Q}_{bb} + \tilde{Q}_{cb} + \tilde{Q}_{tr} \qquad \textbf{2-11}$$

The spectral wave model has a main time step for convection (propagation) of the wave field (Equation 2-4), a second time sub-step for the integration of all source and sink terms, including dissipation by bottom friction ($\tilde{Q}_{bf}$), and a third sub-step for the nearshore depth-induced breaking ($\tilde{Q}_{bb}$), non-linear triad ($\tilde{Q}_{tr}$) and breaking by strong current ($\tilde{Q}_{cb}$) terms.

### 2.4.3 Sediment transport and bed evolution

SISYPHE is used to parametrise transport estimates from input from the hydrodynamic and wave models and the then balance the bed evolution. SISYPHE can model suspended transport by including a tracer equation of sediment concentration in the TELEMAC2D transport equations. For simplicity and efficiency, a total transport equation was selected that takes into account the combined effects of suspended load with bed load in the transport parameterisation (see next section on model setup). The Exner equation solves this total load transport and bed evolution (erosion/accretion) and is formulated as;

$$(1-\phi)\frac{\partial Z_f}{\partial t} + \mathrm{div}(q_T) = 0 \qquad \textbf{2-12}$$

, where $\phi \approx 0.4$ is bed porosity, $Z_f$ is the bottom elevation and $q_T$ is the total transport estimates. The estimate of the total transport takes into account a spatially varying sediment field by employing different population percentages of different classes of sediment in each grid cell. Transport is calculated for each class and summed together (population weighted) to estimate the total transport.

To aid with model comparison, point source transport estimates made by TELEMAC are denoted with a lowercase $q$ and have units $m^3/m/s$ to state that it is a volume transported per unit width of the bed. Intergraded transport estimates in cross-shore direction across the surf zone, made by the CERC equation and integrated for TELEMAC ($q_T$), are denoted by an uppercase $Q$ and have units $m^3/s$ (not to be confused wave source term$\tilde{Q}$).

# 3. MEASUREMENTS, MODEL DATA AND METHODOLOGY

This study makes use of four types of data sources that are described in detail in this section and summarised in Table 3-1 and Table 3-3. The first type of data includes direct, *in-situ* measurements of atmospheric and oceanographic variables along with bathymetric surveys and sediment samples. The direct observations provide the means to validate model-generated information. The second type of data includes simulations of atmospheric and oceanographic variables in models that are constrained by atmospheric conditions over a particular observational period. These hindcasts provide 'pseudo-data' at regular spatial and temporal resolution for time periods amounting to several decades and also provide a means to investigate the nature of the coastal ocean response on interannual time scales. The third type of data includes simulations of atmospheric and oceanographic variables in models configured to represent present and future climate conditions, so that future changes can be assessed. For atmospheric variables, Global Climate Models (GCMs) are used, whereas for ocean variables, wave and hydrodynamic models that use atmospheric forcing from GCMs are used. The fourth type of data includes the climate indices, which are used to explore relationships between climate variability and coastal response in the study area.

This section concludes with methodologies used in the study. The first of these involves estimating sediment transport from measured bedform migration. The second methodology involves the configuration of the TELEMAC sediment transport model. The third methodology is about the development of a semi-empirical equation to extrapolate the TELEMAC simulations.

## 3.1 Measurements

**Table 3-1 Measured and modelled atmospheric and ocean dataset information.**

| **Dataset** | **Wind** | **Wave** | **Currents** |
|---|---|---|---|
| platform | Land based Met-station | Wave Buoy | ADCP |
| Location | Bullock Island | 2km off coast 21m depth | 2km off coast 21m depth |
| GPS Location | 37.890S 147.9733E | 37.9133S 147.9819E | 37.9130S 147.9793E |
| Length Data | 4.21 | 4.21 | 2.45 |
| start Date | 15/04/2008 | 15/04/2008 | 7/04/2008 |
| end date | 1/07/2012 | 1/07/2012 | 21/09/2010 |
| Hindcast/Reanalysis | CFSR | CAWCR_WW3_CFSR | ROMS_CFSR |
| Resolution | 1/3Deg | 4ArcMin, 1Deg | 5km |
| GPS Location | 37.89S 147.97E | 37.91S 148E | 38.46S 147.458E |
| Length Data | 31.00 | 29.00 | 31.00 |
| start Date | 1/01/1979 | 1/01/1981 | 1/01/1981 |
| end date | 1/01/2010 | 31/12/2009 | 1/01/2010 |
| HADGEM | 10m Winds | COWCLIP_WW3 | ROMS |
| Resolution | 1.25x1.875deg,360day/yr | 1Deg | 5km |
| GPS Location | 37.917S 148E | 37.917S 148E | 38.458S 147.458E |
| Length Data | 19.71_18.73 | 19.71_18.73 | 27_19 |
| Baseline dates | 1980-01-01_2000-01-01 | 1980-01-01_2000-01-01 | 1979-01-01_2006-01-01 |
| Future dates | 2081-01-01_2100-01-01 | 2081-01-01_2100-01-01 | 2081-01-01_2100-01-01 |
| ACCESS | 10m Winds | COWCLIP_WW3 | ROMS |
| Resolution | 1.25x1.875deg, real years | 1Deg | 5km |
| GPS Location | 37.917S 148E | 37.917S 148E | 37.917S 148E |
| Length Data | 20_19.99 | 20_19.99 | 27_20 |
| Baseline dates | 1980-01-01_1999-12-31 | 1980-01-01_1999-12-31 | 1979-01-01_2006-01-01 |
| Future dates | 2081-01-02_2101-01-01 | 2081-01-02_2101-01-01 | 2081-01-01_2101-01-01 |
| CNRMCM5 | 10m Winds | COWCLIP_WW3 | ROMS |
| Resolution | 1.4x1.4, real years | 1Deg | 5km |
| GPS Location | 37.917S 148E | 37.917S 148E | 37.917S 148E |
| Length Data | 20_20 | 20_20 | 27_20 |
| Baseline dates | 1980-01-01_1999-12-31 | 1980-01-01_1999-12-31 | 1979-01-01_2006-01-01 |
| Future dates | 2080-01-01_2099-12-31 | 2080-01-01_2099-12-31 | 2081-01-01_2101-01-01 |
| INMCM4 | 10m Winds | COWCLIP_WW3 | ROMS |
| Resolution | 1.5x2deg, 365 day/yr | 1Deg | 5km |
| GPS Location | 37.917S 148E | 37.917S 148E | 37.917S 148E |
| Length Data | 19_18.99 | 19_18.99 | 27_20 |
| Baseline dates | 1981-01-01_1999-12-31 | 1981-01-01_1999-12-31 | 1979-01-01_2006-01-01 |
| Future dates | 2081-01-02_2099-12-31 | 2081-01-02_2099-12-31 | 2081-01-01_2101-01-01 |

Both standard oceanographic and meteorological conventions of direction are adopted in this paper. Wave direction, currents and transport are reported in standard oceanographic convention, i.e. direction towards which the waves are travelling in degrees clockwise from True North, e.g. *westward movement* is towards the west (270º). Wind direction is reported in standard meteorological convention, i.e. the direction from which the wind is coming in degrees clockwise from True North, e.g. *westerly winds* from the west (270º). The exception to the rule is that the wind stress, τ;

$$\tau = \rho_a C_D V^2 \qquad \textbf{3-1}$$

, where $V$ is the 10-m wind speed, $\rho_a$ = 1.225 kg/m$^3$ is air density and $C_D$ = 1.2x10$^{-3}$ is the dimensionless drag coefficient, is reported in the oceanographic convention to align the longshore directions with the waves and currents.

### 3.1.1 Meteorological Fields

Ten-minute average wind observations from an anemometer located at a height of ten metres on a signal tower at the entrance breakwater and Mean Sea Level Pressure (MSLP) from a barometer located on Bullocks Island are available over a 4-yr period from 2008-2012 (see Figure 2.1 for location and Table 3-1 for further details). Both instruments were out of operation for around 12% of the measurement period due to servicing and short term failure.

### 3.1.2 Waves

Observations of the integrated spectral wave parameters of significant wave height (*Hs*), mean wave period (*Tm*) and mean wave direction (*Dm*) were measured from April 2008 to July 2012 by a directional wave buoy located 2 km off the coast at the Entrance to the Gippsland Lakes in the vicinity of the ocean current measurements in approximately 22 m of water (Figure 2.1). The instrument was not in operation for about 18% of the measurement period due to servicing and short term failure.

### 3.1.3 Currents and water levels

Depth-averaged 3D ocean current observations are available from 18 two-month deployments between April 2008 and September 2010. The measurements were from a bottom mounted Teledyne RDI Workhorse Sentinel Acoustic Doppler Current Profiler (ADCP) located at a depth of 21 m, 2 km off the coast at Lakes Entrance (Table 3-1). The current meter was located in the vicinity of the wave buoy. The ADCP was not in operation for about 2% of the measurement period due to servicing or short term failure.

### 3.1.4 Bathymetry

Three types of bathymetric surveys were used in this study. The bathymetry surveys were mapped onto a regular grids for analysis (Table 3-2).

**Table 3-2 Bathymetry grid coordinates. UTM zone 55 south.**

| Grid | Rotation $\theta_R$ | Origin Easting | Origin Northing | Resolution | Longshore grid length | Cross-shore grid length | Coastline offset |
|---|---|---|---|---|---|---|---|
| West | 20.5° | 581950 | 5803950 | 2.5m | 3000m | 825m | 25.0m |
| East | 20.5° | 586750 | 5805400 | 2.5m | 3000m | 1000m | 102.5m |
| Model | 18.0° | 582500 | 5802000 | 40-200m | 8200m | 3200m | - |

#### 3.1.4.1 LiDAR

An airborne LiDAR survey of the entire NMB seaboard was conducted from November 2008 to April 2009. The survey was gridded onto 2.5m tiles using the Universal Transverse Mercator (UTM) zone 55 south projection (Sinclair and Quadros, 2010). The gridded bathymetric and topographic datasets provide data from around 100 metres inland to a depth of around 20m, depending on the turbidly of the water for the Laser to penetrate. The 20m-depth contour is typically a few kilometres off the coast of NMB. The zero vertical chart datum is Mean Sea Level (MSL).

The coastline UTM x-y coordinates of NMB were extracted from the LiDAR survey tiles along the zero bathymetry contour (MSL line) at 10m intervals. At each interval (point) along the coastline the coordinates of the profile normal (perpendicular) to the coastline was identified from 200m inland to 4000m offshore. The LiDAR survey tiles were then mapped onto these profile coordinates at each profile, at 10m intervals along the coastline. These mapped coastline normal profiles were stacked next to each other to form a Coastline Normal Profile Grid (CNPG). The CNPG represents a ‘straightened out’ map ‘projection’ of the NMB curved coastline. Where the positive y-axis of the CNPG represents the eastward longshore direction and the positive x-axis resents the offshore direction. The coastline of the CNPG is always at x = 0 and the depth values in the cross-shore x direction are the actual normal (perpendicular) depth values.

### 3.1.4.2 Single-beam Sonar

As part of the ongoing dredging operations at Lakes Entrance, bathymetric depth sonar surveys of two large rectangular Dredge Material disposal Grounds (DMGs) and bordering regions of the open coast have been undertaken (GHD, 2013; Figure 3.1 insert). These surveys span ~2km along the coast and extend from ~100m to ~800m off the coast, framing the design DMG with a 100m ribbon of extra survey area. Nine surveys for the west DMG and ten for the east DMG are available to quantify the variability of the profile. The surveys are at irregular time intervals, spanning ~3.7 years (Table 3-3).

The single-beam transit lines occur every 100m in the longshore direction. The landward extents of the surveys are limited by operational depth constraints of the vessel (typically 2m from MSL). The single-beam datasets are projected onto the (UTM) zone 55 south coordinates. The survey zero chart datum of 0.757m below MSL, which is approximately Indian Springs Low Water (Riedel and Sjerp, 2007), is adjusted to MSL. This was done to be in line with the LiDAR dataset. The scattered survey points, which are separated by an average of 1 to 2m, were mapped onto a regular 2.5m grid, rotated by 20.5° from the origin for the west (581950,5803950) and east (586750,5805400) sites respectively. Both of these grids spaned 3km in the longshore -y direction and ~1km in the cross-shore -x direction (Table 3-2). The soundings were mapped with a bi-linear interpolation method. The first eight single-beam surveys, at both sites, showed the absence of a storm-bar and trough between June 2009 and Feb 2011. The final two surveys, between September 2011 and March 2012, showed the presence of a storm-bar (Figure 3.2). The storm-bar profiles represent a high wave energy climate typical of a ‘winter’ profile, but can occur in summer months.

### 3.1.4.3 Multi-beam Sonar

Multi-beam soundings superseded the single-beam surveys after 2011. They are available for both sites for five surveys each between 2012 and 2013. The data is limited to survey taken seaward of the storm-bar (>5m depth) due to the operational depth limits of the survey vessel. The scattered survey points, separated by < 1m on average, were mapped onto the same regular grid as the single-beam surveys (Table 3-2). The soundings were mapped with a nearest neighbour method. The multi-beam surveys are on the same map projection and chart datum as the single-beam and has been adjusted to MSL to be in line with the LiDAR data set. More detail on the surveys and the dredging and disposal program can be found in the port authorities annual reports (GHD, 2013). Surveys were conducted using differential GPS with an accuracy of < 0.10 m.

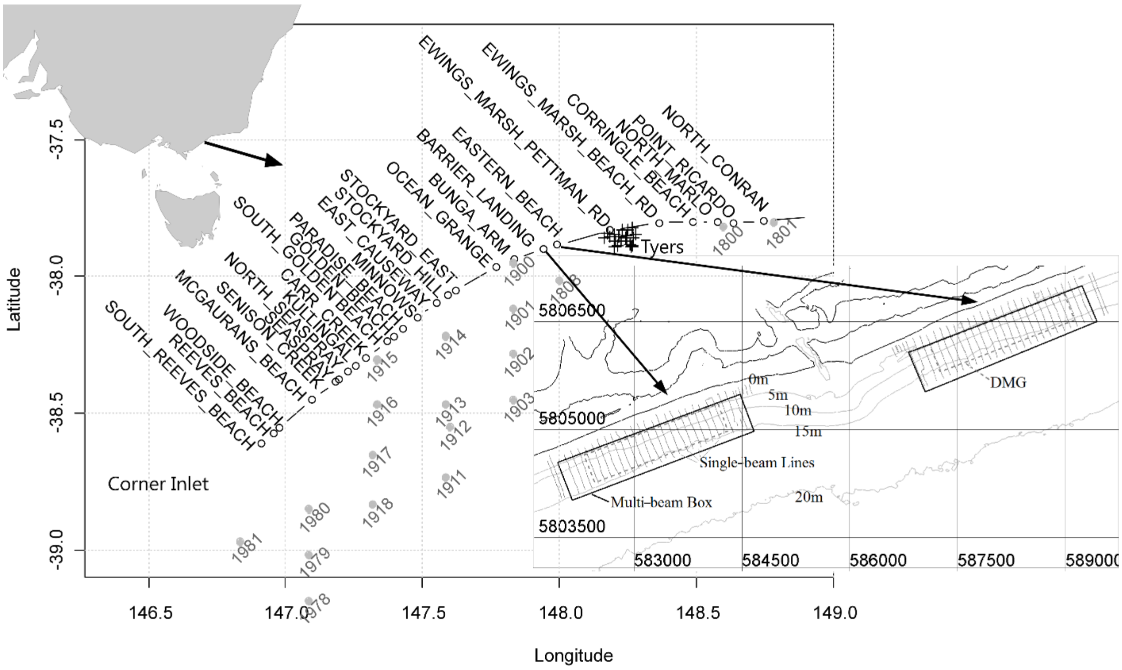


**Figure 3.1 Map of the sediment samples locations and insert of bathymetric surveys.**

Grey dots are ship-based samples with corresponding site ID number (Jones et al., 1983). Black circles and location names are the beach sample sites (Wright et al., 1982). Clusters of black crosses near Ewings Marsh Road are the Tyers site samples (Black *et al.*, 2013). The insert is Lakes Entrance with the examples of the single-beam transects (cross-shore lines separated by 100 m) and multi-beam survey area (thick black box) at both the west and east dredge material grounds (DMG) sites (grey dashed box) with the UTM zone-55 map-projection.

**Table 3-3 Details of bathymetric surveys.**

| File ID | Date | DMG | Measurement Type | Initiate Survey Number | Event Duration (Days) | Type of Profile |
|---|---|---|---|---|---|---|
| - | 2008-2009 | All | LiDAR | ALL | - | storm (bar) |
| GL5422 | 20090618 | West | single-beam | 1 | 49 | calm (no bar) |
| GL5424 | 20090619 | East | single-beam | 1 | - | calm (no bar) |
| GL5444 | 20090730 | West | single-beam | 2 | 67 | calm (no bar) |
| GL5447 | 20090806 | East | single-beam | 2 | - | calm (no bar) |
| GL5462 | 20091005 | Both | single-beam | 3 | 35 | calm (no bar) |
| GL5476 | 20091109 | Both | single-beam | 4 | 92 | calm (no bar) |
| GL5497 | 20100209 | Both | single-beam | 5 | 202 | calm (no bar) |
| GL5508 | 20100510 | West | single-beam | - | | calm (no bar) |
| GL5528 | 20100830 | Both | single-beam | 6 | 100 | calm (no bar) |
| GL5549 | 20101208 | Both | single-beam | 7 | 111 | calm (no bar) |
| GL5563 | 20110329 | Both | single-beam | 8 | 183 | calm (no bar) |
| GL5592 | 20110928 | Both | single-beam | 9 | 16 7 | storm (bar) |
| GL5627a | 20120119 | West | multi-beam | - | - | calm (no bar) |
| GL5627b | 20120119 | West | multi-beam | - | - | calm (no bar) |
| GL5663a | 20120313 | East | multi-beam | - | - | storm (bar) |
| GL5663b | 20120313 | East | multi-beam | - | - | storm (bar) |
| GL5664 | 20120313 | Both | single-beam | 10 | 120 | storm (bar) |
| GL5665 | 20120710 | West | multi-beam | 11 | 91 | calm (no bar) |
| GL5670 | 20120711 | East | multi-beam | 11 | - | calm (no bar) |
| GL5687 | 20121004 | West | multi-beam | 12 | 49 | calm (no bar) |
| GL5690 | 20121009 | East | multi-beam | 12 | - | calm (no bar) |
| GL5703 | 20121114 | West | multi-beam | 13 | 30 | calm (no bar) |
| GL5706 | 20121122 | East | multi-beam | 13 | - | calm (no bar) |
| GL5716 | 20121213 | East | multi-beam | 14 | 90 | calm (no bar) |
| GL5717 | 20121214 | West | multi-beam | 14 | - | calm (no bar) |
| GL5732 | 20130313 | West | multi-beam | - | - | calm (no bar) |
| GL5733 | 20130313 | East | multi-beam | - | - | calm (no bar) |

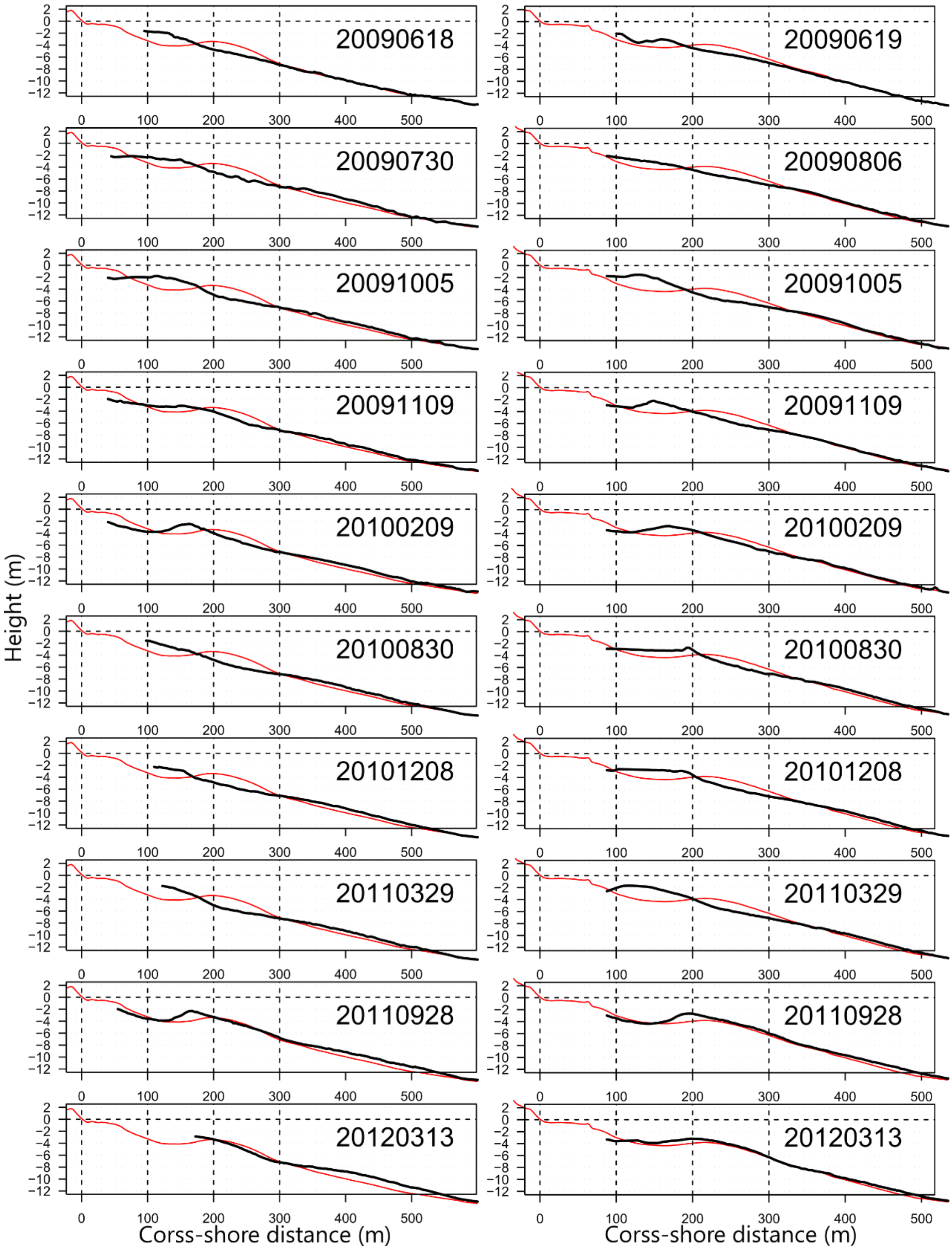


**Figure 3.2 Profile view of the temporal variations in the west and east survey sites.**

West (east) site surveys start in chronological order starting at the top of the left (right) column run down the column. Single-beam surveys (thick black) lines are the average of profile in the longshore direction (located between y = 1700 to 1900 m). LiDAR survey (red line).

### 3.1.5 Morphology

#### 3.1.5.1 Cross-shore Morphology

Field work by (Wright et al., 1982) sampled marine sediments at Eastern Beach to show constant medium mean grain sizes of around 0.3-0.4mm from the coastline to 10m depth (Figure 3.3). From 10m to 20m depth the grain size increases somewhat linearly to coarse mean grain sizes of around 0.8mm at 20m depth. The morphology at 20m depth is described as cobbles with some whole shells. A second large ship-derived study, in deeper water, showed medium to coarse sand sizes of 0.25-0.6mm from 20-40m and then increasing to medium to very coarse sands between 0.25-1.4mm at 60m depth (Jones et al., 1983; Figure 3.3). A third study near Ewings Marsh Road (~25km east of Eastern Beach) found medium sediments of around 0.3-0.4mm at 10m depth, then increasing from coarse sediments of 0.06mm at 20m depth and then 0.09mm at 40m (Black *et al.*, 2013; Black and Oldman, 1999).

The cross-shore sorting and carbonate content of sediments between 20-60 m depth (Jones et al., 1983) shows two distinct groups separated at around the 40 m depth contour. Moderately sorted sediments with CaCO3% < 30% are found at depths less than 40 m and poorly to very poorly sorted sediments with CaCO3% > 80% at depths greater than ~40 m. The analysis of the sand fraction of the sample (not the whole sediment sample), show very well to well sorted sands at all depths up to 45 m near Ewings Marsh (Black et al., 1991). The sediment properties at depths between 5-20 m are somewhat similar to those up to 40 m, suggesting some conductivity. However, in the deeper water, high CaCO3% indicates a lack of terrestrial quartz sediments, and the coarse, unsorted deposits indicate regions of reduced energy and transport activity.

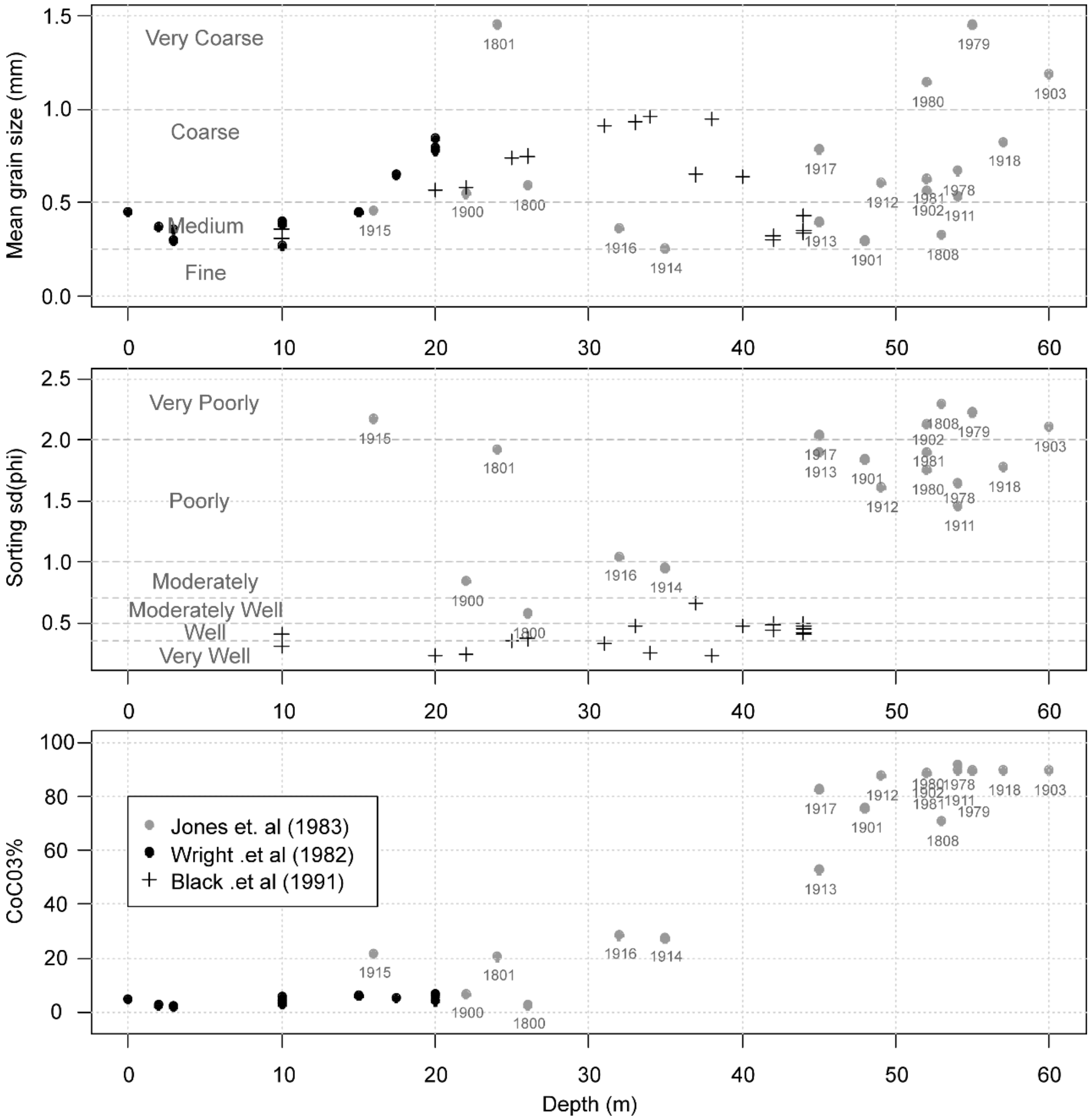


**Figure 3.3 Cross-shore sediment grain size, sorting and Carbon % with depth.** Numbered data points are from Jones et al., (1983) at station numbers plotted in Figure 3.1. Tyers site survey points are from the second survey 11th February 1991 (Black *et al.*, 2013). Sorting values refer only to the sand fraction of the sample, not the whole sediment sample (Black *et al.*, 2013).

### 3.1.5.2 Longshore Morphology

The field work by Wright et al., (1982) also sampled the sediments on the beach and in the surf zone (to around 4m depth) at around 30 locations along the extended NMB coastline. These samples revealed a positive linear regression between beach-face slopes and mean grain size found on the beach. Sediment sorting and mean grain sizes within the surf zone showed spatial variability (Figure 3.4). The samples showed poorly-sorted, very-coarse-grain sizes to the western side of NMB and moderately-well to moderately sorted coarse-grain sizes to the eastern side. The samples also showed an increasing west to east gradient in the carbonate percentage from Corner Inlet to East Causeway, then a decreasing gradient towards the artificial entrance.

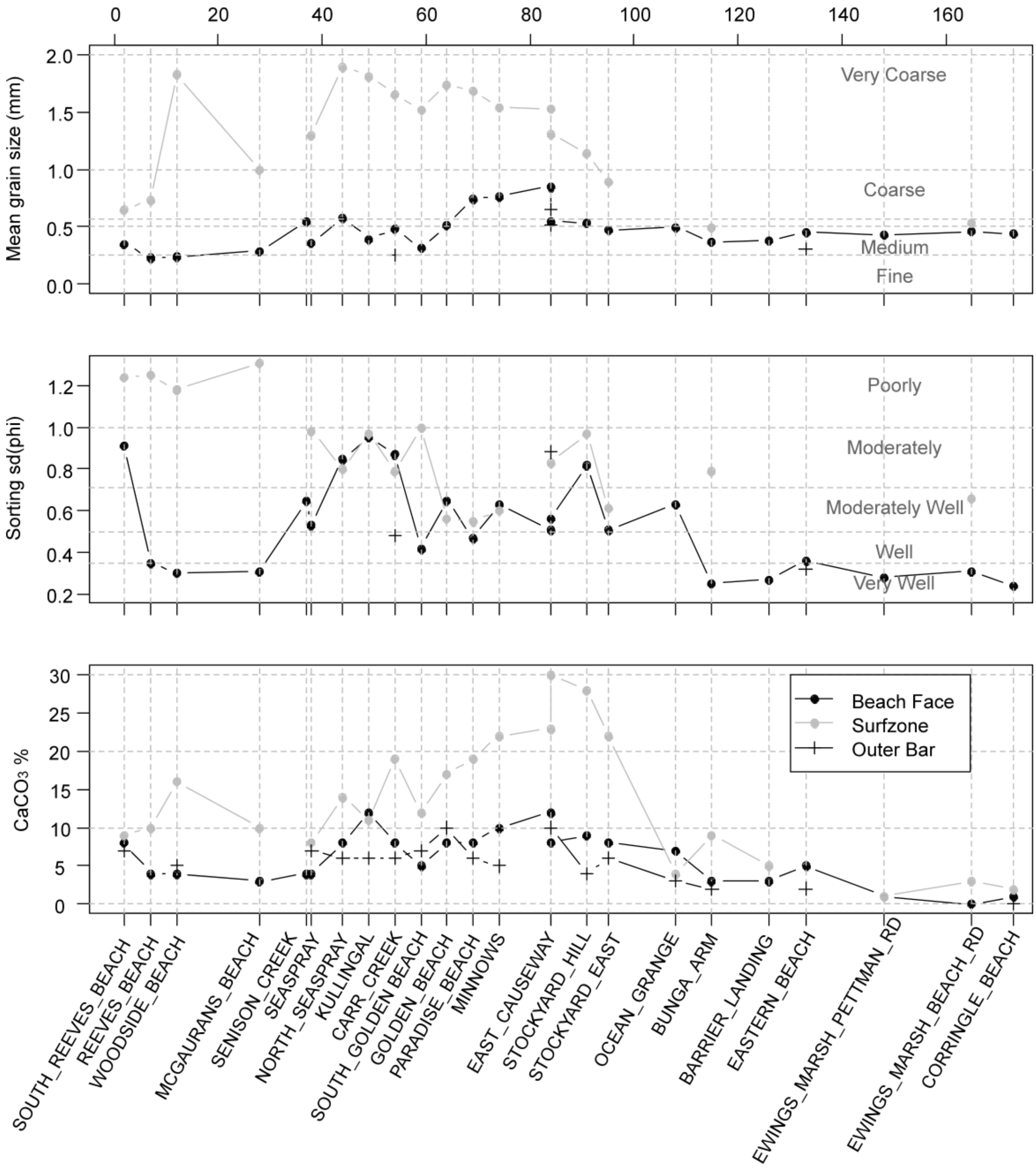


**Figure 3.4 Longshore sediment grain size, sorting and Carbon % along NMB.**

Data from Wright et al., (1982). Black line and dots are sampled on the beach face. Grey lines and dots are samples within inner surf zone. Black '+' and lines are samples at the outer bar. Grain sizes are converted from phi scale to mm (where $d$[mm] = $2^{-\varphi}$).

## 3.2 Hindcast Data

### 3.2.1 Meteorological Fields

The Climate Forecast System Reanalyses (CFSR) dataset (Saha et al., 2010), provides meteorological variables across the globe at hourly temporal resolution and approximately 38 km spatial resolution, from 1979 to 2009. Relevant meteorological data from this dataset were used to provide forcing for wave and hydrodynamic models in order to generate hindcasts of ocean waves, currents and sea levels.

### 3.2.2 Waves

Two wave hindcasts were available for use in this study. In the first, the 10 m winds from CFSR were used to force the WAVEWATCH III (WW3, v3.14; Tolman 2009) model with global coverage at one degree spatial resolution as part of the Coordinated Ocean Wave Climate Project (COWCLIP; Trenham et al., 2013). The COWCLIP simulations provide a consistent benchmark for the baseline GCM-forced simulations, which were also modelled at one-degree resolution with the same model parameterisation. The second, referred to here as the Centre for Australian Weather and Climate Research (CAWCR) wave hindcast, was performed with WW3, v4.08 at 4 arc-minute resolution around the Australian coast (Durrant et al., 2014).

### 3.2.3 Currents and water levels

CFSR fields were also used to force a barotropic Australia-wide configuration of the Regional Ocean Modelling System (ROMS) (Shchepetkin and McWilliams, 2005). The hydrodynamic model simulated the depth-averaged tide and atmospheric forced currents and water levels around Australia at a 5 km resolution. An earlier set of runs for southern Australia, which used a similar configuration of ROMS, is described in Colberg *et al.*, (2017). Globally gridded, hourly CFSR 10 m winds and MSLP are used to force the hydrodynamic model. The atmospheric fields were interpolated bilinearly onto the 5 km grid of the hydrodynamic model. Winds over land were masked out and replaced with extrapolated values from the ocean grid points.

## 3.3 Climate Model Data

Future changes to waves and currents were investigated in wave and hydrodynamic simulations, where the 10 m wind and pressure forcing was obtained from Global Climate Models (GCMs). The source of the GCM simulations is the fifth phase of the Coupled Model Intercomparison Project (CMIP5; Taylor et al. 2012). Only four GCM model simulations were chosen from the available selection of CMIP5 model simulations because of the large computational requirements of running the wave and hydrodynamic models. The models were selected on the basis that they stored surface wind and pressure data at 3-hourly temporal resolution, were available at the time the wave and hydrodynamic modelling was undertaken and were assessed as providing a credible climatology of winds over the observational period. The selected models were the HadGEM2-ES, ACCESS1.0, INMCM4 and CNRM-CM5 models. The GCM experiments selected were run with greenhouse gas forcing following the Representative Concentration Pathway (RCP) 8.5 experiment (Riahi et al., 2011), which leads to a radiative forcing of 8.5 W/m$^2$ in 2100. The hydrodynamic and wave models simulations were performed over two 20-year periods; 1981-2000 representing the baseline period and 2081-2100 representing the future climate period. Changes between these time periods were assessed by subtracting the averages of model variables of the baseline period from the future period.

The wave and hydrodynamic simulations were carried out independently of each other with no feedbacks or interactions between them, i.e. currents do not interact with waves and waves do not generate currents. The interaction of waves and currents generally occurs in the nearshore littoral zone at a scale finer than these large-scale coastal simulations. The three-hourly ~1.5 degree GCM wind fields from the HadGEM2-ES, ACCESS1.0, INMCM4 and CNRM-CM5 models were also interpolated onto the same hydrodynamic 5 km grid Table 3-1.

Astronomical tides and storm surges are often considered to be independent processes. However, within Bass Strait, modelling studies have shown that resonance behaviour and the interaction between wind-driven currents and astronomical tide can attenuate the prediction of the M2 tidal constituent amplitudes (Wijeratne et al., 2012). This attenuation of the modelled sea level is highest in central Bass Strait, to the west of Wilsons Promontory (Figure 2.1) and diminishes towards the open ocean boundaries of the basin, including our study area. For this reason and to reduce computational expense, the hydrodynamic simulations forced by the CMIP5 model atmospheric data under present and future climate conditions do not include tidal forcing.

Normalised values were calculated to indicate the relative climate change signal from a models internal variability for ensemble model comparison, where the internal variability is described as one standard deviation of the model time series. Values were normalised to lessen any bias within the model that arises from that model's change signal. Normalised climate model anomalies ($A$) were calculated as the difference between the future ($F_G$) 2081-2100 and baseline ($B_G$) 1981-2000 GCM model output relative to the standard deviation of the baseline ($B_G$) output;

$$A = (F_G - B_G)/sd(B_G) \qquad \textbf{3-2}$$

## 3.4 Climate Indices

### 3.4.1 Subtropical Ridge Location

Different measurements of the STR have been used in various studies including the strength or location of the STR (Kent et al, 2011). For the study here, we only focus on location of the STR. For a given longitude, the latitude or location index of the STR (STR-L) is extracted from the maximum MSLP grid point between 25-50°S in the monthly CFSR gridded dataset. STR-L values that were identified north of 25°S or south of 50°S were excluded from the analysis. This resulted in less than 1% of the monthly data excluded for all models except CNRM-CM5, which had approximately 10% excluded, typically during the months of July through October. The STR-L value was averaged between longitudes of 145-150°E. The narrow longitudinal window serves to focus on the region of interest here although we note that other studies, such as Kent et al. (2011) consider a much wider longitudinal extent in their definition of STR-L. To better determine the location of the maximum MSLP in the coarse resolution GCM models a quadratic fit was applied over five grid cells, centred at the maximum MSLP grid cell and including the two neighbouring cells to the north and south.

### 3.4.2 Southern Oscillation Index

The connection of the El Nino Southern Oscillation (ENSO) with the STR and meteorology and oceanography in this region is also investigated in this study. The Southern Oscillation Index (SOI) is calculated from the difference between MSLP at Tahiti and Darwin and provides one measure of ENSO (Troup, 1965). Values of SOI were sourced from the Australian Bureau of Meteorology (ftp://ftp.bom.gov.au/anon/home/ncc/www/sco/soi/soiplaintext.html).

## 3.5 Longshore Bedform Transport Analysis

Analysis of the repeat multi-beam surveys provided opportunity to indirectly measure the amount of sediment transport through shifts in the position of the bedforms. This subsection details how bedforms were identified, characterised and track to estimate the longshore transport.

### 3.5.1 Bedform identification

Hillside-shaded maps of the gridded multi-beam surveys were used to visually bring out the submarine bedform features from the sea floor for the five surveys at both sites (Figure 3.5). This method identified *dune* sized bedforms with wavelengths (trough to trough) on the order of tens of meters wide and tens of centimetres in height (trough to crest) superimposed over larger *sandwave* bedform with wavelengths of hundreds of meters and metres in height. The trains of successive dunes were ordinated with crest-lines normal (perpendicular) to the coastline and suggest the transport of the bedforms is parallel to the longshore surge-tide direction flow along the coastline.

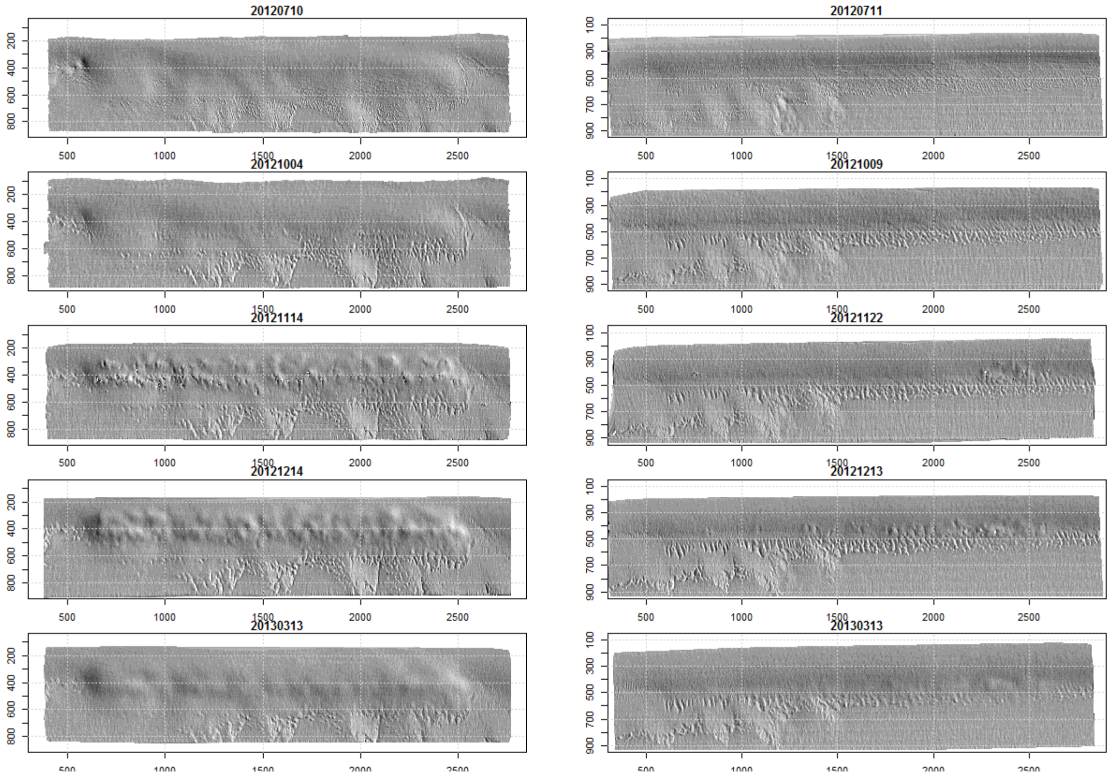


**Figure 3.5 Hill-shade maps of the multi-beam surveys.**

West (east) site surveys start in chronological order starting at the top of the left (right) column run down the column. Plan view of the surveys, horizontal axes is in the longshore direction and the vertical axes is in the cross-shore direction (distance from the shore), lighting source is from the top-right. Examples of the dredge spoil mounds are evident in the top half of the plot titled '20121114' at the west survey site (third from top). The sharp mounds dissipate and smooth out in subsequent surveys.

Quantitative analysis of the bedform characteristics was applied along each row of the gridded multi-beam datasets. Two smoothed-cubic-splines were applied to each row of the survey grid to model the continuous surface of the sandwave and dune bedform features (Regression, 1996). Splines were chosen over other curves (e.g. sinusoidal) because of their ability to represent the asymmetric shape of the bedforms. The smoothed spline fit $S_1$, modelling the background sandwave, had fixed spline knots to the survey data separated by 30 points (spanning 75 m). The spline fit $S_2$, modelling the dunes, had knots separated by three points (spanning 7.5 m). To display the dune field, represented by gridded seabed anomalies, the sandwave spline $S_1$ surface was removed from multi-beam survey grid. The contours of this seabed anomaly grid are plotted in

Figure 3.6 as alternative to the hill-shaded maps to bring out the dune bedforms (Figure 3.5). An example of the dune spline fitting $S_2$ to the multi-beam survey grid is provided in Figure 3.6.

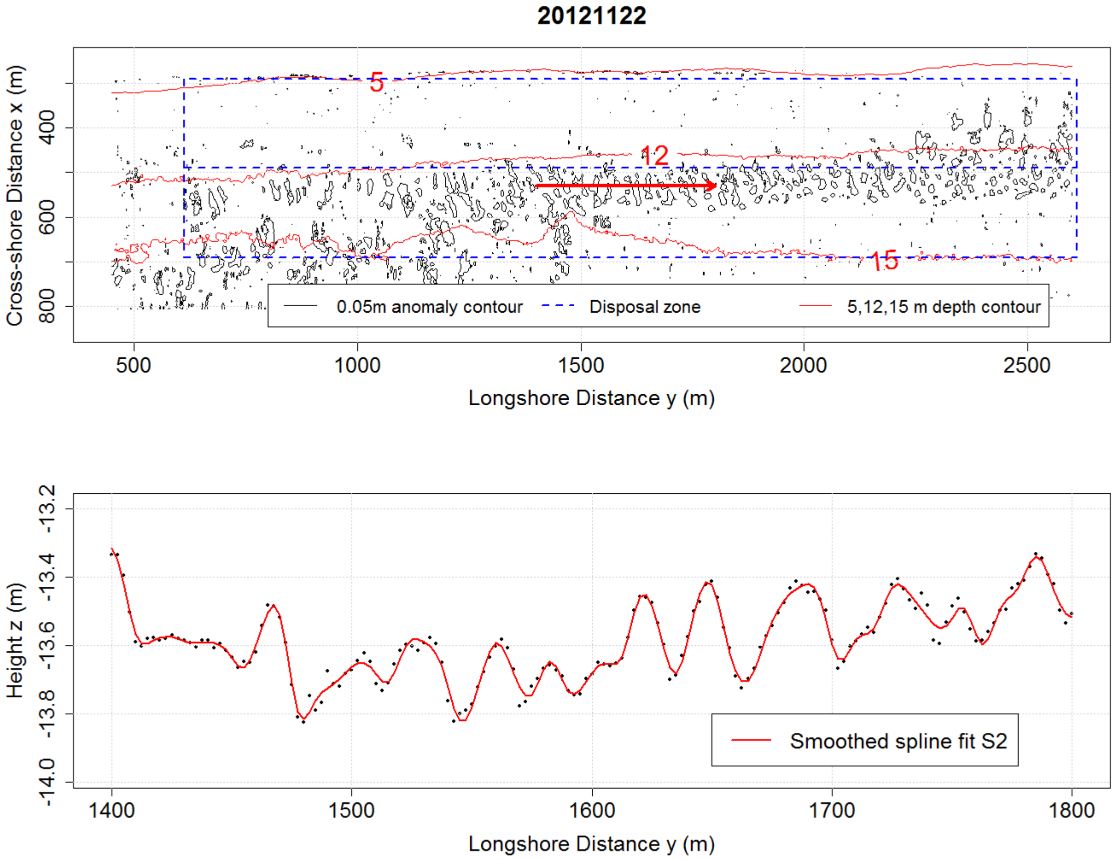


**Figure 3.6 Spline fit of the measured dune bedforms.**

Top, plain view 0.05m contour map (black contours) of the seabed anomaly grid representing the dunes. Dashed blue rectangular boxes outlines the east DMG region. Bottom, Longshore transect (corresponding to the red arrow in top) of the spline fit $S_2$ (red curved line) to the multi-beam survey grid row elevations (black dots). Data is from the East site 2012-11-22 multi-beam survey.

Bedform statistics were calculated between successive trough points on the $S_2$ dune spline curve (Figure 3.7). The trough points were identified when both the first derivative of the spline curve $S_2$ crosses zero ($S_2'=0$) and second derivative is greater than zero ($S_2'' > 0$). The crest points were first estimated halfway between troughs and then an optimiser (Brent, 2013) was used to refine/interpolate (between 2.5m gridded survey grid points) the position of both the crest and trough points where $S' = 0$.

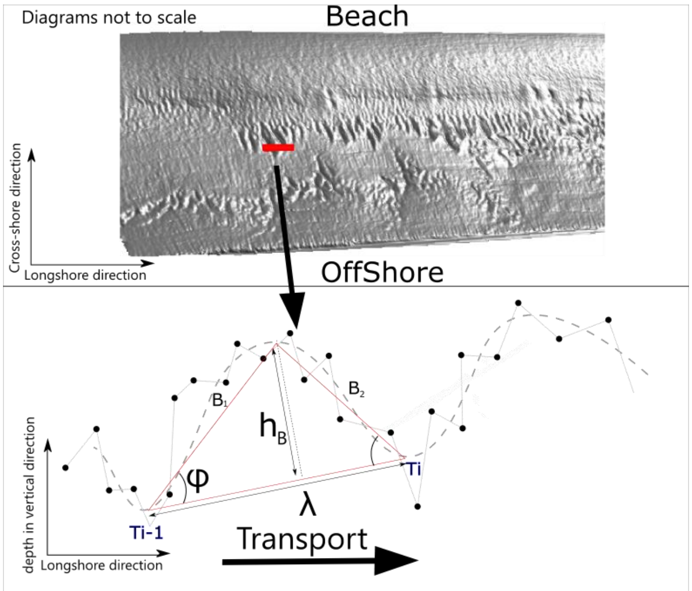


**Figure 3.7 Diagrams illustrating the identification of bedform characteristics.** Top, plan view hill-shade map of the dune field in the multi-beam survey. The thick-red line indicates the location of example transect. Below, profile view, row of gridded survey elevations (connected black dots), spline fit (grey dashed line) and idealised bedform (red triangle). Parameters are described in Equation 3-3.

Bedform characteristics detection and parameters are shown in Figure 3.7. The parameters were then calculated in a similar way to Duffy and Hughes-Clarke, (2012) with the following equations;

$$\lambda = \sqrt{(Ty_i - Ty_{i-1})^2 + (Tz_i - Tz_{i-1})^2} \qquad 3\text{-}3$$

$$B_1 = \sqrt{(Cy_i - Ty_{i-1})^2 + (Cz_i - Tz_{i-1})^2}$$

$$B_2 = \sqrt{\lambda^2 + B_1^2 - 2\lambda B_1 \cos\varphi}$$

$$\varphi = \tan^{-1}\left(\frac{Cz_i - Tz_{i-1}}{Cy_i - Ty_{i-1}}\right) + \tan^{-1}\left(\frac{Tz_i - Tz_{i-1}}{Ty_i - Ty_{i-1}}\right)$$

$$h_B = B_1 \sin\varphi$$

$$\Lambda = \frac{(B_2 - B_1)}{(B_2 + B_1)}$$

, where $\lambda$ is the bedform wavelength (Euclidean distance) between troughs; *Ty*, *Tz* are the bedform trough longshore location and depth respectively at points $i$ = 1,2,3 ... *number of crests*, *Cy*, *Cz* are the same parameters but for the bedform crest, $B_1$ and $B_2$ are the stoss and lee lengths, $h_B$ is the bedform height normal to the trough slope, $\Lambda$ is the asymmetry (Figure 3.7). For $B_2 > B_1 : \Lambda > 0$, $B_2$ is the stoss side, $B_1$ is lee side and flow direction was to the left, for $B_1 > B_2 : \Lambda < 0$, $B_1$ is the stoss side, *B2* is lee side and flow direction was to the right.

### 3.5.2 Bedform tracking

In each row of the gridded multi-beam survey, submarine bedforms were tracked at their crest points between successive surveys. There were two requirements of the automated tracking. The first was that the bedforms (dunes), did not move greater than half the wavelength of the bedform between the multi-month surveys, to avoid automated aliasing of bedforms. The second requirement was that the physical limits in bedform migration must be realistic and consistent with transport estimates elsewhere in the literature. The method of bedform tracking was to track to the nearest crest point ($Cy_i$) within a search window of $\pm\lambda/2$ in the successive survey, in the longshore y-direction. This method has been applied to multi-beam bedform movements normal to the crest line in tidal channels (e.g. Barnard and Erikson, 2012).

An example of the spline fit ($S_2$) to the multiple bedform train, is presented in Figure 3.8. This plot demonstrates the somewhat regular bedforms and their changes over three successive surveys. The crest-points of the splines were then tracked to show the longshore dune displacements $\Delta y$. The displacements $\Delta y$ were plotted against the depth of water and show a similar pattern of transport for both sites. The visual inspections of successive dune bedforms trains indicate that the first and last bedforms move the same distance as all the bedforms in the train (Figure 3.8). This distance is approximately of 1-2m between each survey and is less than half the wavelength of the bedform (20-40 m). The possibility that the bedforms could shift more than one wavelength (tens of meters) between surveys is low. This would require the last bedform in the train is washed out and a new bedform is generated at the start of the train. It would also imply the volume of transported sediment would be a factor of 10 larger than predicted. Predictions of bedform migration on the Canadian coast are meters per month in coastal waters between depths of 20-40m (Duffy and Hughes-Clarke, 2005). Hence a nearest crest-tracking window was set to ten metres either side of the crest.

Other tracking methods were tested, such as particle image velocimetry (Buijsman and Ridderinkhof, 2008; Duffy and Hughes-Clarke, 2005) which can track bedforms in two horizontal directions (cross- and longshore). The non-uniform tide-wave flow at the study site resulted in irregular bedform shapes, that didn’t retain their shape between surveys, hence the ‘finger print’ of the bedforms couldn’t be accurately detected between surveys.

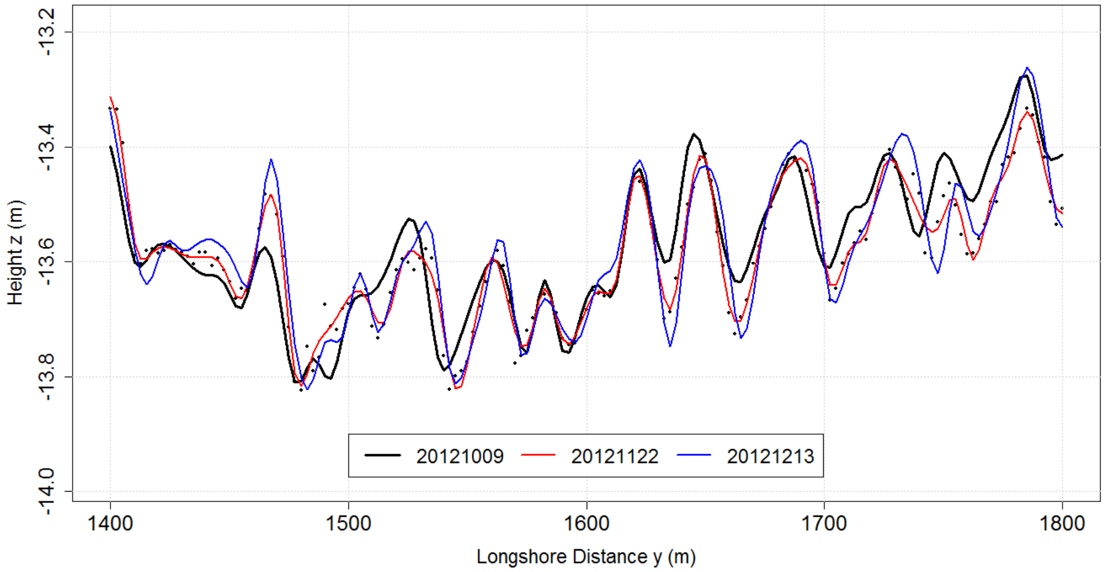


**Figure 3.8 Changes in bedform train in three successive surveys.**

Three longshore transects of the spline fits $S_2$ to the multi-beam survey grid row at the same transect line (Figure 3.6). The dates of the surveys are listed in legend. The dots represent the 2012-11-22 multi-beam grid elevations.

### 3.5.3 Estimating longshore transport

Transport is calculated from the approximate volume eroded ($V_{err}$) and deposited ($V_{dep}$) from a triangular bedform (Duffy and Hughes-Clarke, 2012). The equations to approximate transport are;

$$V_{err} = V_{dep} = h_B \Delta y \left(1 - \frac{\Delta y}{\lambda}\right) \qquad \text{3-4}$$

$$q_v = \frac{1}{\Delta t} V_{err}$$

, where $\Delta y$ is the displacement of the bedform crest in the longshore y-direction, $h_B$ is the bedform height, $\lambda$ is the bedform length, $q_v$ is the sediment discharge transport rate ($m^3 m^{-1} yr^{-1}$) and $\Delta t$ is the time (in years) between surveys. The transport was computed at the crest point of each row of the grid and then all computed transport values where binned into 1m depth ranges to summarise the statistics of transport. The longshore transport rate $Q_v$ is calculated mean transport averaged $q_v$ in the cross-shore direction, multiplied by the cross-shore distance bedforms exist (distance between depth contours). The somewhat regular shape of the bedforms will affect the estimates in Equation 3-4, so statistics of the mean and standard deviation of the population of bedforms at different depths are used to capture the accuracy of the bedform identified transport.

## 3.6 TELEMAC Model Configuration

In this section we describe the setup and implementation of the TELEMAC model introduced in Section 2.4. As a general overview, the model simulations were forced at the boundary by the hindcast datasets and run for the ~3.7 years of the surveys. The model was then rerun with GCM downscaled boundary conditions. The selection of model parametrisation was made by limiting tuning to the fewest parameters that control the largest model internal variability. Otherwise, the default settings where used.

### 3.6.1 Model Grid and Bathymetric Initialisation

Several grid configurations, with different domains and resolution were tested. The domain was chosen to cover the two DMG survey sites at the coast and the wave buoy and ADCP within the deep water boundary (Table 3-2). The resolution was designed to capture the larger bedform features. These include the storm-bar and trough, ‘The Bar’ ebb tidal delta and the 100-200m long sandwaves. The resolution was also designed to be computationally efficient to allow for a small Courant number for numerical stability (Figure 3.9). To do this, the grid has a resolution of 40m over the survey sites, which expands to 200m towards the boundary, in order to limit the number of ocean boundary points.

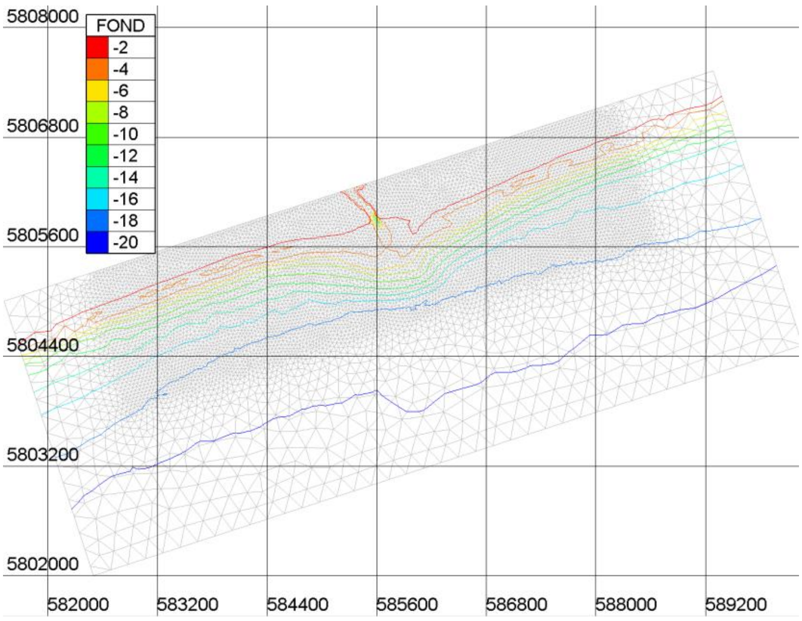


**Figure 3.9 TELEMAC model grid. Same grid for all three models.**

Map of 8.2km x 3.2km unstructured model grid, varying from 200m at the open domain to 40m around the survey sites. Coloured contours are the mapped LiDAR heights (see colour key insert titled ‘FOND’). Coordinates are UTM zone 55 south. See Table 3-2 for grid coordinates.

The model was run for 14 periods between 15 consecutive bathymetric surveys. The grid was initiated with the survey at the start of the simulation, with initiation dates provided in Table 3-3. All bathymetric mapping was performed with a nearest neighbour method, with a limited neighbour interpolation distance of 55m, and the minimum depth of 2 m. The surveys did not cover the whole model domain (e.g. Figure 3.10). So, two idealised profiles, either post-storm or after-calm conditions, from larger surveys were required for the non-surveyed grid points. The bathymetric profile with a large storm-bar (Figure 3.2), can be thought to have a 'winter' (post-storm) profile, as Austral-winter is when most large storms occur. However, a storm-bar can be present in Austral-summer months. In a like manner, a 'summer' (calm) profile, where the storm-bar is absent, can occur during winter months.

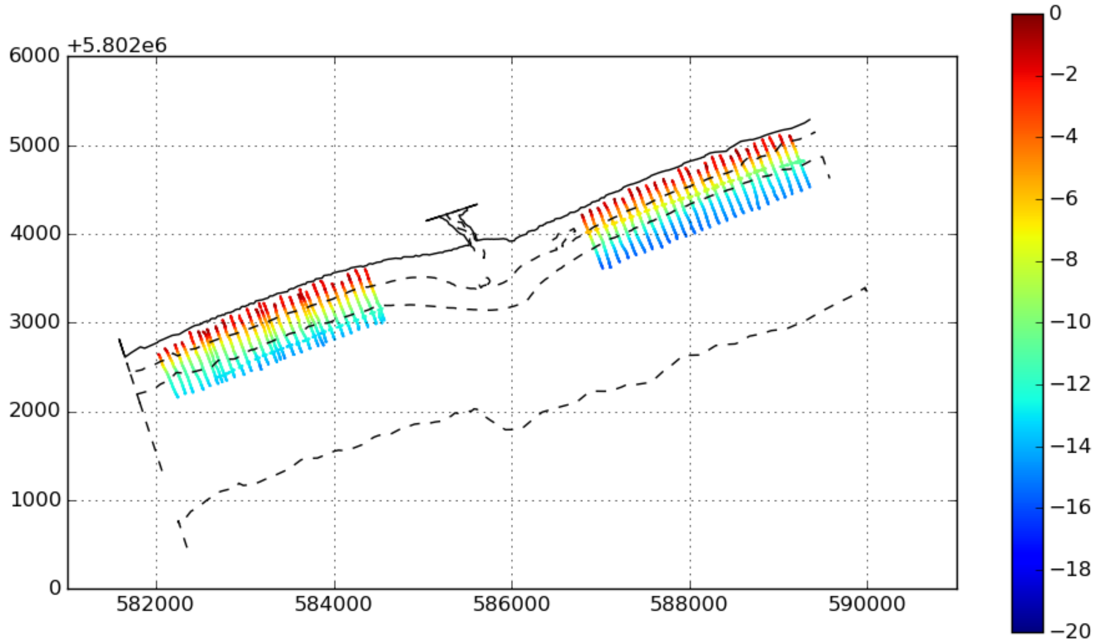


**Figure 3.10 Example of a single-beam survey of both west and east sites.**

Single-beam survey (GL5462) 2009-10-05 across both sites, transect surveys separated by ~100 m. The coloured, cross-shore transect lines correspond to survey height (m) on the colour key. Contour dash lines represent the 20, 12 and 5m depth contours.

The only complete bathymetric survey across the whole domain is the LiDAR survey conducted over the austral summer of 2008-2009. It represents the 'winter' storm-bar and trough profile. The most complete survey representing a 'summer' absent storm-bar and trough profile is the survey of 2011-03-29 (Figure 3.11). The difference between the 'summer' and 'winter' profiles is plotted in Figure 3.12.

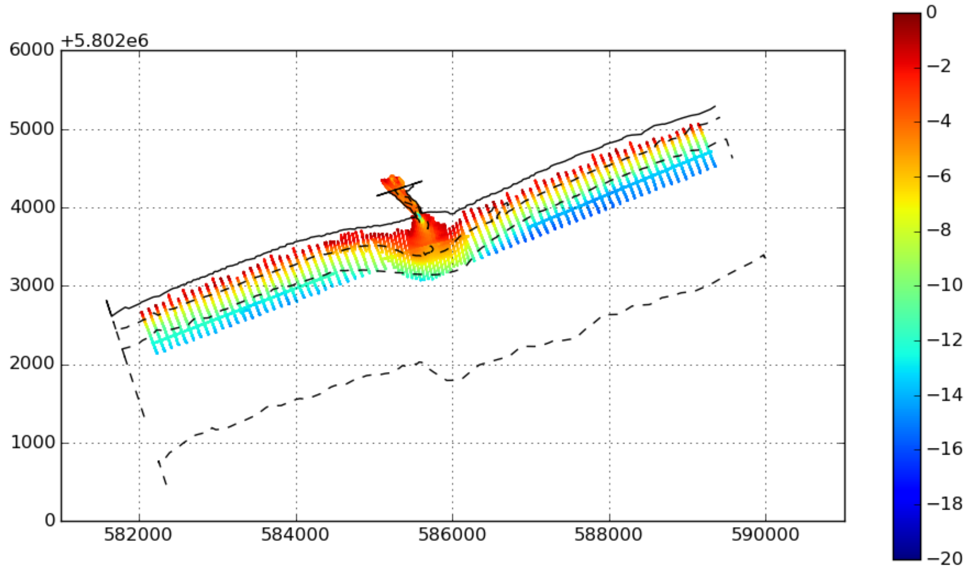


**Figure 3.11 Single-beam survey of 'summer' profile**

Survey (GL5563) 2011-03-29 represents the most complete wintertime survey across both dredge disposal sites and the bar. Contour dash lines represent the 20, 12 and 5m depth contours.

To best represent the changing profile across the entire model domain, the survey mapping was a three-step process. In the first step, the LiDAR data was mapped. In the second step, if the survey soundings used to initialise the simulation were identified to have a 'summer' profile then the 2011-03-29 survey was mapped. In the final step, the initial soundings were mapped onto the grid to initiate the simulations. The model grid is exactly the same for all three models (TELEMAC2D, TOMAWAC and SISYPHE).

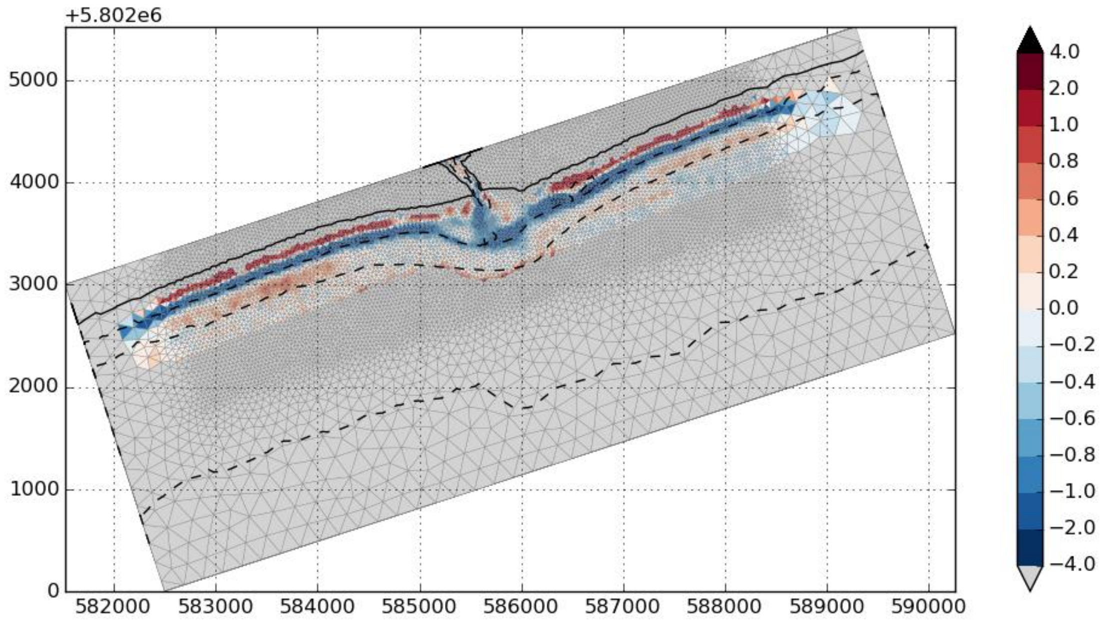


**Figure 3.12 Mapping the transects change from LiDAR**

The colours indicate the difference in bed elevation (in metres) of Survey GL5563 2011-03-29 'summer' profile from the LiDAR 'winter' profile. Reds (blues) indicate higher (lower) bed elevations in the GL5563 survey compared to LiDAR profile (see Figure 3.2 for profile view)

### 3.6.2 TELEMAC2D

The governing PDEs and model introduction are provided in Section 2.4.1. The type of numerical discretization used was quasi-bubble (4 node triangle) for velocity and linear (3 node triangle) for depth because of the strong bathymetric gradient. The numerical solution of the advection of velocity was solved with the default method of characteristics. The solver for the hydrodynamic propagation step was the default conjugate gradient on normal equation method. The model time step was set to 10s for efficiency and accuracy. Treatment of tidal flats is used in the simulations to account for changing water levels and the wetting and drying of land points.

Bottom friction is accounted for in TELEMAC2D model with quadratic drag law parametrisation. In the coupled TELEMAC system this is computed in SISYPHE, and for consistency with the drag coefficient computed in the sediment transport parameterisation (discussed in Section 3.6.4) the Nikuradse law of bottom friction is used (Nikuradse, 1933). The drag coefficient, plotted in Figure 3.13, is larger in shallower water, so the bed shear stress term reduces the flow in shallowing depths. The equations for bottom friction are;

$$\tau_{bx} = \frac{1}{2}\rho C_d u|\vec{U}| \qquad \textbf{3-5}$$

$$\tau_{by} = \frac{1}{2}\rho C_d v|\vec{U}| \qquad \textbf{3-6}$$

$$C_{dN} = 2\left[\frac{0.4}{\log\left(\frac{12h}{k_{sN}}\right)}\right]^2 \qquad \textbf{3-7}$$

, where $\rho$ =1020 kg/m$^3$ is the density of water, $k_{sN}$ = 0.05 m is a tuneable bed roughness coefficient.

Wave stress, another source term of momentum, is provided by wave shoaling and depth-induced breaking. The formulation for this term is provided by the TOMAWAC wave model (see next section).

The final term of the momentum shallow water equations (Equations 2-2 to 2-3) corresponds to the diffusion of the velocities. The tuneable coefficient $v_t$ controls the extent and shape of recirculation. In the simulation presented, viscosity is assumed to be constant with time across the whole domain. Small eddies are dissipated with smaller values of $v_t$ while larger recirculation is controlled by larger values. In preliminary tests, different values of velocity diffusivity (molecular + turbulent viscosity) were tried to control the flow. The 40m horizontal resolution allows for the dynamic modelling of eddies and for a small viscosity value. In the end, other model configurations (e.g. time step, numerical schemes, wave processes and boundary setup) were seen as the sources of instability and the default value $10^{-6}$ was used. This value corresponds to the molecular viscosity of water.

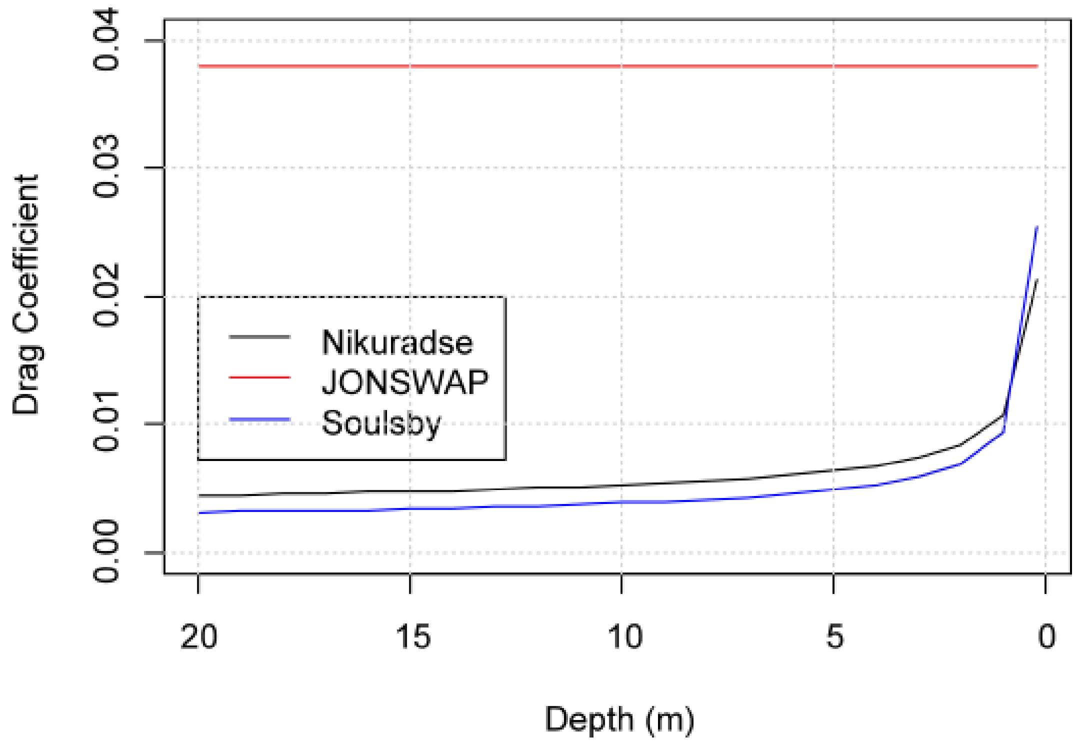


**Figure 3.13 Different model drag coefficients with varying depth.**

Plotted are the quadratic bottom friction coefficient for TELEMAC2D defined by Nikuradse (black line), constant wave bottom friction coefficient for the TOMAWAC model defined in the JONSWAP campaign (red line) and drag coefficient applied to the wave orbital velocity for the SISYPHE model defined by Soulsby (Blue).

Boundary conditions of water levels and currents were sourced from a five-kilometre-resolution, regional hindcast of storm tides around Australia using the ROMS model (Section 3.2.3). Longshore coastal currents were generated within the grid by applying a longshore gradient in the water levels from two neighbouring ROMS grid points. Also, the flow was modified by prescribing flow velocities in and out of the boundary. In preliminary model setups, the coastal-current velocities and water levels were prescribed at all the boundary points, but yielded poor advection into the domain, because the boundary was too constrained. The Thompson method was tested but did not completely remove the undesirable flow patterns in the domain. The Thompson method uses the theory of characteristics to obtain a consistent water level and velocity value at the boundary. In order to free up the flow constraint, the model source code was modified, to prescribed and free flow boundaries depending on the down flow direction of the ROMS flow velocities (Figure 3.14). The different boundary conditions are discussed in the results section (Section 6.1).

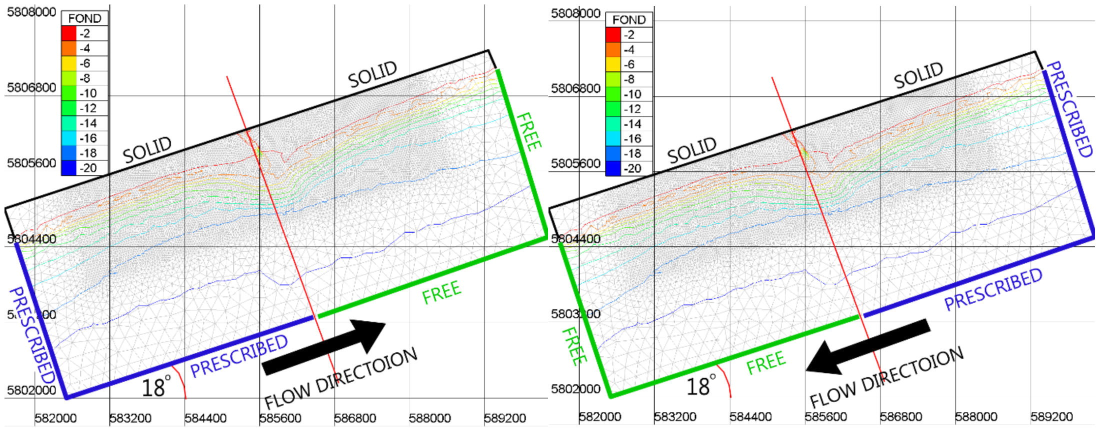


**Figure 3.14 TELEMAC2D alternating flow boundary forcing.**

The plot on the left (right) is the boundary conditions for eastward (westward) ROMS forced flow. The gradient in the water level (free surface) doesn't have an altering boundary and is prescribed for all non-solid (non-land) points.

### 3.6.3 TOMAWAC

The governing equations for the wave propagation in the TOMAWAC model are described in section 2.4.2. The 2D spectral wave model TOMAWAC was forced at the open sea boundary (Figure 3.15) by 2D (direction and frequency) spectral output from WW3 hourly ½-degree gridded global wave hindcast (Section 3.2.2). Both the boundary data and the model used a matching wave spectrum, divided into 18 direction and 26 frequency bins.

The wave source terms of wind generation and long-fetch processes (e.g. quadruplets and dissipation by white capping) are captured in the global WW3 hindcast data, which was applied to the nearshore model boundary. Further contributions of long-fetch processes within the nearshore grid domain were found to be insignificant, and so therefore are not turned on in the nearshore grid. Only the nearshore processes of bottom friction and depth-induced breaking were used for the final simulations. However, triad wave interaction (Eldeberky and Battjes, 1995) and dissipation by strong currents (Van Der Westhuysen, 2012) were tested but produced unsatisfactory results for the required model resolution. The formulation of the source terms for depth-induced breaking and bottom friction reduce the overall wave energy as the waves approach the coast. However they do not affect the distribution (shape) of the energy frequency and direction spectrum. Triad interactions will generally induce a second peak at two times (and higher multiples) of the peak frequency, shifting wave energy from low to higher frequencies.

The commonly used bottom friction equation for wave dissipation was used in this study (Bouws and Komen, 1983). Bottom friction-induced dissipation ($\tilde{Q}_{bf}$) is the reduction in wave energy due to roughness of the seabed and was calibrated during the JONSWAP campaign;

$$\tilde{Q}_{bf} = -\Gamma\left(\frac{\sigma}{g\sinh kh}\right)^2 \tilde{F} \qquad \textbf{3-8}$$

, where Γ is the JONSWAP constant of 0.038 $m^2$ $s^{-3}$ which is constant with depth (Figure 3.13) and g is the gravitational acceleration 9.8 $ms^{-2}$. The equation is based on the quadratic drag law, where the analytical solution of the orbital wave velocity from linear wave theory (within the parenthesis) is squared and multiplied by a constant friction factor Γ to reduce the wave spectrum $\tilde{F}$. Sensitivity tests were made with different friction parameters considering the work of Smith et al., (2011). However, most of the internal model variability came from the breaking parameter (discussed next). For simplicity, the default value from the JONSWAP experiments was used.

TOMAWAC provides four methods for parametrising depth-induced wave breaking. Sensitivity tests led to the selection of the frequently used Battjes and Janssen's (1978) model. However, results from the Izumiya and Horikawa's (1984) model were analysed and presented for comparison. The formulation of the Battjes and Janssen model is;

$$\tilde{Q}_{bb} = \frac{\alpha Q_b f_c H_m^2}{4m_0}\tilde{F} \qquad \textbf{3-9}$$

$$H_m = \begin{cases} \gamma h, \\ \gamma k_c \tanh\left(\frac{k_c h}{\gamma}\right) \end{cases} \qquad \textbf{3-10}$$

$$\frac{1-Q_b}{\ln Q_b} = \left(\frac{H_{m0}}{\sqrt{2}H_m}\right)^2 \qquad \textbf{3-11}$$

$$\frac{1-Q_b}{\ln Q_b} \approx -Q_b{}^{\frac{1}{2.3}} \to Q_b \approx \left(\frac{H_{m0}}{\sqrt{2}\gamma h}\right)^{4.6} \qquad \textbf{3-12}$$

, where $H_m$ is the maximum wave height in a given water depth, $\gamma$ is the depth-induced wave breaking parameter, $k_c$ is the intrinsic wave number ($2\pi/L$) and $Q_b$ is the fraction of breaking waves.

The basic criterion for bathymetric-induced breaking (Equation 3-10) is that waves will break when the breaking ratio ($\gamma$) between the height of a solitary wave ($H$) and the water depth ($h$) is around 0.78 (Munk, 1949). This criterion forces a limit to the height of waves within the surf zone ($H = \gamma * h$). Izumiya and Horikawa, (1984) show that this criterion can be extended to a weak dependence of bathymetric breaking from wavelength and wave steepness (wave height over wavelength). To account for wave steepness in the Battjes and Janssen model, the Miche criterion was included (Miche, 1944). The Miche criterion (Equation 3-10), modifies the breaking parameter from the effect of wave steepness, which allows larger waves in a given depth than the ratio (γ) permits. The forcing from the wave model to the hydrodynamics comes through the radiation stress force equations;

$$T_{xx} = g \int_{f_r=0}^{\infty} \int_{\theta=0}^{2\pi} \left[ n(\sin^2\theta + 1) - \frac{1}{2} \right] \tilde{F} \, \mathrm{d}f_r \mathrm{d}\theta \qquad \textbf{3-13}$$

$$T_{yy} = g \int_{f_r=0}^{\infty} \int_{\theta=0}^{2\pi} \left[ n(\cos^2\theta + 1) - \frac{1}{2} \right] \tilde{F} \, \mathrm{d}f_r \mathrm{d}\theta \qquad \textbf{3-14}$$

$$T_{xy} = g \int_{f_r=0}^{\infty} \int_{\theta=0}^{2\pi} [n \sin\theta \cos\theta] F \, \mathrm{d}f_r \mathrm{d}\theta \qquad \textbf{3-15}$$

$$\tau_{wi} = -\frac{1}{h}\left( \frac{\partial T_{ii}}{\partial x} + \frac{\partial T_{xy}}{\partial y} \right) \quad , i = x, y \qquad \textbf{3-16}$$

, where the wave force $\tau_{wi}$ in the $i^{th}$ (*x* or *y*) coordinate is the sum of the spatial change in the radiation stress $T_{ii}$. The radiation stress ($T_{ii}$) is a function of the integrated wave shoaling (*n*) and spectral energy, which can be considered as an equivalent to spectral significant wave height. It follows that large values of the wave force will occur when there are large spatial changes in significant wave height. The largest spatial changes in spectral significant wave height come from depth-induced breaking on steep profiles. As a consequence, the largest wave forces applied to the hydrodynamic model are controlled by the wave breaking parameter. The parameter γ, determines which part of the (sometimes exponentially) steepening bathymetric profile, wave height (energy) will be reduced, so where the strong wave-driven force is applied.

The TOMAWAC modelled integrated parameters of *Hs*, peak period (*Tp)* and peak wave direction (*θp)* are passed on to the morphodynamic model SISYPHE to compute the wave orbital velocity for sediment transport;

$$U_o = \frac{H_{m0}(2\pi f_c)}{2\sinh(kh)} \qquad \textbf{3-17}$$

The spectral wave model has a main time step for convection (propagation) of the wave field (Equation 2-4). It also has a second time step (sub-step) for the integration of all source and sink terms and a third time step (sub-sub-step) for the nonlinear source terms ($\tilde{Q}_{bb}$, $\tilde{Q}_{tr}$ and $\tilde{Q}_{cb}$). The boundary WW3 spectrum had a resolution of 1hr and effective model propagation was achieved with the step set to the same temporal resolution. The number of source-terms sub-step iterations was set to 10, to better resolve the dissipation. These time sub-steps are arranged in a geometrical progression, and the geometric ratio of one source solution to the next was increased from the default of 1.54 to 3 to reduce the overestimation of dissipation per time sub-step.

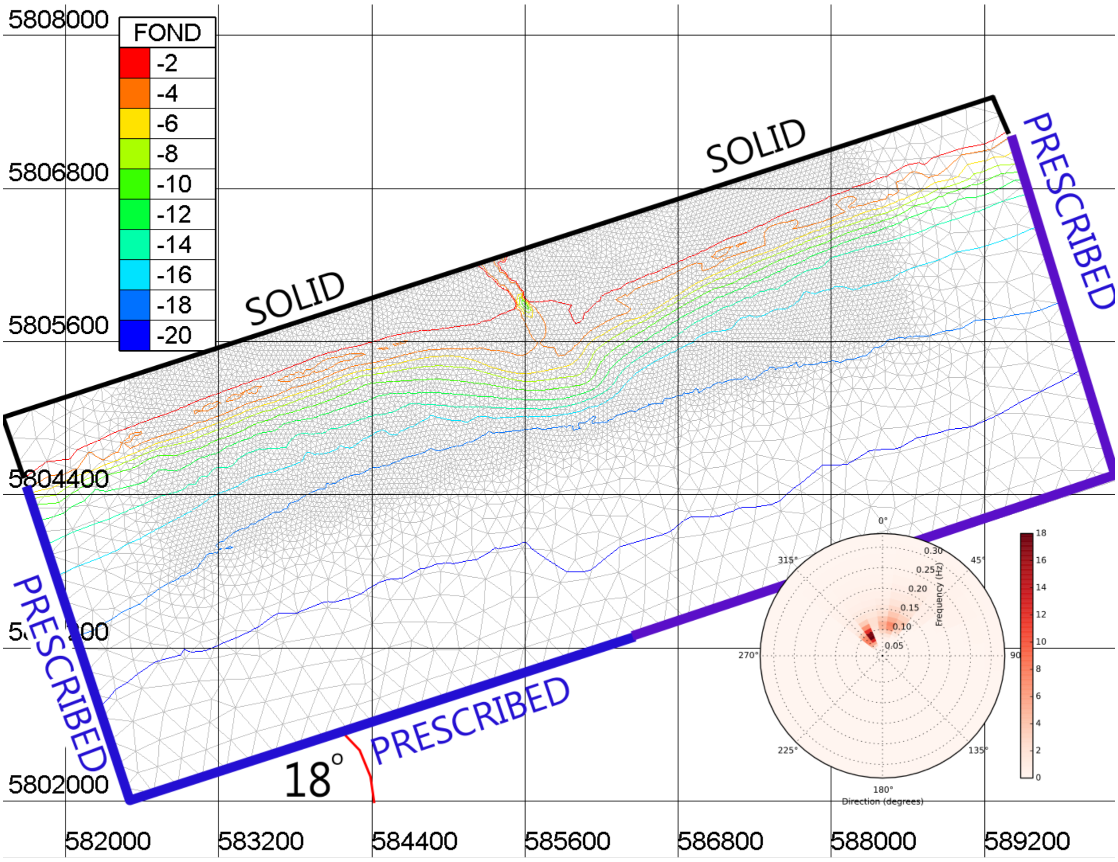


**Figure 3.15 TOMAWAC spectral wave boundary forcing.**

The two-dimensional wave energy spectrum was prescribed along the boundary of the grid in waters deeper than 1m, show in blue (above). An example 2D wave spectrum is inserted in the lower left. The coloured depth contour lines correspond to the colour key labelled FOND.

### 3.6.4 SISYPHE

The governing equation for bed evolution (bathymetric change) in SISYPHE is provided in section 2.4.3. The morphodynamic time step is the same as the 10s TELEMAC2D hydrodynamic time step.

Both waves and coastal currents modify sediment transport in the nearshore region and SISYPHE provides a number of empirical and dynamical (PDE) equations to resolve these effects. Suspended sediments can be modelled more dynamically by adding a tracer equation (convection-diffusion) to the TELEMAC2D transport equations. The additional tracer equations come at the cost of a large computational overhead. For efficiency, the sediment-concentration tracer equations were not used in the results presented. The Soulsby Van Rijn (Soulsby, 1997) formulae (equations 3-18 to 3-30) were chosen for this study because, among other things, they can be used to simply estimate the suspended-load (3-20) contribution to the bed-load (Equation 3-19) components of the total sand transport (equation 3-18). The Soulsby Van Rijn define transport as;

$$q_T = (q_b + q_s) \quad , for\ each\ class\ of\ d_{50} \tag{3-18}$$

$$q_b = A_b \dot{U} \left| \vec{U} \right| \tag{3-19}$$

$$q_s = A_s \dot{U} \left| \vec{U} \right| \tag{3-20}$$

$$\dot{U} = \left[ \left( \left| \vec{U} \right|^2 + \frac{0.018}{C_{ds}} U_O^2 \right)^{0.5} - U_{cr} \right]^{2.4} \tag{3-21}$$

$$C_{ds} = \left[ \frac{0.4}{\log\left(\frac{h}{k_{ss}}\right) - 1} \right]^2 \tag{3-22}$$

$$A_b = \frac{0.005h(d_{50}/h)^{1.2}}{((\rho_s/\rho - 1)g d_{50})^{1.2}} \tag{3-23}$$

$$A_s = \frac{0.0012h d_{50} D_*^{-0.6}}{((\rho_s/\rho - 1)g d_{50})^{1.2}} \tag{3-24}$$

$$U_{cr} = \begin{cases} 0.19 d_{50}^{0.1} \log_{10}\left(\frac{4h}{D_{90}}\right), & 0.0001 \leq d_{50} \leq 0.0005 \\ 8.5 d_{50}^{0.6} \log_{10}\left(\frac{4h}{D_{90}}\right), & 0.0005 \leq d_{50} \leq 0.0020 \end{cases} \tag{3-25}$$

$$d_{50,i} = (0.0003, 0.0004, 0.0008) \tag{3-26}$$

$$D_{50} = \sum_{i=1}^{3\ classes} P_i d_{50i} \tag{3-27}$$

$$\sum P_i = 1, \tag{3-28}$$

$$0 < P_i < 1$$

$$P_1 = 0.5, for\ h > -12, else\ 0$$

$$P_2 = 0.5$$

$$P_3 = 0.5, for\ h < -12, else\ 0$$

$$D_{90} = \frac{(0.9 - \sum_1^{i-1} P_i)}{P(ci)} (d_{50i} - d_{50(i-1)}) + d_{50(i-1)} \tag{3-29}$$

$$D_* = d_{50i} \left[ \left( \frac{\rho_s}{\rho_s - \rho} \right) \frac{g}{v} \right]^{1/3} \tag{3-30}$$

, where sediment transport ($q_T$) is the sum of the bedload ($q_b$) and suspended load ($q_s$) transport for each sediment median grain size ($d_{50}$) class (in metres) and population ($P_i$) percentage.

Both the bed-load and suspended-load transport are activated when root sum squares of the current speed and scaled-wave-orbital-velocity exceed a critical velocity, $U_{cr}$ (equation 3-21). Within each grid cell there could be up to three sediment classes, and for each class, a different critical velocity for mobility (Figure 3.16). The critical velocity is defined by the sediment properties and depth of water (Figure 3.17).

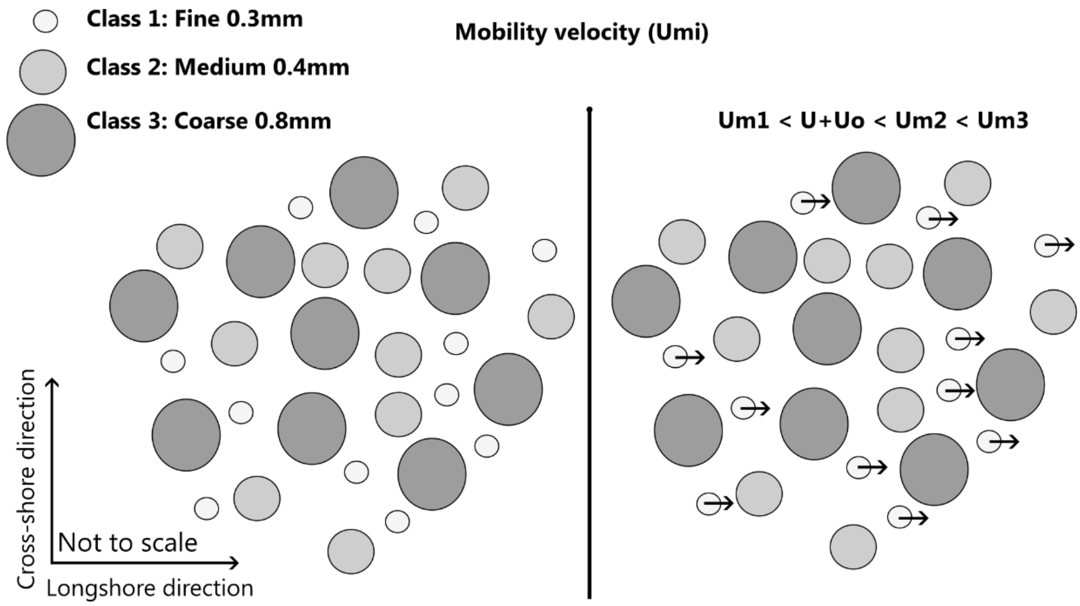


**Figure 3.16 Critical mobility diagram.**

This plot shows the conceptual configuration of three sediment classes in each cell. The right hand side show the example condition where the combination of the mean current and orbital velocities are strong enough to move only the finest sediment class (see Equation 3-25).

To replicate the cross-shore varying sediment grain size described in Section 3.1.5.1 three sediment classes are defined based on the descriptive stratigraphy given by Bird (1978), plotted in Figure 3.18. The populations of the three sediment classes (defined in Equation 3-28) were divided into two zones at the 12m-depth contour. In waters shallower than 12m, there was 50% fine ($d_{50,1}$=0.3 mm) and 50% medium ($d_{50,2}$=0.4 mm) sand grain sizes. In waters deeper than 12m there were 50% medium ($d_{50,2}$=0.4 mm) and 50% coarse ($d_{50,3}$=0.8 mm). Summing the sediment populations in Equation 3-27 resulted in an initial $D_{50}$ of 0.035mm in waters less than 12m and 0.6mm in waters deeper than 12m (Figure 3.18). A second combination of sediment classes was tested to measure internal model sensitivity, with a smaller fine-sediment class ($d_{50,1}$=0.25 mm), larger medium-sediment class ($d_{50,2}$=0.5 mm) and a smaller coarse-sediment class ($d_{50,3}$=0.7 mm).

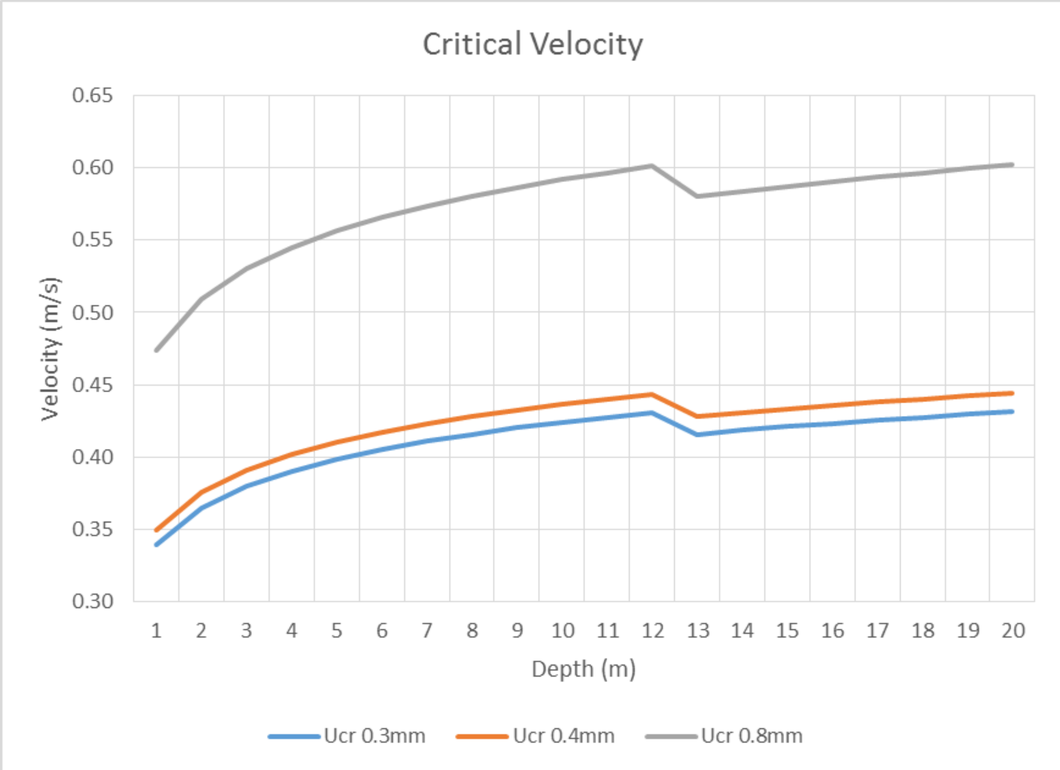


**Figure 3.17 Critical mobility velocity with depth.**

The critical velocity for sediment mobility is different for the three sediment classes (fine medium and coarse grain), and increases with increasing depth (Equation 3-25). The $D_{90}$ value strongly impacts the critical velocity at the 12m contour where the sediment class populations change.

Once the critical velocity is exceeded, the main driver of the sediment transport magnitude is the current velocity (both wave-orbital and wind- tide- driven). Secondary divers are the scaling parameters $A_b$ and $A_s$, defined by the sediment properties and depth.

In the calibration process, $q_T$ was found to underestimate the surveyed seabed evolution by a multiple of 20. This difference could be explained by the use of constant horizontal viscosity $\upsilon_t(10^{-6})$ across the domain (Section 3.6.2), where field studies have measured a value in the vertical direction ~100 times greater within the surf zone (Wright *et al.*, 1986). Kinematic viscosity $\upsilon$ has also been noted to be 100 times larger when there is sediment in the water column during large wave events (van Rijn, 2013). With this underestimation of $\upsilon$, the dimensionless grain size $D_*$ (Equation 3-30) would be overestimated, leading to an underestimation of $A_s$ (Equation 3-24) and therefore suspended transport $q_s$ (Equation 3-20) by a multiple of ~30 during large wave events. The increased eddy viscosity at the bed level would also impact bed load transport, which cannot be accounted for in the Soulsby Van Rijn transport equations. Hence $q_T$ was multiplied by 20 to improve the models ability to replicate the bed evolution surveys and represent an increased viscosity/diffusivity in the sediment transport model.

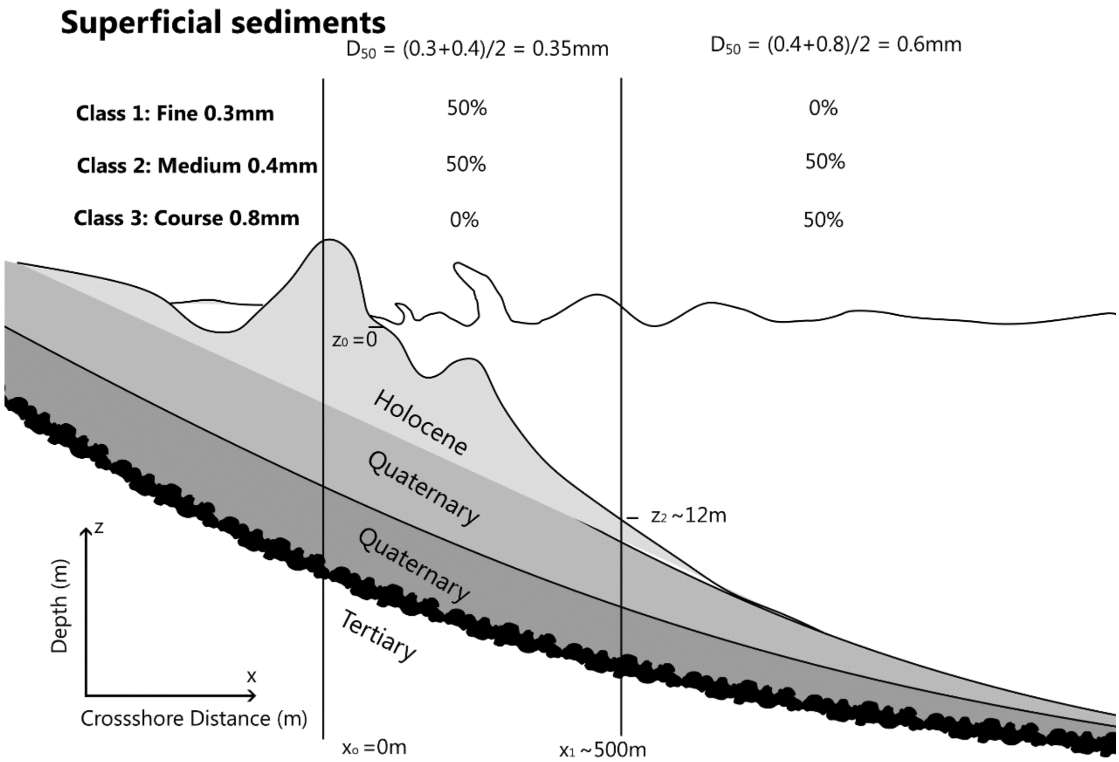


**Figure 3.18 Idealised diagram of Superficial Sediments.**

This figure shows a cross-section diagram displaying the description of superficial sediments given by Bird (1978). The model domain was split into two zones divided at the 12 m-depth contour. 50-50 percentage of two class (Equation 3-28) is given with each zone. The initial $D_{50}$ is given as the average of the two class $d_{50}$ in each zone. A second set of sediment classes were tested, with class one 0.25 mm, class two 0.5 mm and class three 0.7 mm. Diagram is not to scale.

### 3.6.5 Future Climate Simulations

The future climate simulations had the same model setup as the hindcast simulations, except that the boundary data was downscaled (forced) from the GCM by a change factor (CF) method applied to the 3.7 year hindcast data (Anandhi et al., 2011). Here we described how the normalised GCM climate change signal identified by Equation 3-2, is applied to the WW3 and ROMS hindcast boundary data. A schematic of a simplified coupled model flow chart (Figure 2.3) with the climate change boundary forcing for the climate simulations is shown in Figure 3.19. The model was run with different combinations of climate forcing to separate out the sensitivity of the increase in water levels representing mean sea-level rise, changes to the longshore current and changes to wave-driven transport calculated by the method described in Section 3.3.

Future climate simulations forced with sea level rise were achieved by simply adding the value of sea level increase to the boundary free surface water level data. While estimates of global mean sea level rise for the period 2081–2100, compared to 1986–2005, is likely (medium confidence) to be in the 5 to 95% range of projections from process-based models, which give 0.26 to 0.55 m for RCP2.6 and 0.45 to 0.82 m for RCP8.5 (Church *et al.*, 2013). For RCP8.5, the rise by 2100 is 0.52 to 0.98 m with a rate during 2081–2100 of 8 to 16 mm $yr^{-1}$. Increasing the water level by an additional one metre would result in a separation of the bottom sediment transport from the water surface waves within the 3.7 year climate simulation, whereas the natural climate sea level rise would gradually change over decades. Instead it was decided to use an instantaneous increase in SLR that is less than the tidal amplitude.

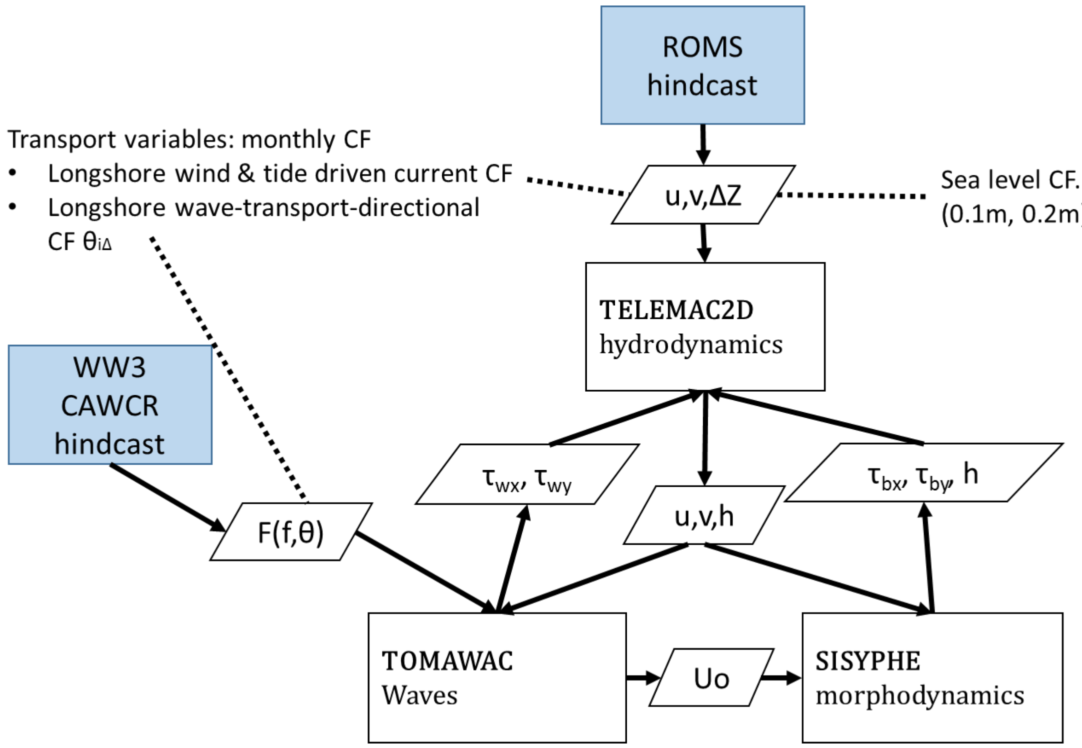


**Figure 3.19 TELEMAC climate change model forcing diagram.**

The ROMS hindcast wind-tide- driven current and WW3 hindcast waves are modified by the change factor method to simulate the shift in transport. The hindcast sea levels are offset by 0.1m to simulate the effect of sea level rise.

The additional CF for the future longshore current forcing was found by rearranging Equation 3-2 and replacing the monthly climate model baseline statistics (mean and standard deviation) with the hindcast longshore current data. Future longshore currents are therefore defined by the following equation;

$$F_{HU} = A \cdot \mathrm{sd}(B_{HU}) + B_{HU} \qquad \textbf{3-31}$$

, where $F_{HU}$ is the hourly time series of the imposed future longshore current speed, A is the GCM derived mean normalised anomaly for a given month from Equation 3-2, sd($B_{HU}$) is the standard deviation of the ~30 years of monthly-mean hindcast data, and $B_{HU}$ is the hourly time series of the hindcast data. The changes ($B_{HU}$) were added as a vector to the longshore grid direction on the prescribed flow boundary.

For waves, the CERC longshore wave transport equation was used in the normalised climate change analysis (Equation 3-2) and was a function of both the breaking wave height ($H_{sb}$) and breaking incident wave direction ($\theta_{ib}$) (U. S. Army corps of Engineers, 1984). The CERC equation is written as;

$$Q_w(H_b, \theta_i) = K_s H_{sb}^{5/2} \, sin(2\theta_{ib})/2, \qquad \textbf{3-32}$$

$$K_s = \frac{0.023 g^{1/2}}{(s-1)},$$

, where $g$ = 9.8 m/s$^2$ is acceleration due to gravity and $s$ = 2.6 is the ratio of sediment and water. $H_{sb}$ is assumed to have the value of the nearshore $H_s$ and $\theta_{bi}$ is calculated from the nearshore mean wave direction ($\theta$) clockwise from true north such that $\theta_{bi}$ equals $\theta$-$\theta_N$, where $\theta_N$ is the angle of the shore normal.

TELEMAC was forced with 2D wave spectral (frequency and direction) boundary conditions and the GCM normalised wave change analysis was summarised by the single bulk CERC parameter of $Q_w$ (a function of two parameters, *Hs* and $\theta$). A 2D spectrum can be altered by rotating the spectral direction bins, or by increasing the overall energy bins (i.e. *Hs*), or both. Ideally, in order to reduce complexity, the CF method is applied to one wave parameter rather than both *Hs* and $\theta$. So for simplicity in the TELEMAC model setup it was assumed that the change in the GCM derived CERC $Q_w$ can be entirely defined by an offset in wave climate direction alone. This was done so that the applied direction offset of the 2D spectrum ended up with the same resulting change in TELEMAC derived $Q_w$ as the CERC $Q_w$, even without a change in the spectral energy (i.e. *Hs*). Given this assumption, where the GCM identified increases (decreases) in CERC derived $Q_w$ which result from larger or smaller *Hs*, the change was instead accounted for in TELEMAC by an increased or decreased offset in the spectral angle in the longshore direction. This 'wave-transport-directional' CF ($\theta_{\Delta}$) term is different to a simple change in the mean wave direction, as it takes into account changes in wave height to modify the longshore transport. For the future longshore wave transport, equation 3-32 is written as;

$$F_{QH} = Q_w(H_{sH}, \theta_{iH} + \overline{\theta_\Delta}) \qquad \textbf{3-33}$$

, where $F_{QH}$ is the hourly time series of future mean longshore wave transport resulting from the hourly input from the wave hindcast $(H_{sH}, \theta_{iH})$ and the monthly mean offset in wave-transport-directional CF ($\theta_\Delta$). Monthly means are accented with a bar above the variable. Future longshore wave transport can be solved a second way. By using equation 3-2 again, we can solve for the CF change applied to the hindcast;

$$F_{QH} = A \cdot \mathrm{sd}\left(\overline{Q_w(H_{sH}, \theta_{iH})}\right) + Q_w(H_{sH}, \theta_{iH}) \qquad \textbf{3-34}$$

, where $A$ is the GCM-derived mean normalised anomaly for a given month from Equation 3-2, sd is the standard deviation of the monthly-mean longshore transport across each of the ~30 years. The monthly value of $\theta_\Delta$ (Equation 3-33) was found numerically by minimising (optimising) the absolute error between Equation 3-33 and 3-34. The optimisation method of Nelder and Mead was implemented using the statistical software package R (Nelder and Mead, 1965).

To generate the future rotated 2D wave spectrum, the monthly mean $\theta_\Delta$ was subtracted from the direction coordinate of the hindcast 2D wave spectrum. This spectrum (with the shifted direction coordinates) was then interpolated back onto the original direction coordinates. In this linear interpolation process, the spectrum was tiled (repeated in sequence) three times along the directional coordinate (-360° to 720°) to avoid issues crossing -1° in the direction from 1° to 360° and crossing +1° from 360° to 0° in the opposite direction.

## 3.7 Semi-empirical NMB-LM equation

The empirical CERC equation (Equation 3-32) was compared to the TELEMAC longshore transport estimates and then reformulated to include the effect of longshore wind- and tide- driven currents to better represent the transport modelled by TELEMAC. Once calibrated, the updated CERC equation (NMB-LM) was used to extrapolate the ~3.7 yr TELEMAC hindcast simulation to the full ~30 yr WW3 and ROMS hindcast datasets, to get a larger picture of the transport climate estimated by TELEMAC. It was then used with CF input wave and flow parameters to estimate the effect of climate change on the longer ~30 yr hindcast. The reformulated empirical flow equation was composed of the following;

$$Q_{wu} = D_1 K_s H_s^{D_2} \frac{sin(2\theta_i D_3)}{2} + D_4 U_l |U_l| \left| D_1 K_s H_s^{D_2} \frac{sin(2\theta_i D_3)}{2} \right| \qquad \textbf{3-35}$$

, where $D_1$, $D_2$, $D_3$ and $D_4$ are the calibrated values and $U_l$ is the longshore current velocity, positive (negative) eastward (westward).

The parameters of *D* were found by minimising (optimising) the absolute error between the TELEMAC simulated longshore transport and Equation 3-35 with the bulk WW3 and ROMS hindcast parameters. The optimisation method of Nelder and Mead, (1965) implemented in the statistical software package R, was used.

The first term on the right of Equation 3-35 is the CERC equation scaled by $D_1$ and has $Hs$ increased from the power of 5/2 to $D_2$. Different expressions of the power of Hs have been explained by Kamphuis, (1991) and Kamphuis et al., (1986). The power of Hs was increased because the CERC equation predicted more transport than TELEMAC during low compared to large wave conditions. The incident angle ($\theta_i$) is also scaled down by $D_3$ because the offshore waves input in ~20m of water have a greater incident angle to the coast than the required CERC wave breaking angle. The second term on the right of Equation 3-35 is the product of the longshore current $U_l$ , a scale parameter $D_{3,}$ the absolute value (magnitude) of $U_l$ and the absolute value of the first term on the right (scaled CERC wave term). This formulation replicated the TELEMAC-derived transport, where the longshore flow ($U_l$) only had a significant effect when the wave transport is large.

# 4. REGIONAL LONGSHORE TRANSPORT CLIMATE VARIABLITY AND CHANGE

This chapter analysis the performance of the hindcast and GCM modelled data and then provides a description of the longshore winds, waves and currents for the present and future climates. The data presented in this chapter will be used as input to the sediment transport models in Chapters 6 and 7.

## 4.1 Hindcast Model Performance

Assessing the similarity of model data to *in-situ* observations is made using the Pearson's r correlation statistic. The significance of the correlation is assessed by testing if the outcome of the correlation is of random chance with the Pearson's P probability statistic. If the P statistic is less than 0.01 (1%) then there is less than a one-in-one hundred probability that the observed relationship happened by chance, hence the findings are highly significant. In this study all correlations presented were found to be highly significant given the length of the datasets and resulting degrees of freedom.

### 4.1.1 Meteorological Fields

Meteorological data from the CFSR have been assessed against previous reanalyses in (Chelliah et al., 2011) and found to most likely represent an improved data set for synoptic studies and calculations, particularly for subtropical regions. Figure 4.1 (top panel) compares the CFSR model data to the *in-situ* observations and demonstrates close agreement over an example time period of one month. A highly significant correlation of 0.96 was found between the approximately 22 months of overlapping hourly model data and observed MSLP. Lower correlations of 0.66 and 0.65 were found between modelled and observed wind speed and direction respectively. Wind rose plots (Figure 4.2) partition the wind speed and direction into bins to demonstrate the climatological distribution of the winds. The wind rose plots of the observed data set show more easterly and southeasterly winds not captured by CFSR. The CFSR winds underestimate wind speeds compared to observations, with a scatter index (RMS error/mean value) of 0.39 (1.731/4.4). This is likely due to small-scale features not resolved by the model such as the southeasterly sea breezes or the intensities of tightly structured storm systems such as East Coast Lows (e.g. McInnes and Hubbert, 2001), which can bring strong easterly winds to the region, particularly in the winter.

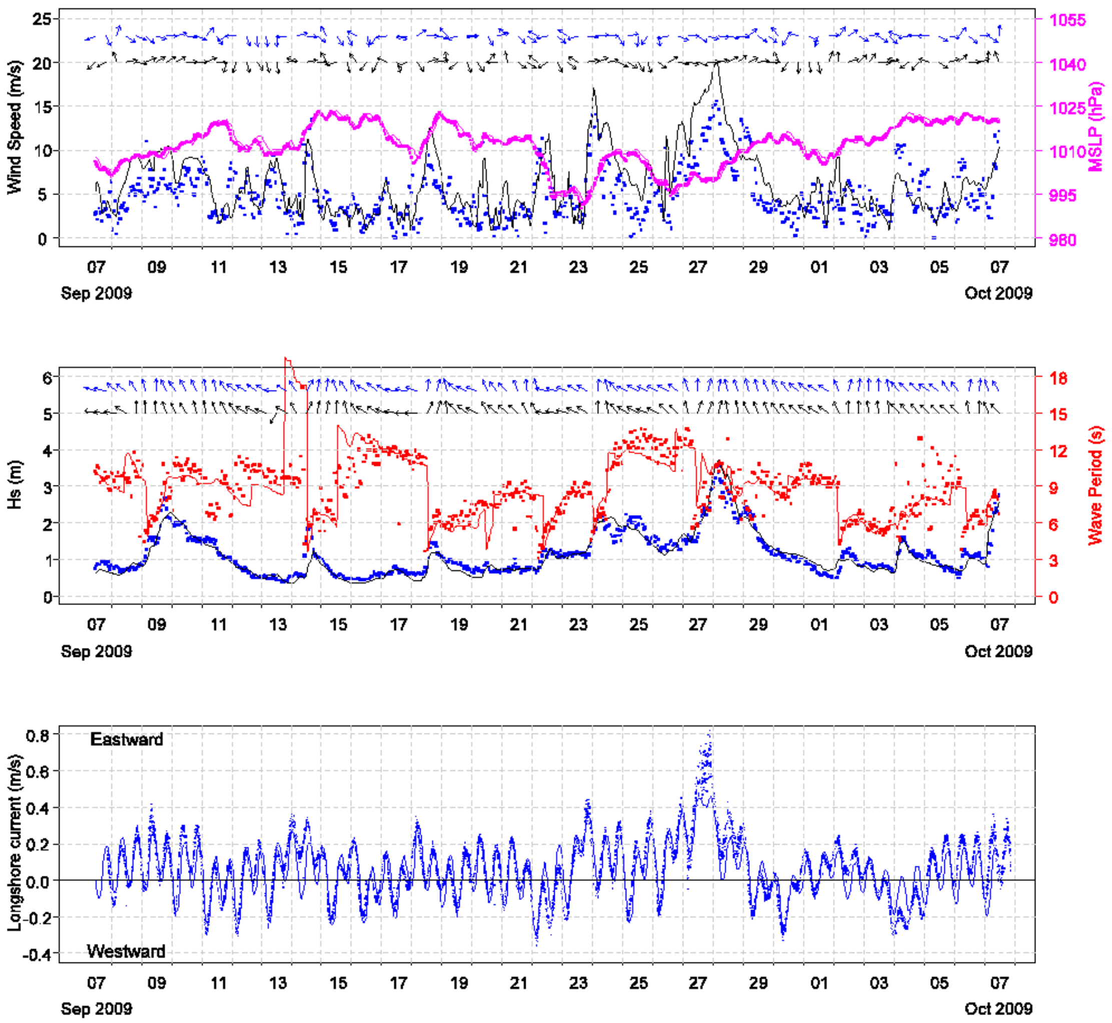


**Figure 4.1 Time series of model output validation over 31 days.**
Measurements (dots) and modelled values (solid line) are shown in all three plots. The secondary dataset corresponding to the right hand axis are MSLP (top) and wave period (middle). In the middle panel, blue arrows (above) are observations and black arrows (below) are hindcasts (reanalysis).

### 4.1.2 Waves

Significant wave height (*Hs*) is used as a general indicator of wave model performance. In the high resolution CAWCR wave hindcast (Durrant et al., 2014) there is a strong correlation (r = 0.93) between approximately 1.5 years of overlapping data with the observed waves and almost an exact regression fit with a scatter index of 0.1 (0.13/1.03). This agreement is shown in the middle plots of Figure 4.1. The lower one degree-resolution COWCLIP hindcast *Hs* correlates well (r = 0.89) with the offshore grid point in the high resolution CAWCR hindcast. However it under predicts the observed waves due to its lower spatial resolution and its availability at lower temporal resolution.

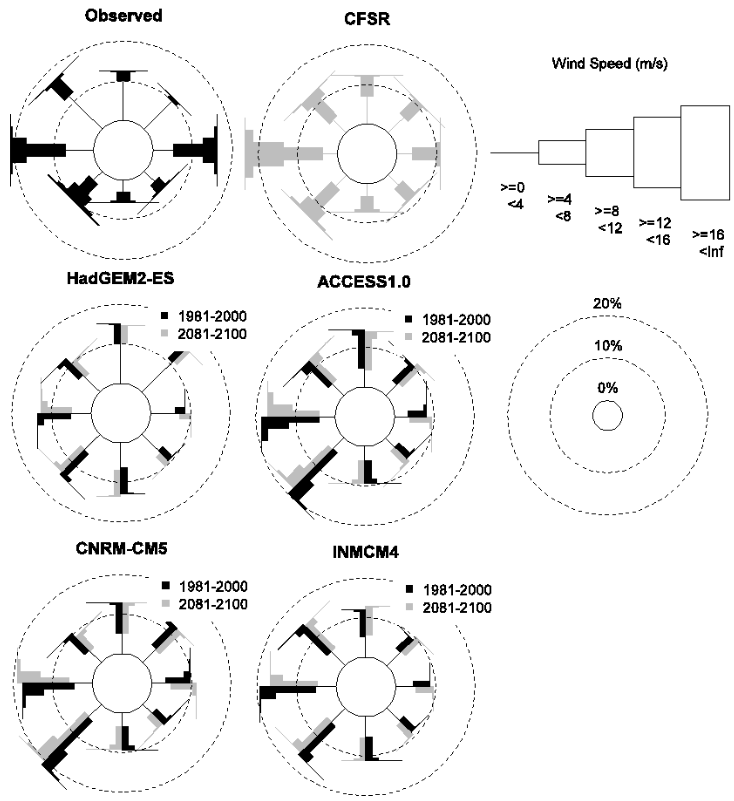


**Figure 4.2 Rose plots describing the climate of different datasets.**
The top row shows the observed and CFSR wind climate. Middle and bottom plots show the GCM baseline (black) and future (grey) wind climates.

The wide, shallow and gently sloping continental shelf in Eastern Bass Strait refracts waves so that the wave crest lines arrive almost uniformly parallel to the coast along NMB (Bird, 1978). In the gridded CAWCR hindcast dataset the wave height and direction at the model grid points located along NMB exhibit a similar signal to the hindcast grid point representing Lakes Entrance used in this study (r ≥ 0.8).

### 4.1.3 Currents

The modelled ocean currents due to meteorological and tidal forcing are plotted on the bottom panel of Figure 4.1. They validate well against the 20 months of overlapping observations (r= 0.87) with a small positive model bias of 0.07 m/s eastward, likely due to unresolved features of the model coastline. Also wave-driven currents during high wave events that are captured by the ADCP are not accounted for in the hydrodynamic model.

Three different hydrodynamic hindcast simulations were conducted to identify the effects of tides on wind-driven currents; the first simulation includes tidal and meteorological forcing (wind-tide). It simulates the total barotropic currents ($U_{t+s}$). The second simulation includes only tidal forcing ($U_t$) while the third only accounts for meteorological forcing ($U_a$). The first simulation ($U_{t+s}$) validates well against the observational dataset ($U_o$), ($r$ = 0.87) with the agreement evident in the bottom plots of Figure 4.1. The difference between the first two simulations ($U_{t+s}$ - $U_t$) is the residual surge current ($U_r$) which includes the effects of the tide on atmospheric-driven currents, which are not present for the third simulation forced by the atmosphere only ($U_a$). The residual and surge velocities ($U_r$ *and* $U_a$) are strongly correlated with each other ($r$=0.92) with a small *RMS* error of 0.03 m/s. However $U_a$ predicts faster currents than $U_r$ because it does not include tides, where for increasing tidal currents the non-linear effect limits the contribution of wind-driven currents to the total currents. This over-prediction of $U_a$ compared to $U_r$ would be important if $U_a$ was used to reconstruct a time series of total current ($U_t$ + $U_a$), however for assessing the effect of climate change, the baseline and future averaged currents are differenced so that the non-linear effect of tides on wind-driven currents can be expected to cancel out.

The model grid point used in the analysis of tides at Lake Entrance was compared to the other modelled grid points along the greater NMB coastline to investigate the spatial uniformity of the $U_a$ currents along the coastline. The correlation of hourly time series of modelled longshore currents at the Lakes Entrance grid point to other grid points along NMB reduces almost linearly with distance along the coastline away from Lakes Entrance. At around 140 km east or west the correlation is 0.75 because there is a time offset in the propagation of storm surges along the coast. Applying a 24-hour mean filter to the time series increases the spatial comparison ($r$ = ~0.8) and a three-monthly mean filter increases the spatial comparison further ($r$ > 0.9). Adding a time shift of up to three hours to the time series comparison will improve the hourly correlation ~140 km east ($r$ = ~0.9) and ~140 km west towards Corner Inlet ($r$ = ~0.8). To summarise, there are significant correlations of monthly mean values of currents along the NMB.

## 4.2 Climate Model Performance

### 4.2.1 Meteorological Fields

Visual comparison of wind roses between the CSFR climate and the four GCM climates over the same baseline period suggest that all four climate models capture the main atmospheric conditions reasonably well. However the GCM models tend to exhibit a more uniform distribution of winds across all directions, particularly at lower wind speeds. The mean monthly zonal (east-west) wind stress (Equation 3-1) from the climate models over the baseline period is compared with CFSR in Figure 4.3 and indicates that the seasonal cycle of the zonal wind stress is also captured in the GCM baseline runs. The good agreement between hindcast and GCM-forced waves and hydrodynamic fields (discussed in the next two subsections) provide further confirmation that the wind field forcing is adequately represented.

### 4.2.2 Waves

Climate projections of the longshore wave energy flux are presented to include both the wave height (proportional to wave energy) and wave direction. Several empirically based formulae exist in the engineering community to compute longshore energy flux, which can be calibrated against data from a study site to estimate sediment transport in the littoral zone. For example, the "CERC" (Komar, 1971) formula (Equation 3-32) has been used to estimate a 100,000 $m^3$/year longshore transport ($Q_w$) towards the west along NMB (GHD, 2013).

The GCM-forced wave climate projections are provided on a one-degree grid, and the grid point closest to the shore, used to represent the coastal wave climate, is assumed to be outside the littoral zone. The direction of the waves at this offshore point indicates the direction from which wave energy will come. Here only waves that originate from a direction out to sea (with a direction between 90° and 200°) were considered in the analysis.

Monthly-averaged longshore wave transport climate derived from the wave hindcasts (Equation 3-32) indicate that the mean wave energy is westward and the GCM simulations over the same time period accurately represent the direction of the transport, although they underestimate the magnitude (Figure 4.4). The hindcast shows that during austral winter months there is a shift to increased westward energy that is driven by the winter storm climate. Three of the baseline GCM simulations pick up the seasonal shift in longshore wave energy but fail to capture the magnitude of the westward energy, particularly in winter. The model forced with INMCM4 winds does not display the seasonal cycle but rather shows an evenly distributed weak westward transport.

### 4.2.3 Currents

The monthly-averaged wind-driven currents are shown in Figure 4.5. Each of the four climate simulations show the seasonal variability in the longshore coastal current in good agreement with the hindcast. The direction of monthly mean currents is also in close agreement with the monthly mean winds.

## 4.3 Climatology

In this section we present an analysis of the thirty-year reanalysis, hindcast and CMIP5 datasets to give an account of the wind, wave and wind-tide currents' climate and variability from seasonal to decadal-time scales. The relationship between local scale changes and the El Nino Southern Oscillation (ENSO) and STR-L indices are also investigated.

### 4.3.1 Winds

Wind rose diagrams of the CFSR output and observations in Figure 4.2 indicate that the dominant wind direction is from the west and southwest. The local observations include higher resolution effects such as the sea breeze and local topographic influences, which could contribute to the failure of CFSR or the GCMs to better capture the easterly component in the observed wind climate. The GCMs are also known to do a poor job of resolving the intensities of East Coast Low storm events (e.g. Katzfey and McInnes 1996) which can bring strong easterly winds to the region in the winter, hence the impact of changes to such events cannot be fully assessed from wind analysis. The GCMs tend to predict a more uniform distribution of winds with fewer strong wind events from all directions, with the ACCESS1.0 model over-predicting the distribution of northerly winds.

The monthly mean CFSR zonal wind stress (Figure 4.3) is westward throughout the year with strongest values during the winter months. This cycle is well represented by all four GCMs except the HADGEM2 model, which under-predicts the amplitude of the seasonal cycle.

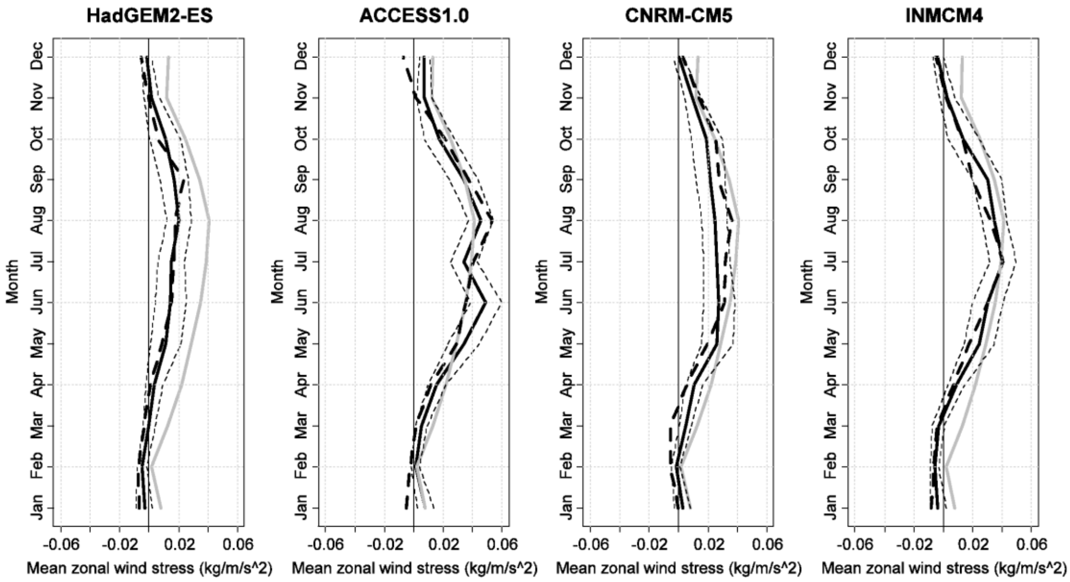


**Figure 4.3 Seasonal zonal wind stress.**

Derived from CFSR data over the 1981-2000 period (grey line), GCM baseline data, also over the 1981-2000 period (solid black line) and GCM data over the 2081-2100 period (dashed black line). Baseline internal variability is identified by plus and minus one standard deviation from the mean (thin dashed lines). Positive values indicate eastward values.

### 4.3.2 Waves

During calm wind conditions, the wave climate at Lakes Entrance is typically comprised of dominant southeasterly swell from the Southern Ocean. During the more frequent prevailing westerly wind conditions, the coastline to the west partially blocks the waves generated by westerly winds. Cold fronts can bring southwesterly winds in the winter months and are able to reverse the direction of wave energy propagation during individual storms. However the background southeasterly swell dominates the monthly climatology, leading to net westward monthly wave energy propagation, even in winter (Figure 4.4).

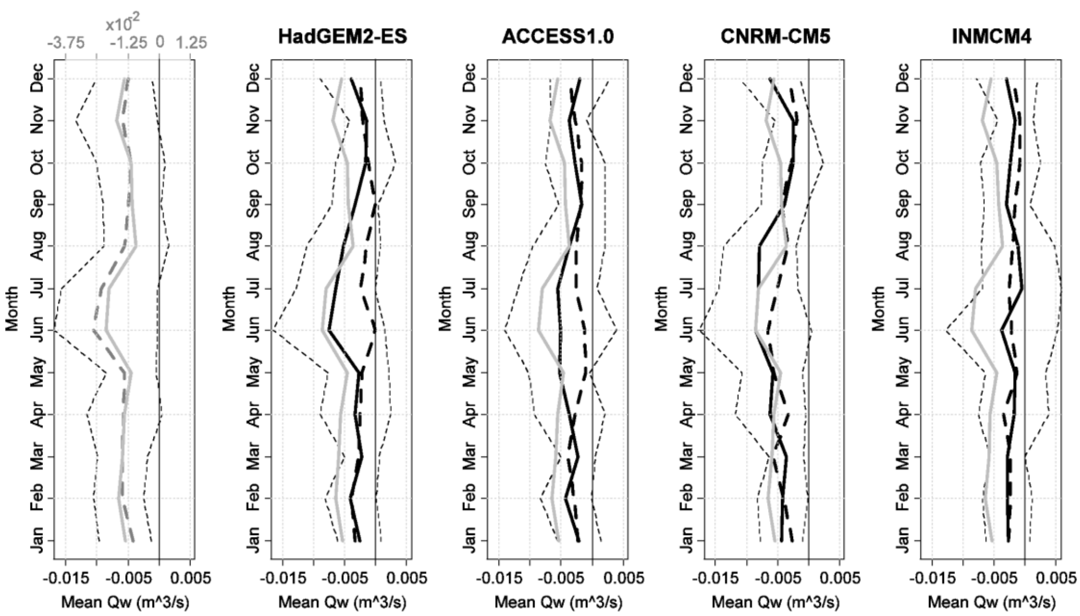


**Figure 4.4 Seasonal longshore wave transport.**

In the leftmost panel, the grey solid line is the WW3 CFSR 1° simulation with the axis at the bottom and the grey dashed line is WW3 CFSR 4 arcminute simulation with the axis at the top. The remaining panels show the WW3 CFSR 1° simulation from CFSR data over the 1981-2000 period (grey line), GCM baseline data, also over the 1981-2000 period (solid black line) and GCM data over the 2081-2100 period (dashed black line). Baseline internal variability is identified by plus and minus one standard deviation from the mean (thin dashed lines). Negative values indicate transport towards the southwest.

### 4.3.3 Currents

Table 4-1 shows the observed and modelled monthly means of the currents, tide, atmospheric forcing and wind-tide for 2009, which is the full-modelled year that overlaps with the observations. The annual mean observed wind-tide current ($U_o$) for 2009 is 0.036 m/s eastward. The strongest monthly mean current of 0.095 m/s eastwards occurs in August. February is the only month with mean westward currents of 0.037 m/s. Previous studies have shown that more frequent storm conditions arise from westerly fronts than from southerly or easterly intense lows (Tasman or East Coast Lows) (O'Grady and McInnes, 2010). These storm events occur more frequently in winter and this is reflected in the strongest monthly mean longshore current in winter forcing water eastward (Figure 4.5). Considering just the atmospheric-driven component of the currents from the hindcast simulation ($U_a$), the currents are westward to near zero during January. From October to December however the currents are less than the monthly mean eastward tidal currents, resulting in net monthly eastward currents.

**Table 4-1 Monthly mean longshore currents (m/s) for 2009 for the observed currents ($U_o$), the modelled wind-tide ($U_{t+s}$), the modelled tide currents ($U_t$), the derived residual currents ($U_r$), Atmospheric only simulation ($U_a$).**

| | $U_o$ | $U_{t+s}$ | $U_t$ | $U_r = U_{t+s}-U_t$ | $U_a$ |
|---|---|---|---|---|---|
| Jan | 0.029 | 0.019 | 0.012 | 0.007 | -0.005 |
| Feb | -0.037 | -0.013 | 0.012 | -0.025 | -0.049 |
| Mar | 0.018 | 0.014 | 0.01 | 0.004 | -0.002 |
| Apr | 0.032 | 0.022 | 0.009 | 0.012 | 0.007 |
| May | 0.038 | 0.016 | 0.009 | 0.007 | 0.01 |
| Jun | 0.042 | 0.023 | 0.011 | 0.012 | 0.02 |
| Jul | 0.08 | 0.06 | 0.012 | 0.048 | 0.078 |
| Aug | 0.095 | 0.073 | 0.012 | 0.061 | 0.088 |
| Sep | 0.066 | 0.052 | 0.01 | 0.042 | 0.066 |
| Oct | 0.018 | 0.006 | 0.008 | -0.002 | -0.01 |
| Nov | 0.013 | 0.01 | 0.01 | 0.001 | -0.01 |
| Dec | 0.016 | 0.016 | 0.011 | 0.005 | -0.004 |
| Ann | 0.036 | 0.025 | 0.011 | 0.015 | 0.016 |
| | | | | | |

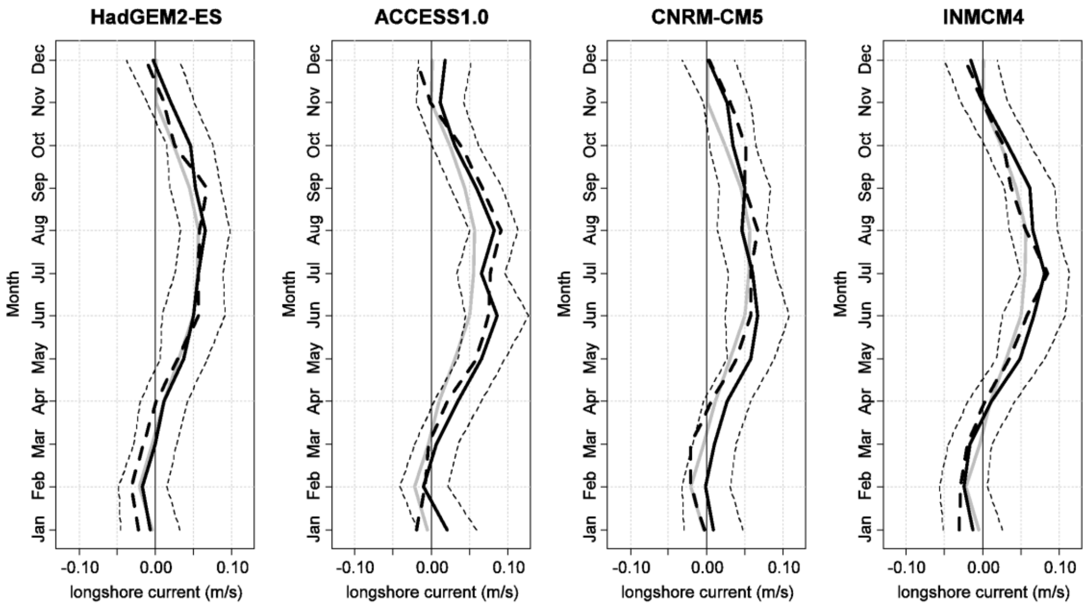


**Figure 4.5 Seasonal longshore wind-driven currents.**

$U_a$ derived from CFSR data over the 1981-2000 period (grey line), GCM baseline data, also over the 1981-2000 period (solid black line) and GCM data over the 2081-2100 period (dashed black line). Baseline internal variability is identified by plus and minus one standard deviation from the mean (thin dashed lines). Positive values are eastward.

### 4.3.4 Subtropical Ridge Location

The monthly mean STR-L identified in CFSR is located at around 39°S in the summer months and 31°S in winter (Figure 4.6). It is positively correlated (r=0.72) with the CFSR zonal wind speed over Lakes Entrance. The mean timing and direction of the latitudinal shift of the STR is replicated well in all except the INMCM4 baseline simulations. The INMCM4 model simulates an earlier transition of the STR to its northern wintertime position than CFSR. During winter months the mean STR-L in HadGEM2-ES is too far north, while the position is further south for CNRM-CM5 and INMCM4. In summer months the HadGEM2-ES and ACCESS1.0 models place the STR-L around one degree south of CFSR such that it is in the middle of eastern Bass Strait. This could explain the westward bias in the zonal winds for the baseline simulations at the study location (Figure 4.3).

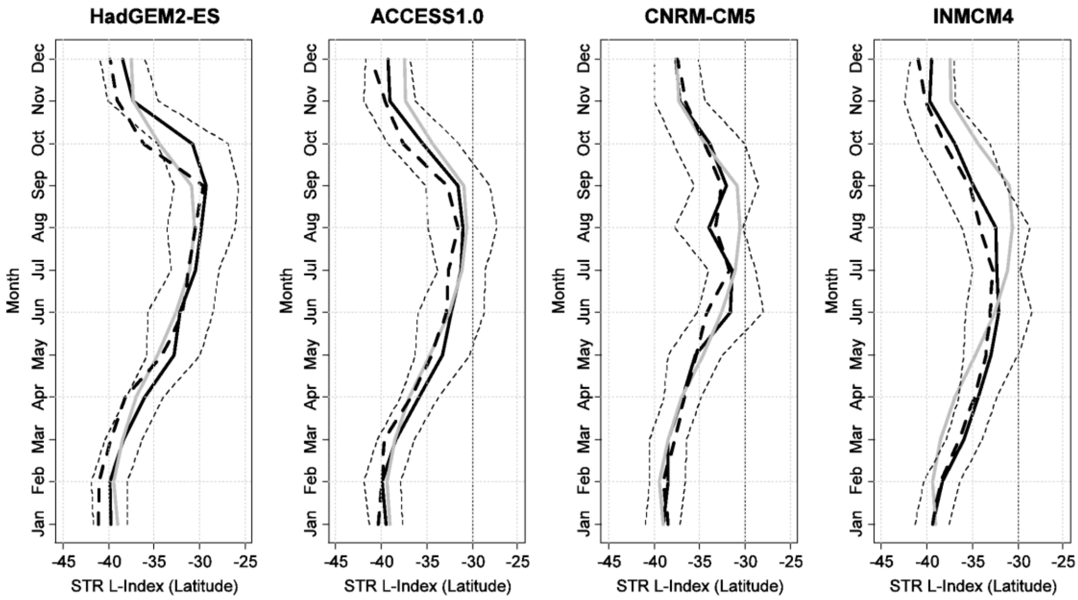


**Figure 4.6 Seasonal Subtropical Ridge location (STR-L).**

Derived from CFSR data over the 1981-2000 period (grey line), GCM baseline data, also over the 1981-2000 period (solid black line) and GCM data over the 2081-2100 period (dashed black line). Baseline internal variability is identified by plus and minus one standard deviation from the mean (thin dashed lines).

### 4.3.5 Variability and Relationship to the SOI

Normalised monthly means for the 1981-2000 period were calculated by removing the total mean (*H*) from the monthly mean values (*M*) and dividing by the standard deviation of the hindcast, (i.e., *(M-H)/sd(M-H)*). The monthly variability of longshore wind stress, currents and STR-L are similar over the period of the thirty-year hindcast and this agreement is quantified by the correlation coefficients shown in Table 4-2. The STR-L values are positively correlated to wind (0.72) and currents (0.75) and there is a strong correlation between wind stress and currents (0.93). However, the correlation coefficients between STR-L and waves (0.18) and wind and waves (0.26) are small indicating that although they are significant, a large amount of the variance of the wave fields is not explained by the variability of winds and STR-L index calculated between 145-150°E. The smaller correlation to waves is likely due to the fact that a large amount of wave variability is remotely generated and related to swell originating in the Southern Ocean.

**Table 4-2 Annual cross-correlation r statistics for the normalised longshore monthly mean and monthly anomaly: wind, waves, wind-driven currents, STR-L and SOI.**

| Normalised monthly correlations | | | | | |
|---|---|---|---|---|---|
| | | Wind | Wave | Currents | STR-L |
| Wind | | 1 | 0.26 | 0.93 | 0.72 |
| Wave | | 0.26 | 1 | 0.19 | 0.18 |
| Currents | | 0.93 | 0.19 | 1 | 0.75 |
| STR-L | | 0.72 | 0.18 | 0.75 | 1 |
| Normalised monthly anomaly Correlations | | | | | |
| | SOI | Wind | Wave | Currents | STR-L |
| SOI | 1 | -0.12 | -0.12 | -0.12 | -0.17 |
| Wind | -0.12 | 1 | 0.43 | 0.87 | 0.62 |
| Wave | -0.12 | 0.43 | 1 | 0.4 | 0.27 |
| Currents | -0.12 | 0.87 | 0.4 | 1 | 0.62 |
| STR-L | -0.17 | 0.62 | 0.27 | 0.62 | 1 |

The monthly seasonal cycle was removed and normalised to allow for a comparison of the monthly anomalous longshore transport variables and STR-L to the SOI. The anomalies are calculated by removing the hindcast average (longshore wind, wave or current) value for a given month (*Hm*), from that monthly average (*M*) and dividing by the standard deviation of the hindcast anomalies (i.e. *(M-Hm)/sd(M-Hm))*. Table 4-2 displays the correlation values. The monthly anomalies of STR-L are strongly correlated to wind stress anomalies (0.62) and to current anomalies (0.87). The correlation between anomalous wind and current is also strong (0.87). This indicates that anomalous southward (northward) movements of the subtropical ridge results in anomalous westward (eastward) longshore coastal transport. Interestingly the correlation values between anomalous STR-L and waves (0.27) and anomalous wind and waves (0.43) are larger than those related to the normalised monthly means indicating that local atmospheric anomalies are affecting the wave field to some extent. Figure 4.7 shows the time series over 1981-2000 of the discussed variables. The time series in this plot are smoothed with a 12-month running mean for visual clarity. This 12-month filtered plot shows that the year-to-year variations in the STR-L, wind stress and currents are quite similar, confirming the results of the correlation analyses discussed above. The time series related to the wave height generally agrees well with the STR-L. Exceptions exist for some years (e.g. 2002) where the wave anomaly is opposite to the other transport anomalies. As discussed above this may indicate the remotely forced nature of the local wave field.

Correlation values between the transport variables and the SOI have been found to be small in general suggesting a weak relationship on a month-to-month basis (Table 4-2). However, the filtered plot (Figure 4.7) does suggest that at times a relationship between certain ENSO events and transport anomalies may exist. For example the strong El Nino years 1983 and 1997 are also related to enhanced eastward- anomaly in the wave field, wind stress and STR-L. In general Figure 4.7 suggest that that over prolonged periods of negative (positive) SOI transport anomalies tend to be eastward (westward). Although we identify a possible relationship here a more detailed analysis is necessary to comment on a possible forcing mechanism related to ENSO.

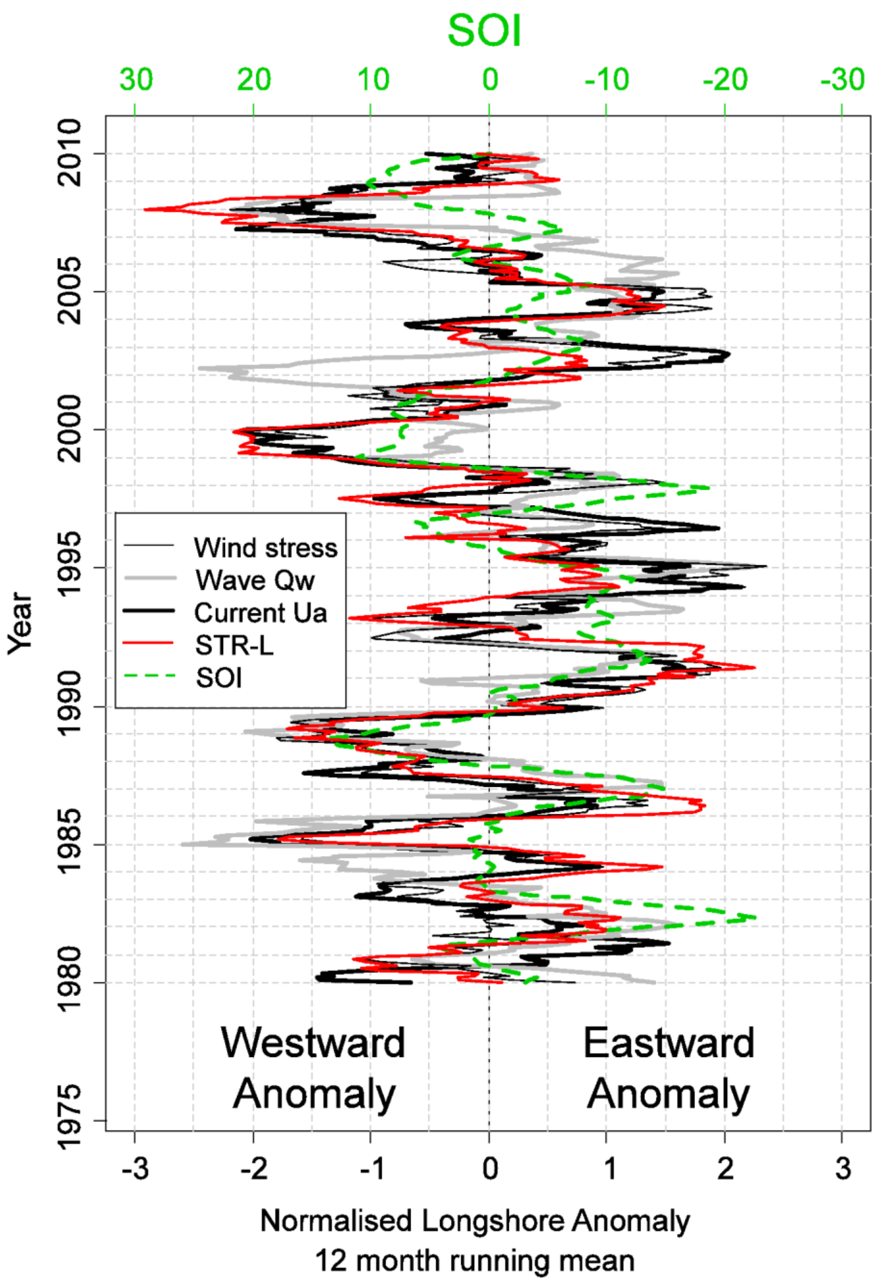


**Figure 4.7 Hindcast longshore normalised annual residual.**

Hindcast datasets of the longshore normalised annual residual, the difference between the annual mean value and the hindcast mean value relative to the hindcast mean. A 12-month moving average filter has been applied to the monthly anomalies values. Top axis corresponds to the SOI value with positive direction reversed to line up with residual direction. Positive (negative) SOI corresponds with westward (eastward) transport anomalies. The positive (negative) normalised STR-L index (thin red line) values are northward (southward) anomaly from the monthly mean location.

## 4.4 Climate Change

Normalised values are presented to indicate the climate change signal relative to the model's internal variability for ensemble model comparison, where the internal variability is described as one standard deviation of the model time series (section 3.3). Values are normalised to lessen any bias within the model that arises from that model's change signal.

### 4.4.1 Winds

Wind rose plots (Figure 4.2) show that the annual directional distribution of future winds shift to more easterly conditions and this change is also captured in the seasonal cycle of the zonal wind stress (Figure 4.3). The future mean seasonal cycle mostly sits within the internal variability (one standard deviation) of the baseline. Figure 4.8a indicates that for future climates all four GCMs show a shift towards enhanced westward zonal mean wind stress in summer and spring months by a factor of 0.1 to 0.5 compared to the internal variability of the baseline, i.e. 10 to 50% of one standard deviation higher. Some models predict enhanced eastward wind stress in winter thereby indicating a possible increase in the amplitude of the seasonal wind cycle.

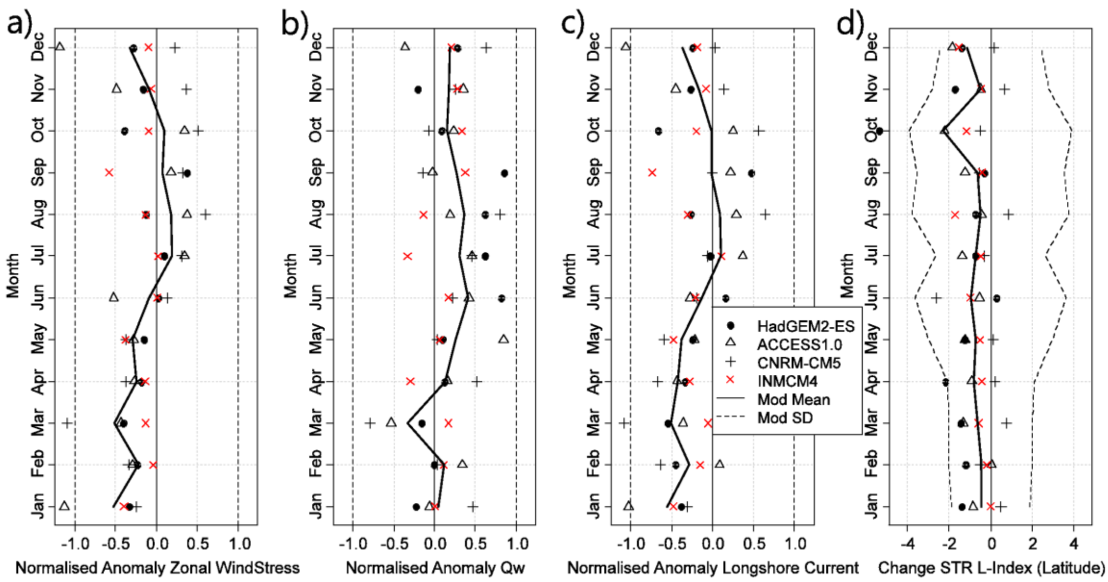


**Figure 4.8 Monthly mean climate change normalised model anomaly from annual baseline mean.**

a) Wind stress, b) wave transport ($Q_w$), c) wind-driven current and d) the change in STR-L in degrees latitude. Black line is the ensemble model monthly mean value. Baseline internal variability is identified by plus and minus one standard deviation from the mean (thin dashed lines).

### 4.4.2 Waves

Baseline and future seasonal statistics are shown in Figure 4.4. They indicate weakening of south-westward wave transport in all four GCM model runs, particularly during winter months. Figure 4.8b indicates possible enhanced westward wave transport in summer and early spring in the ACCESS1.0 and HADGEM2-ES models, noting that some differences may be expected because of the influence of remote swell. These seasonal changes are broadly consistent with changes in the local wind stress and will amount to a reduction in the amplitude of the seasonal cycle of wave transport cycle in the future relative to the baseline GCM runs.

### 4.4.3 Wind-driven Currents

For most of the year, each of the four climate simulations agree on a decrease in the mean eastward longshore coastal currents (Figure 4.7) consistent with a general decrease in the mean eastward wind stress (Figure 4.3). During summer when the baseline mean currents are close to zero or slightly negative, the models all indicate enhanced westward flow in the future climate by a factor of around 0.45 compared to the internal variability of the baseline, i.e. 45% of one standard deviation higher (Figure 4.8c). In autumn where the baseline mean currents are close to zero or slightly positive eastward (Figure 4.5) the models all indicate a slight westward change to zero or slightly negative westward currents indicating a switch to greater westward flow. In winter and spring the strong positive baseline eastward current is suggested to remain the same or slightly increase for some models. The seasonal change of the longshore wind-driven currents amount to an increase in the amplitude of the seasonal cycle, with more westward currents in summer months and slightly more eastward currents in winter months.

### 4.4.4 Subtropical Ridge Location

On average all four models predict an annual southward shift of approximately 0.59° in the location of the STR (Figure 4.8d). For most months of the year the method for identifying the STR-L predicts a constant southward shift, however in October the transitional MSLP fields from the Northern Australian dry to wet season make it difficult to identify the correct STR-L location, particularly for the HadGEM2-ES model and this results in a large range in the ensemble change (Figure 9d).

## 4.5 Discussion

Relating the changes of wind, waves and currents to the changes in STR-L, is more relevant in summer when the STR-L is situated over the study area. In winter the STR is located 10-degrees north of the study location so the connection of the changes in STR-L to transport is reduced. Hence it is suggested that the change in STR-L will directly impact the transport from winds and currents during summer months, which is a change in the mean climate on the order of 45% of the baseline internal variability (Figure 4.8). However, subsequent model experiments in Chapter 7 shows that the net transport change is indeed driven by transport in winter months, indicating the reduced importance of the STR-L as an indicator of net transport change. Changes to wave transport, including swell, in the winter months are likely due to the contraction and increased intensity of the westerly storm belt linked to SAM (Hemer et al., 2009). However, we note that examination of the role of SAM on a finer scale in several localised regional studies have found that the connection of the trend in SAM to observed changes can be complex, differing in direction (sign) from one season to the next (Christensen et al., 2013).

Despite wind and wind-driven currents being of opposite sign to the wave-driven transport, the seasonal changes associated with climate change for the three variables display a similar pattern. This consists of a shift to enhanced transport westward in summer and a little change to slight increase eastward in winter, reducing the amplitude of the seasonal cycle of waves and increasing the amplitude of the cycle of both wind and wind-driven currents (Figure 4.8). The summer changes will therefore enhance the net westward transport during these months. The changes in winter will slightly increase the mean eastward wind and wind-driven currents and decrease the opposing westward wave transport.

Depending on the relative contribution of wave transport and wind-driven currents to the total net sediment transport across the littoral zone, the reduction in westward wave transport during winter could mean net transport could switch to an eastward regime driven by the currents. However the projection of increased westward transport during summer for both waves and wind-driven currents could return the annual net budget to a more balanced state. Numerical process modelling studies are presented in subsequent chapters to quantify the contribution of waves and currents to net transport across the littoral zone from these large coastal scale changes. But before this, measured morphological datasets are presented in the next chapter, as validation for the numerical modelling.

# 5. OBSERVED MORPHOLOGY AND MORPHODYNAMICS ANALYSIS

In this chapter the changes in bathymetric surveys are analysed to quantify the morphodynamics. *Bed evolution* and *volume transport* are the two key morphodynamic variables investigated in this chapter. These two variables are also investigated in the following two chapters on modelling sediment transport. The two variables are related in that the volume transport flux into and out of a sediment cell (from erosion and accretion) results in the bed evolution. The first variable, bed evolution, is simply measured as the change in vertical height of the bottom, in units of metres (m), between surveys at each grid point.

The second variable, volume of transport, takes on different forms. It can be presented as a point source (denoted by a lowercase $q$) or integrated across a cross-shore profile (denoted by an uppercase $Q$) and can be presented as a rate or integrated over time interval $\delta$ (denoted by $q\delta$ or $Q\delta$). The explanation of the sediment transport terms used in this study are:

1) *Sediment transport rate* $q$ is a scalar value and represents the volume transport per bed width in the direction of the transport, per second ($m^3m^{-1}s^{-1}$) or per year ($m^3m^{-1}yr^{-1}$). E.g. TELEMAC transport rate $q_T$ (Equation 3-18) and the bedform tracking transport rate $q_v$ (Equation 3-4).
2) *Net sediment transport* $q\delta$ ($m^3m^{-1}$) is the cumulative sum of the sediment transport rate $q$ ($m^3s^{-1}$) over time $\delta$ (survey or model period) multiplied by the sample time-step and is positive eastward and negative westward.
3) *Longshore sediment transport rate* $Q$ is the cross-shore integrated sediment transport rate ($q$). It is a scalar value and represents the volume transported in the longshore direction,

per second ($m^3s^{-1}$) or per year ($m^3yr^{-1}$), which is positive eastward and negative westward. E.g. The CERC $Q_w$ (Equation 3-32), the bedform identified transport integrated between depth contours $Q_v$ and the TELEMAC cross-shore intergraded value $Q_T$. The latter is calculated as the sum of the longshore component of the sediment transport rate $q_{T,,L}$ ($m^3m^{-1}s^{-1}$) at all wet grid points in the model domain, at each time-step, multiplied by the typical cross-shore grid-point width (40 m), and then divided (averaged) by the number of cells in the longshore direction (165).

4) *Net longshore sediment transport* $Q\delta$ ($m^3$) is the cumulative sum of the longshore sediment transport rate $Q$ ($m^3s^{-1}$) over time $\delta$ (survey or model period) multiplied by the sample time-step and is positive eastward and negative westward.
5) *Gross longshore sediment transport* ($m^3$), is not presented in this study, but is calculated as the cumulative sum of the absolute value of longshore transport rate (positive both eastward and westward) multiplied by the output time step.

Analysis of the single-beam survey profiles provides a measure of the bed evolution. Analysis of the multibeam surveys (which capture the bedform movement) provides a measure of longshore transport. Both analysed datasets will be used to validate the model in the next chapter. The spatial and temporal variability of the coastline is also analysed to investigate the extent of variability of profiles along NMB.

## 5.1 Spatial Morphodynamic Variability

LiDAR profiles for the entire NMB indicate the shape of the nearshore profile. These profiles exhibit, on average, a more recognisable storm-bar and trough profile approximately 100-300m offshore towards the eastern end of NMB (Figure 5.1). Note that the LiDAR survey was conducted over a few months of calm weather conditions between November 2008 and April 2009. The storm-trough is graphically represented in the 3.5m and 5m depth contour lines of the CNPG map (Figure 5.2). The encircled 3.5m contour line between McGauran’s Beach and Golden Beach in Figure 5.2 indicates the shallow trough profile (deeper than 3.5 m), as plotted for North Seaspray in Figure 5.1. The encircled 5m depth contours to the east of Ewings Marsh Pettman Road in Figure 5.2 show the deep trough profile (deeper than 5 m), as plotted for Ewings Marsh Beach Road in Figure 5.1. West of McGauran’s Beach the 3.5 m depth contour does not indicate the presence of a storm-trough.

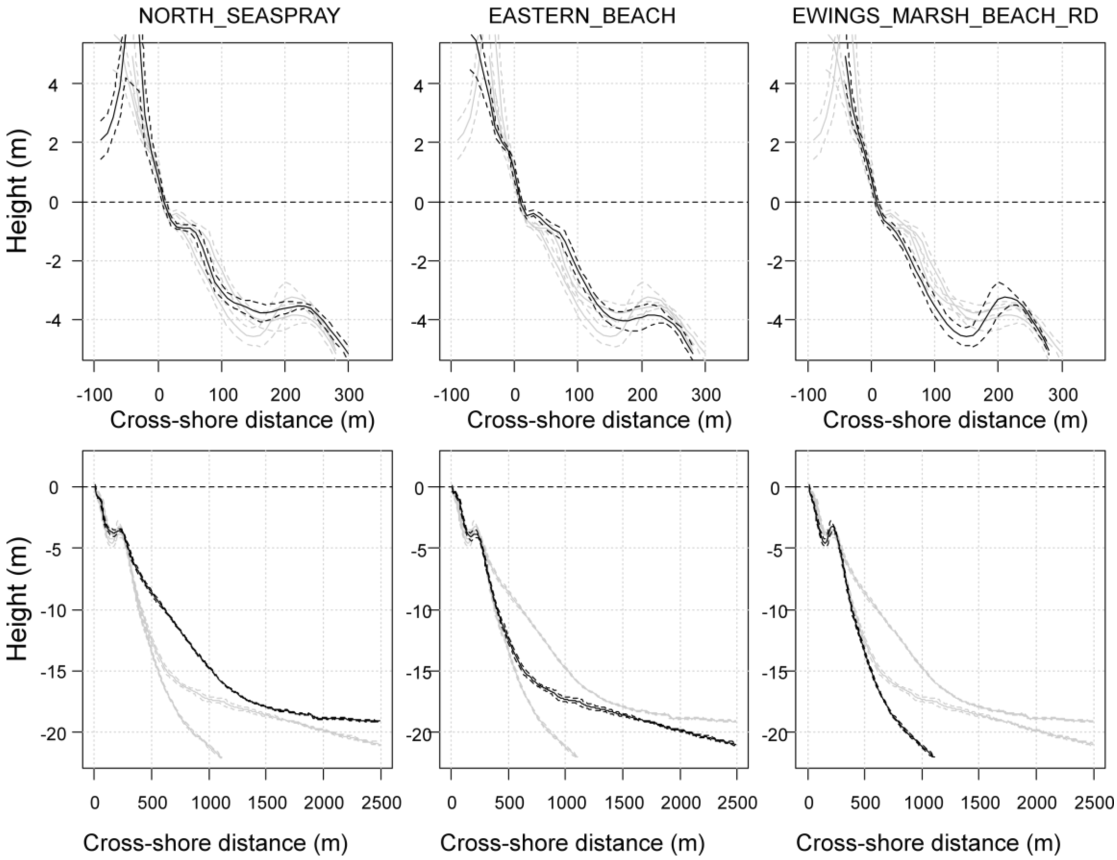


**Figure 5.1 Profile view of select NMB cross-shore profile from LiDAR dataset.** North Seaspray (left column), Eastern Beach (middle) and Ewings Marsh Beach road (right) sites are listed from east to west of NMB respectively. The black solid lines are the mean profile calculated from the adjacent 1km of coastline at each site. The dashed lines represent +- one standard deviation. Greyed-out lines are the other two site profiles. The top row is the inner profile (0-300m off the coast) and the bottom row is the entire nearshore profile (0-2.5 km). See Figure 3.1 for locations.

The location of the 2m and 5m depth contours are around 100m and 300m from the shoreline respectively, for the entire NMB coastline, indicating a reasonably uniform shore-terrace zone (which covers the possible location of storm-bar and trough) along NMB (Figure 5.2). At greater depths, Figure 5.2 shows the 12m, 15m, 20m contours are closer to the coastline at the eastern end and further away to the western end of NMB, as shown for the steepening profiles towards the eastern end of NMB in Figure 5.1.

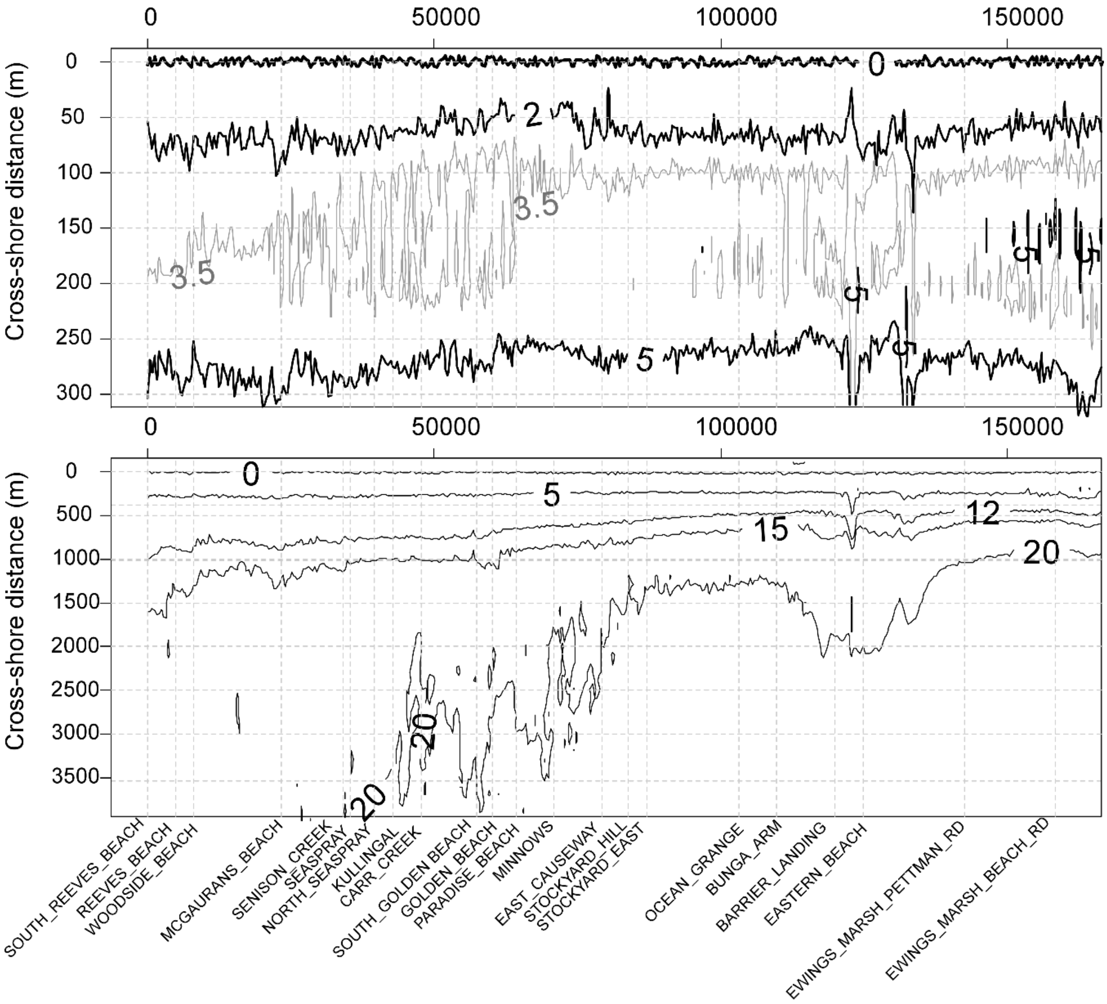


**Figure 5.2 Curvature-corrected coastline map view of NMB depth contours from the LiDAR coastline normal profile grid (CNPG).**

The top plot focuses on the inner 0-300m off the coastline and the bottom plot on the entire nearshore region (0-4km off the coast). The top horizontal axis is the longshore distance (m) from west to east and the vertical axis is offshore distance from the coastline. See Section 3.1.4.1 for a description of the CPNG.

The spatial variability of the first key morphodynamic variable analysed in this study, bed evolution, is quantified by the mean bathymetric height within the typical location of the storm-trough (100-200m off the coast) and storm-bar (200-300m off the coast) (Figure 5.3). The mean height of both the trough and bar zones decrease from Reeves Beach to East Causeway and then level off towards the Ocean Grange. On the eastern side of 'The Bar' there are larger variations in the height of the two zones. On average, the height of the storm-bar zone increases and the height of the trough zone decreases (deepening trough) east of The Bar. The difference between the height in the two zones (outer less inner), shows the seabed within the storm-bar zone is on average one meter deeper west of Ocean Grange, representing the small bar formation observed in the profile. The difference between the heights in the two zones also shows the bar zone can be up to 2m deeper around The Bar, where there is variable bar formation. East of 'The Bar' the storm-bar height increases to a similar height as the trough towards Ewings Marsh Beach road, where a deep storm-bar and trough formation is also observed (Figure 5.1).

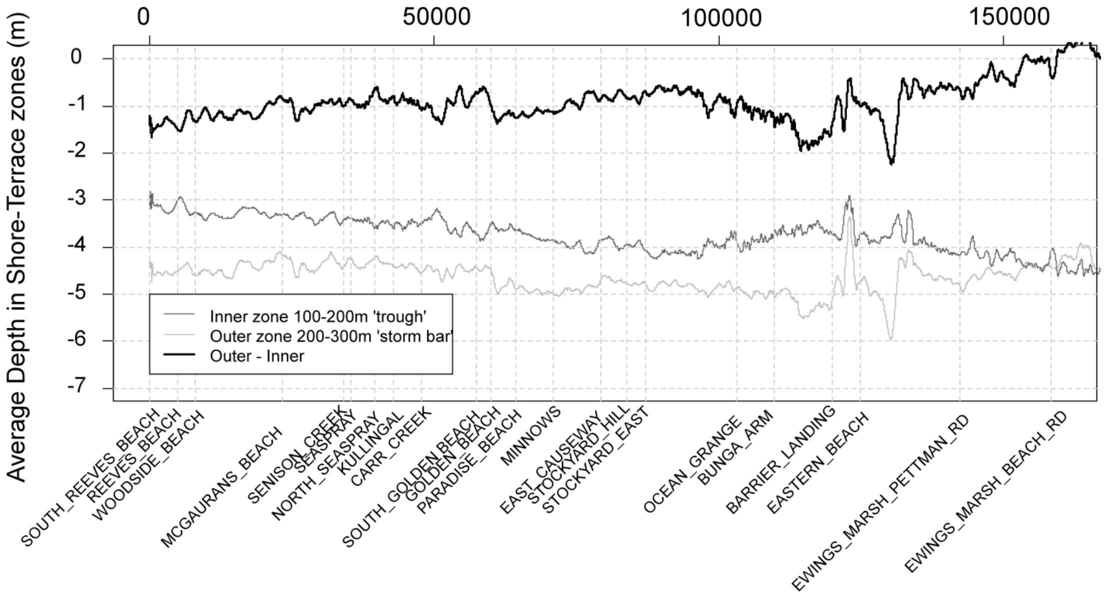


**Figure 5.3. Spatial variation in the nearshore bed elevation.**

Average bed elevation of the inner (outer) zone, 100-200 (200-300) metres from the coast representing the location of the storm-trough (-bar). See Figure 5.1 for example profile plots.

## 5.2 Temporal Morphodynamic Variability

### 5.2.1 Nearshore Bed Evolution Changes

Eight single-beam surveys at both sites show the absence of a storm-bar and trough between June 2009 and February 2011. These are followed by the presence of a storm bar in the final two surveys between September 2011 and March 2012 (Figure 3.2). The area-average height of the single-beam profiles in the storm-bar and storm-trough zones quantify these bed evolution changes (Figure 5.4). The difference between the depths in the two zones (outer less inner) over the first eight surveys, indicated on average, the seabed in the location of the storm-bar is 3 m deeper for the first eight surveys (Figure 5.4), i.e. the-storm bar is absent (see Figure 3.2). This difference is much larger than the spatial variability observed for the LiDAR survey of the entire NMB coast (Figure 5.3). The difference between the depths in the two zones returns to a value closer to the LiDAR survey in the later part of 2011, where the average depth in the bar zone is one metre deeper than the trough zone. This indicates the return of the distinctive storm-bar and trough (Figure 3.2). Both sites exhibit similar patterns of variability, even though there was dredge material disposal at the west site during the survey period which could have interfered with the elevations (GHD, 2013).

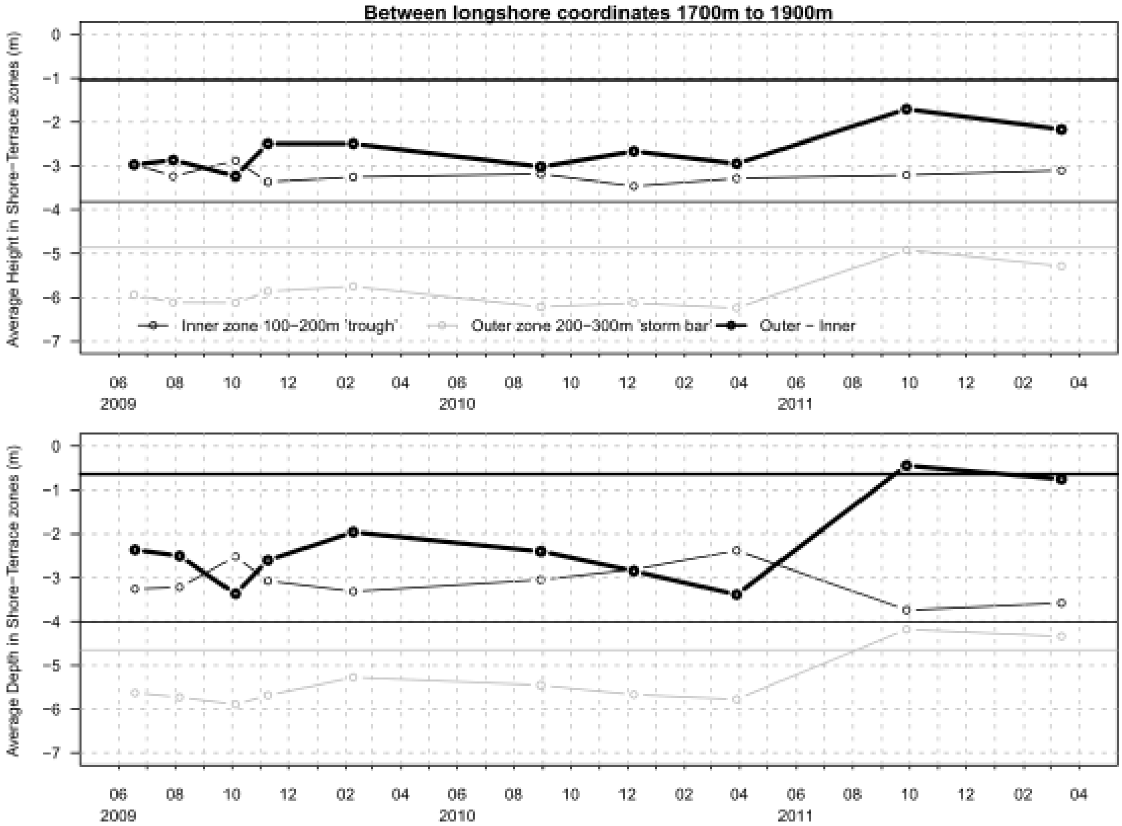


**Figure 5.4 Temporal variation in the single-beam nearshore mean bed elevation.**

The top (bottom) plot shows the west (east) site temporal variation in the single-beam storm-bar and trough zone mean depths. LiDAR values indicated by straight horizontal lines extracted from the approximate location of Barrier Landing (Eastern Beach) for the west (east) site (Figure 5.3). Line styles correspond to single-beam value in the legend. Inner (outer) zone represents the location of the storm-trough (-bar). Profiles of each survey are plotted in Figure 3.2.

### 5.2.2 Longshore Bedform Migration

At both multi-beam survey sites, submarine dunes are visible 400-900 m off the coast, between the 11-16 m depth contours (Figure 3.5). The dunes have a wavelength between 20-40 m and a height between 0.3-0.5 m. On average the dunes are 0.10 m smaller in 11 m depth of water than in 15 m. The asymmetry is on average positive, stoss-side (the bedform side facing the flow) to the east, as evident in Figure 3.6. The crest lines of the dunes are normal to the coastline indicating they move in the longshore storm-tide flow direction. Dunes are sometimes grouped on the seaward side of larger sandwaves. The sandwaves have a wavelength on the order of hundreds of meters and height of meters tall and are located within the 12-16m-depth contours. In shallower depths, closer to the coastline, the influence of surface waves appear to wash out the dune. Further analysis of the larger LiDAR survey shows that dunes and sandwaves exist at different sections of the entire NMB coastline.

The identification and tracking of the dunes is detailed in Section 3.5. Figure 5.5 and Figure 5.6 show plots of the submarine-bedform-crest shift-in-location against depth, between the five multi-beam surveys. Also plotted are the mean and standard deviation of the crest population statistics (from 1 m depth bins). The method for identifying the crest shows some scatter (quantified by the dashed standard deviation curves) due to the somewhat regular bedform shape, and the interpolation of the 2.5 m gridded data with spline curves. Surprisingly, the mean location of the dune crests do not appear to move between the first two surveys over winter of 2012 (Figure 5.5, Figure 5.6). In the subsequent surveys the bedforms move, on average, 1 m east per survey over spring and summer. The final change survey shows an interesting pattern, where in water depths between 11-12m, the transport is reduced to near zero. This could suggest that the depth threshold at which the westward wave-driven currents begin to strongly influence the eastward flowing wind-tide generated currents was located at approximately the 12 m contour between the last two surveys. The asymmetry of the bedforms was also calculated to show that they were on average heading to the east for all depths (Figure 3.6).

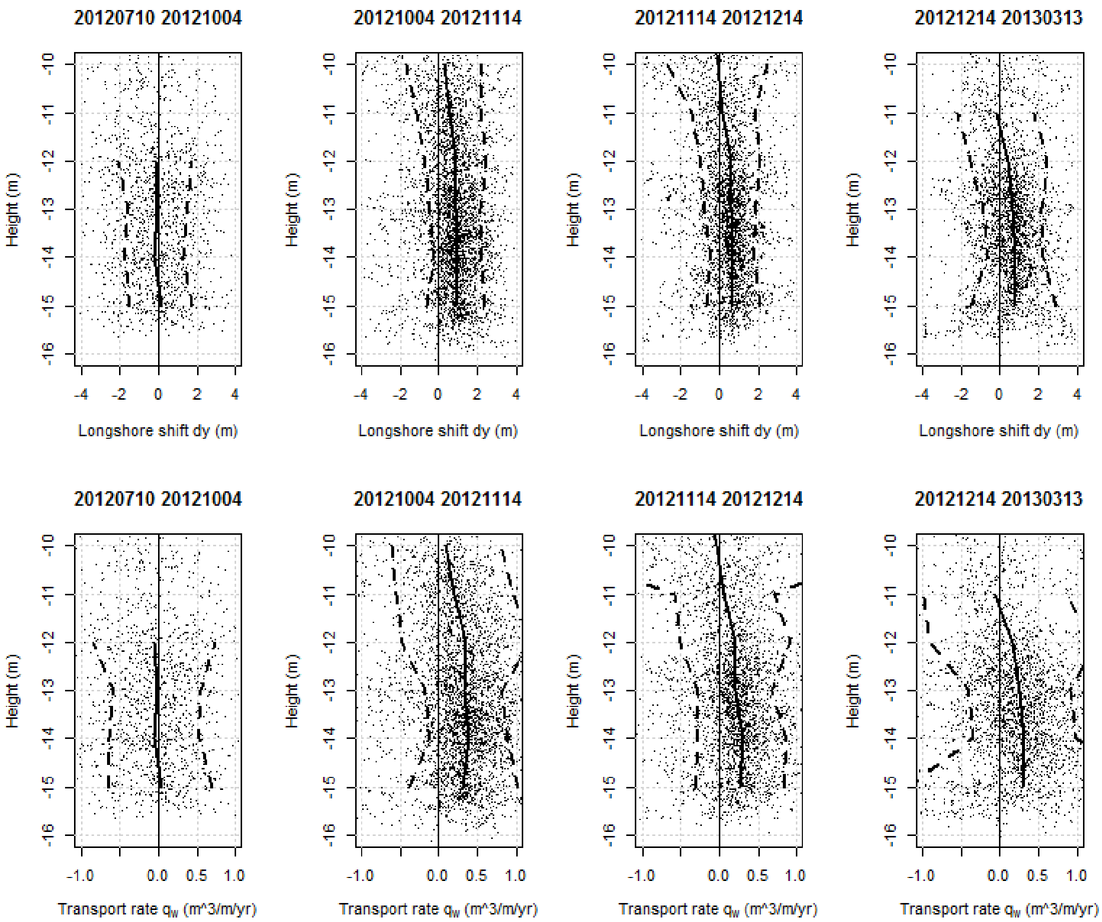


**Figure 5.5 Bedform identified sediment transport rate $q_w$ (m$^3$/m/yr) at the west survey site.**

The top row displays dune-crest position-shift in the longshore y-(eastwards) direction (dy) at the west site, between successive transects. The bottom row shows the corresponding sediment transport rate (m$^3$m$^{-1}$y$^{-1}$) estimates in the longshore direction (Equation 3-4). The dots indicate individual dune-crests. The back solid line is the average value within 1 m depth bins and the dashed lines are ± one standard deviation population intervals.

The sediment transport averaged across the 12 and 15 m depth contours at each survey site is plotted in Figure 5.7. Both the east and west sites display consistent direction of transport. The west site predicts more transport than the east site. This difference could be a result of the dredge material or the interaction of the large ebb-tide-delta separating the sites interfering with the longshore flow.

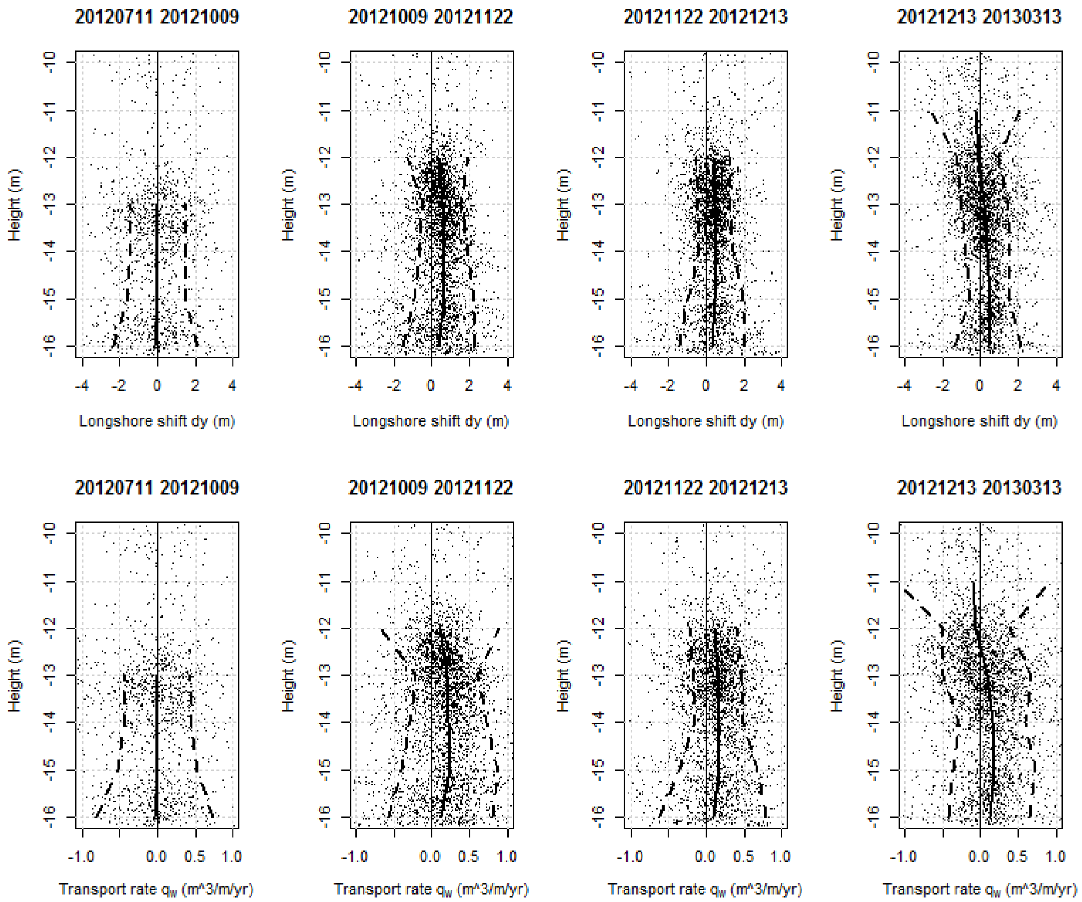


**Figure 5.6 Bedform identified sediment transport rate $q_w$ (m$^3$/m/yr) at the east survey site.**

Same as Figure 5.5 but for the east survey site.

The net longshore transport per unit bedform crest width over the eight months ($q_v\delta$) is around 0.5-1.0 m$^3$m$^{-1}$ to the east (Figure 5.7). The cross-shore distance the bedform crests extend (between the 12-15 m depth contours) is around 200 m. Therefore over the eight months, the intergraded longshore sediment transport ($Q_v\delta$) is100-200 m$^3$ eastward between the 12-15 m depth contours in the direction of the surge-tide flow identified by bedform movements.

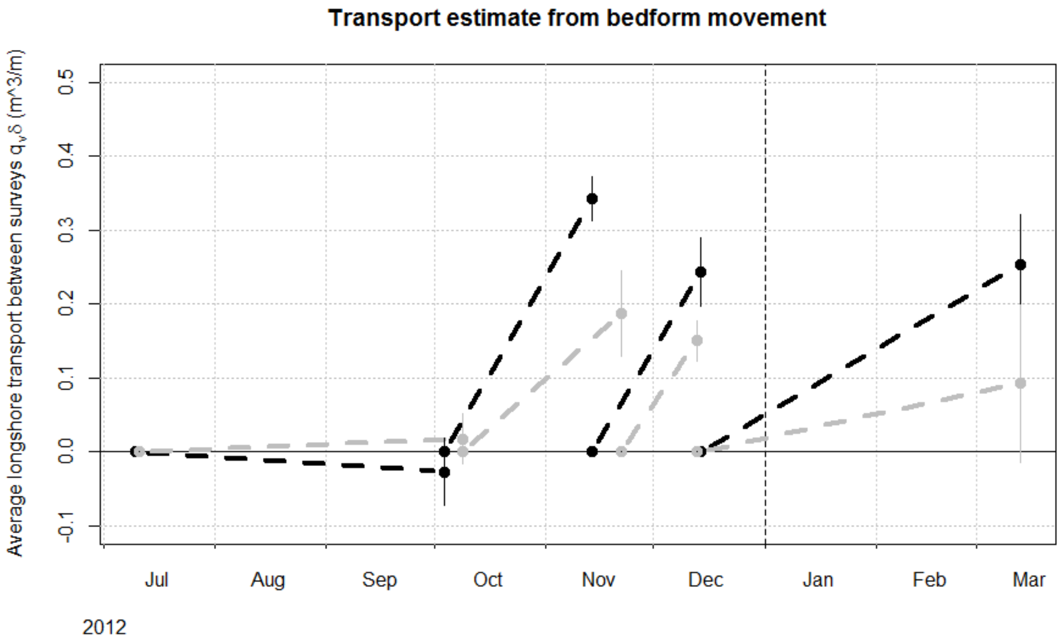


**Figure 5.7 Longshore transport estimate from bedform movement m$^3$/m.** Positive (negative) values on the vertical axis are transport in eastward (westward) direction. The dashed lines show the simple linear approximation of the volume per unit crest width (m$^3$/m) of transport over each survey period. The transport is estimated for all bedforms binned, between 12-15 m depth contours. The whiskers indicate ± one standard deviation of different binned depths estimates.

## 5.3 Discussion

The changes in the storm-bar and trough are used to quantify bed evolution over the survey period. Landward of the storm-bar and trough, 0-100 m seawards of the shoreline in 0-2 m depth of water, where everyday waves break, smaller longshore bars (metres wide) and troughs are very mobile (Wright et al., 1982). This is especially the case when one considers the variability of rip channel morphology changing in location from hour to hour (Dalrymple et al., 2011). At the multi-month sampling frequency, it is uncertain if the storm-bar and trough has formed and washed away multiple times with passing storms and periods of recovery between each survey.

Analysis of extreme wave climate can provide some indication of when the storm-bar and trough could change. Given the simple understanding that waves will break on average when waves reach a height of around 0.8 of the water depth (Holthuijsen, 2007). The significant wave height (~top 1/3 of wave heights) that will break on the top of the storm bar (h = 4.5 m) will need to be around 3.6 m. So, it can be assumed that any event with significant wave heights greater than 3.6

m will strongly influence evolution of the storm-bar and trough. Analysis of wave data from an oil platform approximately 80 km off Lakes Entrance, indicates that the number of high wave events exceeding 3.5 m occurs on average once per month and 4.5 m waves occur on average twice per year (O'Grady and McInnes, 2010). Under these circumstances, it is plausible that the required significant wave height event to break on the storm-bar will occur every few months. Hence the multi-month survey provides a reasonable resolution of the temporal variability of the storm-bar. In the next section the bed evolution changes in the storm-bar and trough are directly modelled (at 10s time steps), in order to investigate their variability.

The transport prediction from bedform movements between the 11-15 m-depth contour is around 100-200 $m^3$ eastward over the eight-month period. This is a small fraction of the CERC empirical-model estimates of 100,000 $m^3$ transport averaged over a year ($m^3$/yr), which were predicted in the westward direction (GHD, 2013). The difference is entirely expected because, the CERC equation estimates the cross-shore integrated longshore transport, including the strong wave-driven transport between the 0-12 m depth contours, where the dune bedforms were absent (washed out). In the next chapter, we will directly model the sediment transport between surveys, and compare the modelled volume of transport ($m^3$) at each grid cell between the 11-15 m depth contours with the estimates from the bedform tracking.

# 6. HINDCAST SEDIMENT TRANSPORT SIMULATIONS

Chapter two introduced the TELEMAC modelling system and chapter three described the method of model configuration. In this chapter validation is provided for each of the three models within the TELEMAC system. In the first section of this chapter, the TELEMAC2D longshore flow boundary conditions are tested and compared with measured coastal currents. In the second section, the TOMAWAC waves are validated against buoy measurements and the additional effect of waves to TELEMAC2D flow is presented. In the third section, the SISYPHE morphodynamics are validated against the analysis in the previous chapter. Model sensitivity is tested against boundary conditions, depth-induced wave breaking parameterisations and different sediment grain size combinations to identify model uncertainty. In the fourth and final section of this chapter, model predictions are provided of the net sediment transport field over the ~3.7 yr hindcast period from the TELEMAC, CERC and the new NMB-LM empirical equation is tuned to the TELEMAC simulations. The ~3.7 yr hindcast climate is then compared to the ~30 yr CERC and NMB-LM equation prediction.

## 6.1 Hydrodynamics Boundary Forcing/Nesting

Boundary forcing (or nesting) of the coastal flow and water levels from (within) the all-of-Australia ROMS hindcast posed the largest challenge for hydrodynamic TELEMAC2D model setup (Section 3.6.2). Simply applying the ROMS boundary flow and water levels to all ocean boundary points resulted in an over-constrained solution, and over-correction of the internal flow field. As suggested in the TELEMAC2D user manual, the option to vary the prescribed- and free-boundary conditions based of the flow direction was implemented to relax the boundary flow (Section 3.6.2). Sensitivity runs of the free- and prescribed-boundary conditions are shown for a strong westerly flow in four subplots within Figure 6.1. The first subplot (Figure 6.1, a) displays the stream flow from the prescribed longshore gradient in the water level alone (without flow boundary input). Here the flow reduces in speed towards the shore due to depth effects, such as bottom roughness (Figure 3.13). The second subplot (Figure 6.1, b), shows reduced internal flow from the addition of a prescribed ROMS coastal flow input on the upstream boundary to the right of the plot, with a free boundary downstream to the left. The bottom row of subplots in Figure 6.1, (c and d) show the relaxed constraint of the Thompson boundary condition introducing unwanted advection within the domain. While the Thompson boundary condition has been suitable for other model configurations, it is shown to be unsuitable for this model setup, for reasons that could include time step, steep bathymetric gradient and the size of the grid domain. For all proceeding results the configuration of subplot Figure 6.1 b) was used.

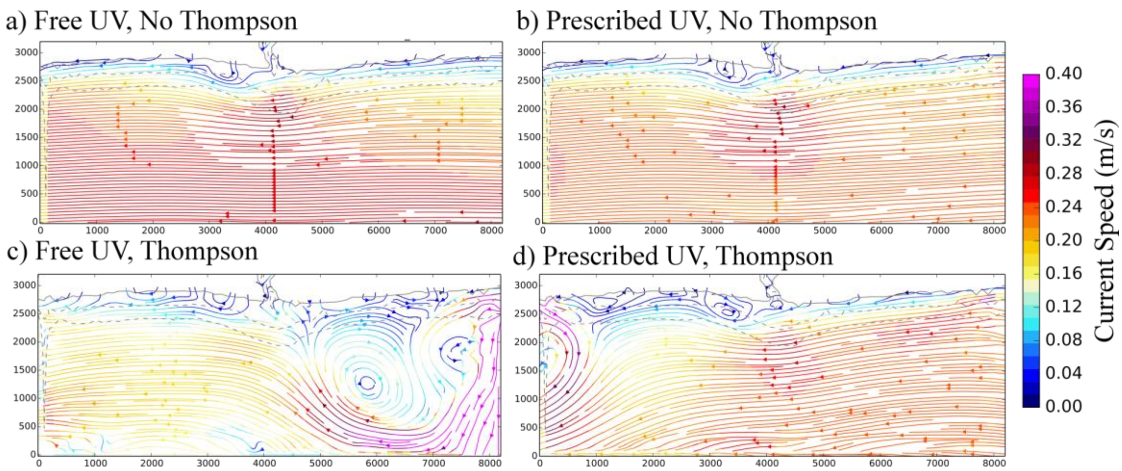


**Figure 6.1 Maps of TELEMAC2D boundary forced longshore flow configuration comparison.**

All four subplots are for the same westward flow examples for 2009-09-10 17:30. All plots are forced with a gradient in the water level from two neighbouring ROMS hindcast output points. The top row of figures have Thompson boundary conditions excluded while in the bottom row figures they are included. The left column has a free flow boundary condition and the right column has boundary currents prescribed. Longshore (cross-shore) direction on the horizontal (vertical) axis.

Model output located at the ADCP measurements demonstrates that the TELEMAC2D (with ROMS boundary forcing) is able to replicate the measured ADCP alternating tidal currents (Figure 6.2). However, the model fell well short of the observed peak longshore flow on the 27$^{th}$ of September 2009, and at other times. This is possibly due to non-modelled effects, such as waves (included in the next section), but also steric (temperature and density) and vertical 3D induced flow. Further validation of the ROMS boundary forcing is provided in Section 4.1.3.

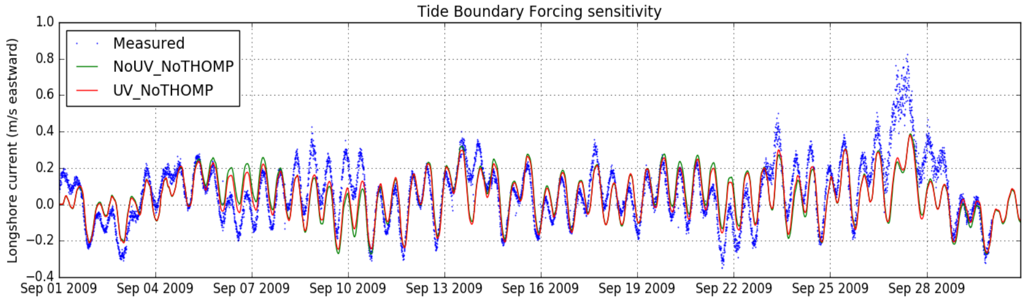


**Figure 6.2 TELEMAC2D boundary forced longshore flow comparison with measured.**

The plot shows the time series comparison of the measured ADCP longshore current (blue dots) with internal longshore flow with (red line) and without (green lines) ROMS flow boundary forcing. It should be noted that observations include other effects on longshore flow including wave- and steric- induced flow. (See Figure 4.1 for weather conditions)

## 6.2 Waves and Wave-Driven Currents

The nesting of the TOMWAC model within the CAWCR wave hindcast, 2D spectral WW3 output, was tested first. This was done by checking the bulk parameter of significant wave height (*Hs*) computed for an internal grid point within the TOMAWAC grid matched with the bulk *Hs* of the wave hindcast output. The two models show excellent agreement with each other (Figure 6.3) and following from section 4.1.2 the wave hindcast shows reasonable agreement with the wave buoy.

In this section, two depth-induced wave breaking formulations are investigated. Namely, the IH1984 (Izumiya and Horikawa, 1984) and BJ1978 (Battjes and Janssen, 1978) models. The IH1984 formulation is investigated because it takes into account the wave period and wavelength in the formulation of depth-induced breaking. This is important because, longer period waves have longer wavelengths ($L = Tp(gh)^{0.5}$ in shallow water), so are less steep and will therefore break later (in shallower depths) than shorter period steeper waves. The BJ1978 in its traditional form of the wave breaking parameter (the relation of wave height to water depth), does not take into account the effect of wave period and wave steepness. As a result the BJ1978 model was also tested with Miche's criterion (BJ1978_M) for wave breaking (Miche, 1944). The Miche criterion frees the wave height from the strict condition of the relation of wave height for a given depth, allowing longer period (wavelength) waves to maintain their height in shallower depths.

Figure 6.3 displays little to no difference in the different formulations of the depth-induced breaking at the wave buoy. Moving from the validation site near the ocean boundary to the coastline, Figure 6.4 shows the profile of *Hs* as the waves move towards the shore for different source term formulations. For the situation of no source terms, the waves steepen as they move towards the coast, representing the processes of wave shoaling. For just triad source forcing the shifting of wave energy to higher frequencies results in an unrealistic growth of bulk spectral significant wave height. It is possible that this is due to the low model temporal and spatial resolution. For the example of just including bottom friction there is little effect in the nearshore domain, in shallow depth the model has a cut of limit of a 1 to 1 wave height to water depth ratio, which reduces the wave height to zero at the coast.

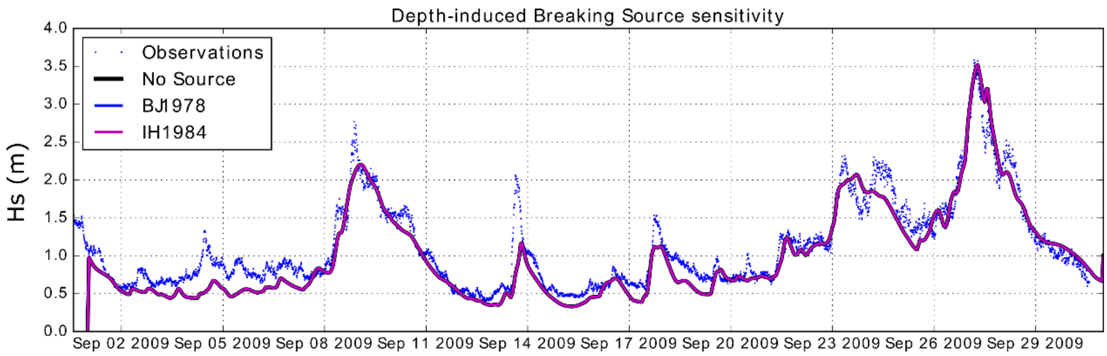


**Figure 6.3 Time series of *Hs* (m) for different breaking formulations.**

Plotted are overlapping model output (lines) at the location of the wave buoy measurements (blue dots) in approximately 20 m of water. The wave buoy and model output was approximately 200 m landward from the midpoint of the ocean boundary.

The cross-shore wave profile of the BJ1978 formulation in its traditional form shows a linear relationship of the height to depth relationship from a depth of 9 m to the coast (Figure 6.4). The BJ1978 with the Miche criterion (BJ1978_M) shows a non-linear relationship from a depth of 9 m to the coast, allowing taller waves in shallower water compared to the traditional BJ1978 method. The IH1984 method also exhibits a similar nonlinear profile, however the waves start to break in shallower water. Despite these differences, the different formulations provide similar results when considering that most of the sensitivity in the wave breaking profile is controlled by coefficient for breaking. As a result, it was decided to select the more commonly used BJ1978 method over IH1984 and to use it with the Miche criterion (BJ1978_M) to take into account the processes of wave steepness in the hindcast simulations. The sensitivity tests of the depth-induced wave breaking coefficient ($\gamma = 0.4, 0.8, 0.9$) are compared in the next section, with the SISYPHE sediment transport simulations.

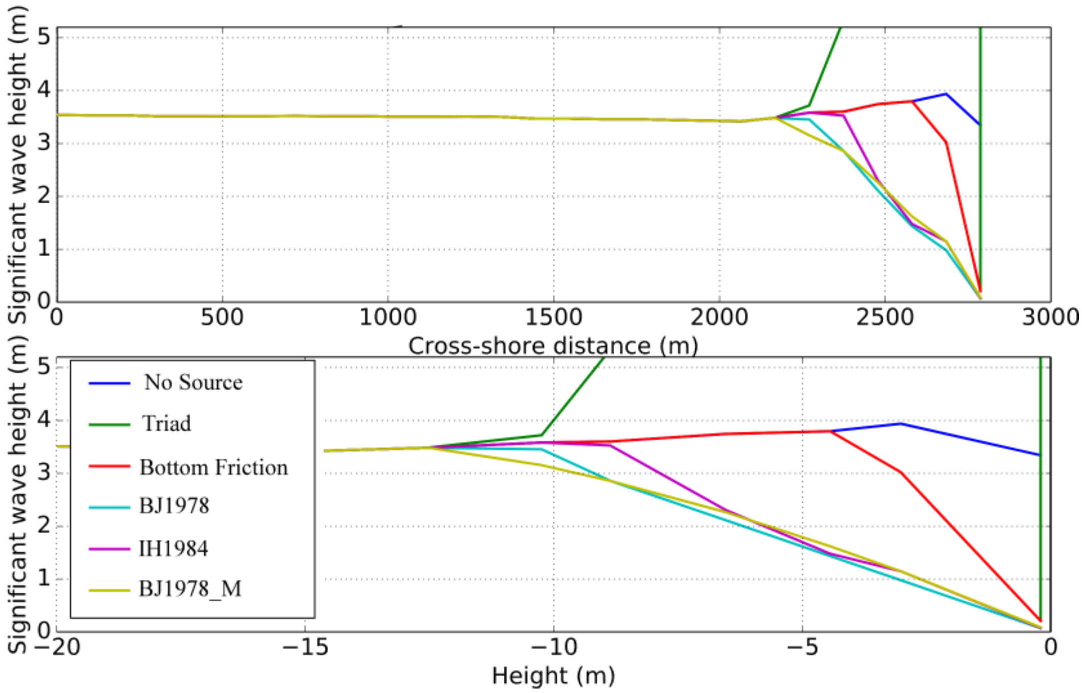


**Figure 6.4 Significant wave height profile for different wave source term.** The top plot shows the wave breaking across the cross-shore profile near the peak of the storm 2009-09-27. The bottom plot is the same data as the top, but the significant wave height is plotted against the water depth (negative height) on the x-axis. No source (blue line), with just triad (green), JONSWAP bottom dissipation (red), BJ1978 (cyan), IH1984 (purple) and BJ1978 with Miche breaking criteria (yellow). All source terms use default parametrisation.

The TOMAWAC model will influence flow in the TELEMAC2D model by applying the forces that result from wave shoaling (directed offshore) and strong depth-induced wave breaking dissipation (directed onshore) to the hydrodynamics (Equation 3-16). The effect of including waves in the hydrodynamics shows increased westward flow for the whole domain for the case of a strong $Hs$ = 2-2.5m, during a westward event around the 10$^{th}$ of September 2009. The largest flow increase (around 20 m/s) was between the 2 and 12 m depth contours, where depth-induced wave breaking occurs (Figure 6.5). The cross-shore transect of the longshore flow is taken from 2000 m longshore model-grid position, and plotted as Hovmöller diagrams, which compare the time series of the oscillating tidal flow with those without tidal flow plotted against the cross-shore position (Figure 6.6, top panel). The middle panel of Figure 6.6 shows the additional effect of waves, increasing the flow speeds in the vicinity of the breaking waves. When very large waves are present the effect of waves on the flow extends to the ocean boundary. At certain phases of the tidal cycle, the wave-driven flow at the coast is in the opposite direction to wind- and tide-driven flow in deeper water.

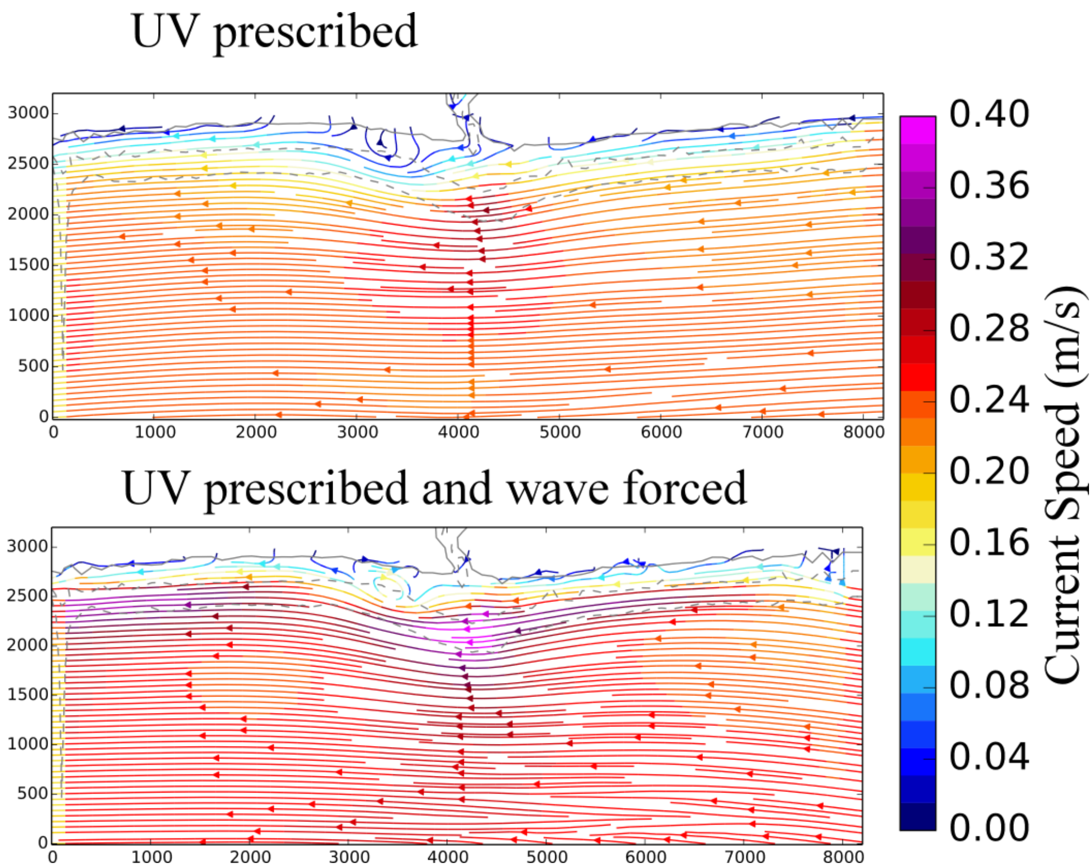


**Figure 6.5 Maps of the effect of including waves in the hydrodynamic simulations.**

Displayed are stream plot diagrams, showing westward flow for 2009-09-10 17:30. The top plot is the TELEMAC2D modelled longshore flow forced by prescribed water level gradient and ROMs flow. The bottom plot is identical to the top, but with TELEMAC2D-TOMAWAC coupled wave radiation stress force. Increased flow in depths between 5- 12m-depth contour are a result of strong wave breaking (breaking parameter = 0.8). Longshore (cross-shore) distance (m) on the horizontal (vertical) axis.

The TELEMAC2D model will modify the TOMAWAC modelled waves under the influence of currents in two optional processes. The first process, modelled by the governing dispersion equations (Equations 2-7 to 2-10), accounts for the well-established effect of *background currents*, which encompasses, modifying the wave spatial coordinates (displacement), direction (refraction) and frequency (Doppler shift) of the wave spectrum. The second process, is the effect of *wave breaking from strong currents* (Van Der Westhuysen, 2012). The effect of wave breaking from strong current dissipation was not resolved correctly with the required model time step and grid resolution. The Hovmöller plot (bottom panel of Figure 6.6) displays that standing eddies (numerical noise) were present in the simulations during large wave events. As a result, the effect of wave breaking from strong currents was not included in the final hindcast simulations, due to limited computational resources to resolve the complex coupled process.

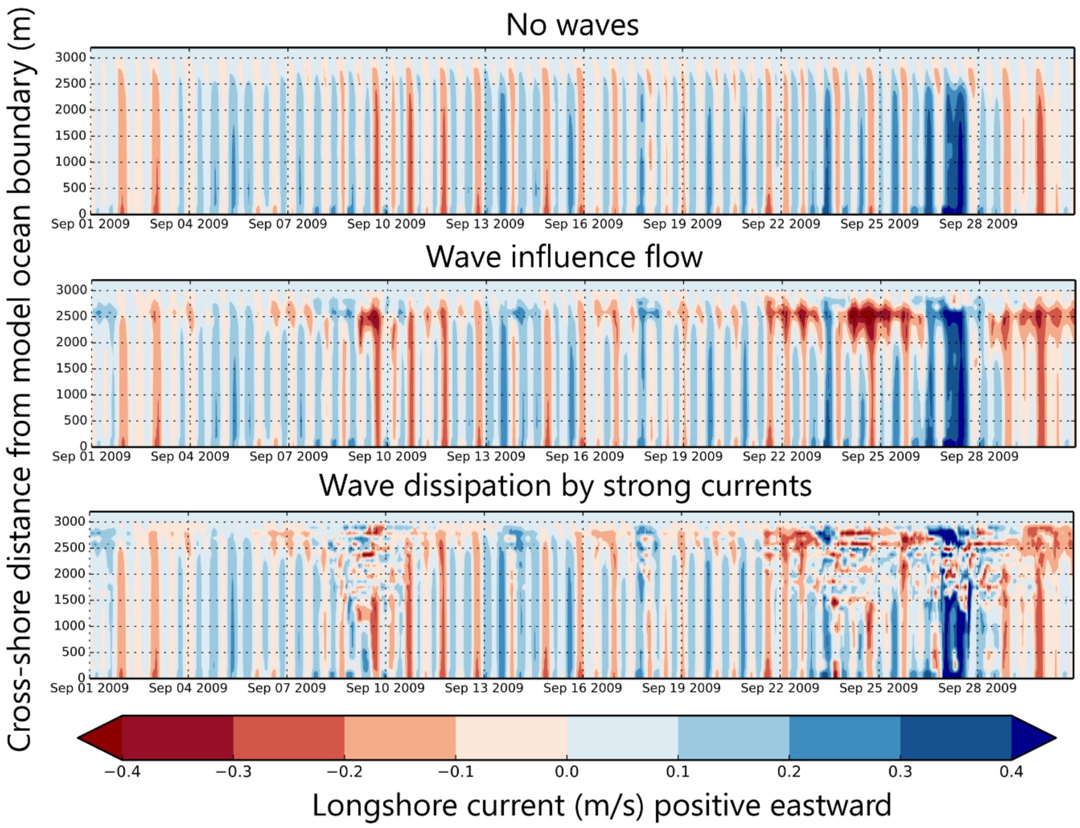


**Figure 6.6 Hovmöller diagram; time series of the cross-shore impact of waves on flow.**

The three plots have time along the horizontal axis from the same single cross-shore transect on the vertical axis. Transect is 2025 m from origin (over the west dredge disposal site). Positive (negative) values are eastward (westward) longshore flow coloured blue (red). The top panel shows the semidiurnal tidal wave propagating longshore, with reduced flow at the coast. The middle plot shows the influence of waves near the shore during moderate wave conditions, extending to deeper water for the larger events around the 27th of September. The bottom panel shows standing eddies and numerical noise from wave dissipation from strong currents.

## 6.3 Morphodynamics

Six sensitivity simulations were tested over the 3rd, 8th and 13th survey periods (see Table 3-3 for dates). The sensitivity runs comprised three different breaking parameters ($\gamma$ = 0.4, 0.8, 0.9) and two different sediment diameter combinations in mm ($d_{50,i}$ = {0.3,0.4,0.8} or {0.25,0.5,0.7}) (Section 3.6.4). The morphodynamics are analysed for two variables, *bed evolution* and *volume transport* (see introduction to Chapter 5 for further details).

### 6.3.1 Bed Evolution (erosion/accretion)

Maps of the final bed evolution over the third survey period show high sensitivity to the depth-induced breaking parameter (γ), and less sensitivity to the second combination sediment diameters (Figure 6.7). The maps show stoss to lee transport across the repeating bedforms (longshore sandwaves and bars in the surf zone) alternating between erosion (blue) and accretion (red) as seen in Putzar and Malcherek, (2012). The smaller γ=0.4 dissipates wave energy in deeper water over a wide gentle profile. The larger γ=0.8 allows taller waves into the shallower waters, where the profile gradient is steep, and the resulting force (Equation 3-16) is greater. The second configuration of sediment class in shallower depth shows little change in bed evolution.

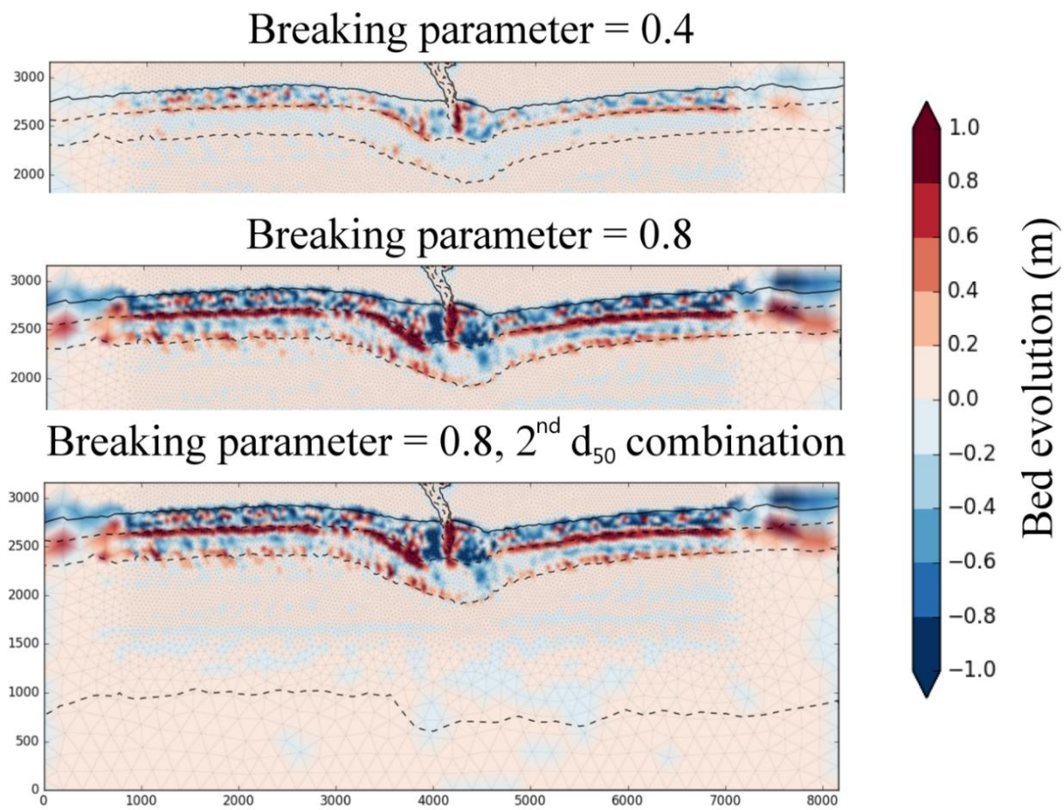


**Figure 6.7 Maps of Bed evolution sensitivity to different breaking parameters and sediment grain size configuration.**

The three panels show the modelled bed evolution from three sensitivity simulations over the third survey period (2009-10-05 to 2009-11-09). The top panel shows less bed evolution from a small breaking parameter ($\gamma$=0.4) compared to the higher breaking parameter ($\gamma$ = 0.8) in the middle plot with the same sediment grain size configuration ($d_{50,i}$ = {0.3,0.4,0.8}). The bottom plot shows the second configuration of sediment class diameters ($d_{50,i}$ = {0.25,0.5,0.7}) has little impact on bed evolution compared to the middle plot. Longshore (cross-shore) distance (m) on the horizontal (vertical) axis.

The first method of morphodynamic validation was derived from bathymetric evolution. The bathymetric change was compared between the model and the survey in the vicinity of the storm trough (100-200 m from the coast) and storm bar (200-300 m from the coast) (see Figure 3.2 for the initial profiles and Figure 5.4 for the temporal changes in height). Initial simulations, with a breaking parameter of 0.8, resulted in the model only resolving 5% of the bed evolution heights. Consequently, all results presented are the calibrated model solution, i.e. multiplying Soulsby Van Rijn transport by 20 (Equation 3-18). The calibrated model does a reasonable job of capturing the magnitude and direction (down/erosion or up/accretion) of bed evolution in all but a few cases (Figure 6.8). Any differences could be a result of dredge disposal between surveys, the effect of the channel, or under resolving the forcing (e.g. 3D effects). The validation statistics on all data points results in a Pearson's R-value of 0.9, a P-value 6.2E-14 and a standard error of 0.068 m.

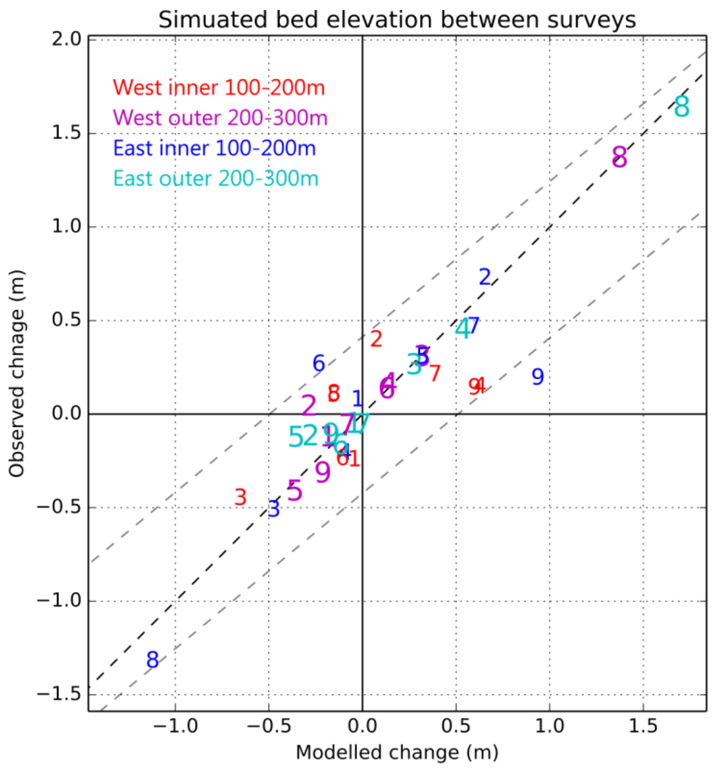


**Figure 6.8 Model bed evolution validation in the location of the storm-bar and trough at both single-beam survey sites.**

Plotted are the model bed elevation median changes over the first nine simulations (10 surveys), compared to the observed (single-beam) change in four zones. Numbers correspond to simulation period. The inner 100-200 m metres zone is the approximate location of the storm trough, and the outer 200-300 m zone is the location of the storm bar. The dashed grey line is plus or minus one standard deviation of a linear fit to all data. The dashed black line is the one-to-one line.

### 6.3.2 Volume Transport

Sediment transport is presented in different ways in the literature (See introduction to Chapter 5). It can be presented as a point source or integrated across a cross-shore profile or integrated over time.

Net longshore sediment transport is plotted in Figure 6.9 for the six sensitivity simulations (six line colours) over three survey simulation periods (3 panels). The three simulation periods represent a situation of westward transport, mixed transport and eastward transport respectively. These plots show that most of the transport predicted by TELEMAC occurs during individual storms. The top 30 $q_{TL}$ longshore sediment transport rates were found by clustering events above an absolute threshold of 0.1 $m^3s^{-1}$ and combining events separated by less than 72hrs (Table 6-1).

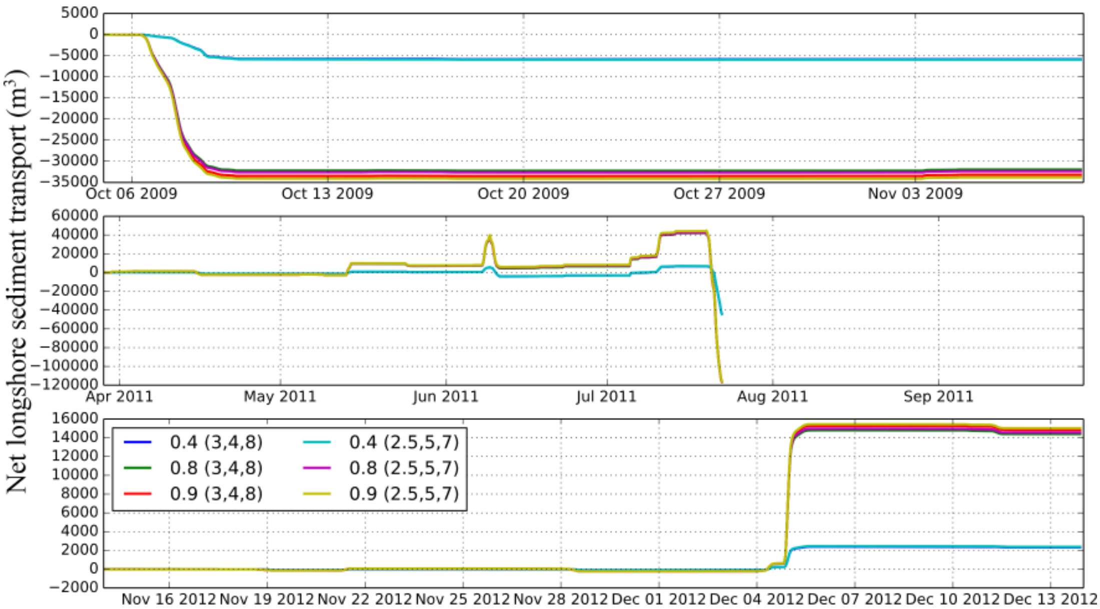


**Figure 6.9 Time series of modelled net longshore sediment transport $Q_T$ ($m^3$) sensitivity for 3 breaking parameters and two sediment grain size combinations.**

Each of the three panels show six model sensitivity simulations (coloured lines), for the 3rd (top), 8th (middle) and 13th (bottom) model survey simulation periods. The legend describes the depth-induced wave breaking parameter ($\gamma$) and sediment class mean diameters ($d_{50}$) in $10^{-1}$ mm in the format $\gamma$ ($d_{50,1}$, $d_{50,2}$, $d_{50,3}$). The Positive (negative) values on the vertical axis represent transport towards the east (west).

The third survey period, from the start of October to November 2009, spans 35 days (Table 3-3). The period was dominated by a single westward event, which was the 17th largest TELEMAC modelled transport rate event (Table 6-1).

The eighth survey period, from March to September 2011, was the longest at 183 days (~6 months) and occurred over the austral winter months. TELEMAC predicted a mixture of three eastward events ($16^{th}$, $15^{th}$ and $13^{th}$ highest transport rate events in succession) followed by a single westward event ($3^{rd}$ highest transport event). The model was not able to provide a stable solution of bed-evolution for the full survey duration, as cumulative errors, such as no sediment transfer budget at the boundaries, crept in. Consequently, results are presented for the first 115 days of the simulation, before it failed (Figure 6.9 middle panel). After 115 days the model predicts the increase in the bed evolution in the location of the storm-bar, and decrease in the location storm-trough measures between the $8^{th}$ and $9^{th}$ surveys, 183 days apart (Figure 6.8). During the non-model TELEMAC period the CERC equation predicts similar westward event around the $10^{th}$ of August.

The thirteenth survey period, from November to December 2012, is the shortest at 30 days. This period is dominated by an easterly event, which was the $7^{th}$ largest transport-rate event modelled by TELEMAC.

**Table 6-1 the top 30 longshore sediment transport rate (*Q*) event-maxima during the TELEMAC simulations.**

| | Survey | | $H_s$ | $U_l$ | $\theta_i$ | TELEMAC | CERC | NMB-LM |
|---|---|---|---|---|---|---|---|---|
| Rank | Period | Date time | m | m/s | deg. | $m^3/s$ | $m^3/s$ | $m^3/s$ |
| 1 | 10 | 2012-06-04 23:00 | 5.09 | -0.15 | -30.50 | -7.31 | -1.23 | -7.15 |
| 2 | 2 | 2009-09-27 7:00 | 3.71 | 0.40 | 30.60 | 1.97 | 0.56 | 2.44 |
| 3 | 8 | 2011-07-21 5:45 | 3.63 | -0.21 | -42.25 | -1.87 | -0.60 | -1.68 |
| 4 | 7 | 2011-03-22 0:15 | 3.41 | -0.12 | -54.40 | -1.62 | -0.49 | -1.26 |
| 5 | 5 | 2010-05-30 1:00 | 3.23 | -0.29 | -55.20 | -1.23 | -0.42 | -1.47 |
| 6 | 10 | 2012-03-08 10:00 | 3.29 | -0.08 | -45.90 | -1.16 | -0.47 | -0.80 |
| 7 | 13 | 2012-12-04 23:00 | 3.10 | 0.36 | 28.30 | 1.12 | 0.34 | 0.73 |
| 8 | 11 | 2012-08-09 10:15 | 2.95 | 0.36 | 26.53 | 0.90 | 0.29 | 0.51 |
| 9 | 5 | 2010-06-09 16:00 | 2.95 | 0.40 | 29.30 | 0.81 | 0.31 | 0.64 |
| 10 | 4 | 2009-11-30 9:15 | 3.01 | -0.18 | -31.97 | -0.67 | -0.34 | -0.41 |
| 11 | 12 | 2012-11-01 11:00 | 2.87 | 0.23 | 28.40 | 0.65 | 0.28 | 0.32 |
| 12 | 5 | 2010-02-14 23:00 | 2.99 | -0.10 | -50.10 | -0.63 | -0.37 | -0.53 |
| 13 | 8 | 2011-07-10 16:15 | 2.97 | 0.23 | 26.35 | 0.62 | 0.29 | 0.36 |
| 14 | 11 | 2012-09-07 12:15 | 2.80 | 0.39 | 29.65 | 0.61 | 0.27 | 0.47 |
| 15 | 8 | 2011-06-08 3:30 | 2.94 | 0.05 | 26.65 | 0.58 | 0.29 | 0.24 |
| 16 | 8 | 2011-07-05 8:00 | 2.72 | 0.43 | 28.90 | 0.57 | 0.25 | 0.43 |
| 17 | 3 | 2009-10-07 13:00 | 2.76 | -0.12 | -21.70 | -0.39 | -0.21 | -0.15 |
| 18 | 8 | 2011-05-13 10:00 | 2.81 | 0.13 | 26.90 | 0.35 | 0.26 | 0.21 |
| 19 | 5 | 2010-08-02 4:15 | 3.07 | 0.15 | 6.87 | 0.35 | 0.09 | 0.09 |
| 20 | 6 | 2010-09-16 12:15 | 2.63 | 0.38 | 29.40 | 0.33 | 0.23 | 0.32 |
| 21 | 1 | 2009-07-04 16:15 | 2.83 | 0.35 | 20.70 | 0.30 | 0.21 | 0.31 |
| 22 | 11 | 2012-07-31 22:15 | 2.32 | -0.25 | -40.75 | -0.27 | -0.19 | -0.14 |
| 23 | 10 | 2012-05-13 1:00 | 2.40 | 0.28 | 27.10 | 0.24 | 0.17 | 0.13 |
| 24 | 9 | 2012-03-01 2:00 | 2.30 | -0.08 | -58.50 | -0.23 | -0.17 | -0.14 |
| 25 | 14 | 2013-02-28 13:00 | 2.56 | -0.09 | -19.20 | -0.19 | -0.16 | -0.08 |
| 26 | 14 | 2013-01-08 11:00 | 2.36 | -0.01 | 25.90 | 0.19 | 0.16 | 0.07 |
| 27 | 5 | 2010-05-14 13:30 | 2.40 | 0.00 | -33.25 | -0.18 | -0.20 | -0.09 |
| 28 | 7 | 2011-03-01 5:15 | 2.27 | 0.26 | 28.03 | 0.18 | 0.15 | 0.09 |
| 29 | 5 | 2010-05-25 11:15 | 2.20 | -0.18 | -62.72 | -0.14 | -0.14 | -0.14 |
| 30 | 5 | 2010-04-12 2:30 | 2.36 | 0.31 | 32.05 | 0.13 | 0.19 | 0.15 |

Bed evolution validation and calibration, was used to identify a single setup for the hindcast and climate simulations. The simulation where $\gamma$ ($d_{50,1}$, $d_{50,2}$, $d_{50,3}$) = 0.8 (0.3, 0.4, 0.8) was selected as the most appropriate hindcast model setup. The net longshore sediment transport is compared for the six sensitivity simulations for the three time periods to the selected setup (Table 6-2). The values in Table 6-2 provide an indication of model setup uncertainty. For this selected hindcast setup, TELEMAC predicted that the largest net transport occurs in the 8th survey period. This prediction is larger than 100,000 $m^3m^{-1}$ annual transport estimated by the CERC equation (GHD, 2013). The smaller $\gamma$ = 0.4 simulations predicts between 62 and 83% less transport than the chosen setup. The larger $\gamma$ = 0.9 predicts between 0.6 and 3.8% more transport than the chosen setup. The second combination of sediment grain sizes ($d_{50,i}$ = {0.25, 0.5, 0.7}) predicts between 0.4 to 1.2% more transport than the chosen setup. Excluding the $\gamma$ = 0.4 simulations which did not show suitable validation to the bed evolution of the storm-bar and trough, the internal model longshore transport uncertainty (sensitivity) to model setup is in the order of ±3 to 6% of the model prediction.

**Table 6-2 Modelled net longshore sediment transport $Q\delta$ ($m^3$) sensitivity.**

The model sensitivity to three depth-induced wave breaking parameters $\gamma$ and two sediment grain size populations (three classes of $d_{50}$) are provided for three sediment survey simulations (3rd ,8th and 13th). Transport estimates are provided for the selected hindcast model setup $\gamma$ ($d_{50,1}$, $d_{50,2}$, $d_{50,3}$) = 0.8 (0.3, 0.4, 0.8) simulation. Other simulations are given as a percentage difference to the 0.8 (0.3, 0.4, 0.8) simulation. Positive (negative) bold values represent transport towards the east (west). Positive (negative) percentages indicate an increase (decrease) in the 0.8 (0.3, 0.4, 0.8) direction of transport.

| $\gamma$, ($d_{50,1}$, $d_{50,2}$, $d_{50,3}$) | Oct 2009 - Nov 2009 | Apr 2011 - Jul 2011 | Nov 2012 - Dec 2012 |
|---|---|---|---|
| 0.4, (0.3,0.4,0.8) | -81.7% | -62.2% | -83.8% |
| **0.8, (0.3,0.4,0.8)** | **-31,958$m^3$** | **-115,907$m^3$** | **14,397 $m^3$** |
| 0.9, (0.3,0.4,0.8) | 3.8% | 0.6% | 3.2% |
| 0.4, (0.25,0.5,0.7) | -81.4% | -61.8% | -83.4% |
| 0.8, (0.25,0.5,0.7) | 1.2% | 0.4% | 1.1% |
| 0.9, (0.25,0.5,0.7) | 5.8% | 0.2% | 4.3% |

The second morphodynamic validation dataset was calculated for net longshore sediment transport (Figure 6.10). Model output was compared to bedform transport estimates made by dune-crest tracking (see Figure 3.5 for images of bedforms and Figure 5.7 for transport estimates). The model agrees with the direction of transport for all except the final survey at the west site (Figure 6.10). The model predicts 100 times (two orders of magnitude) the transport estimated by the bedform tracking method. Several factors could account for this large difference. Firstly, the additional suspended sheet flow transport bypasses the dune transport processes (stoss-to-lee). Secondly, the model is over predicting sediment transport between the 12 and 16 m depth contours. It is also possible that both of these factors are at play.

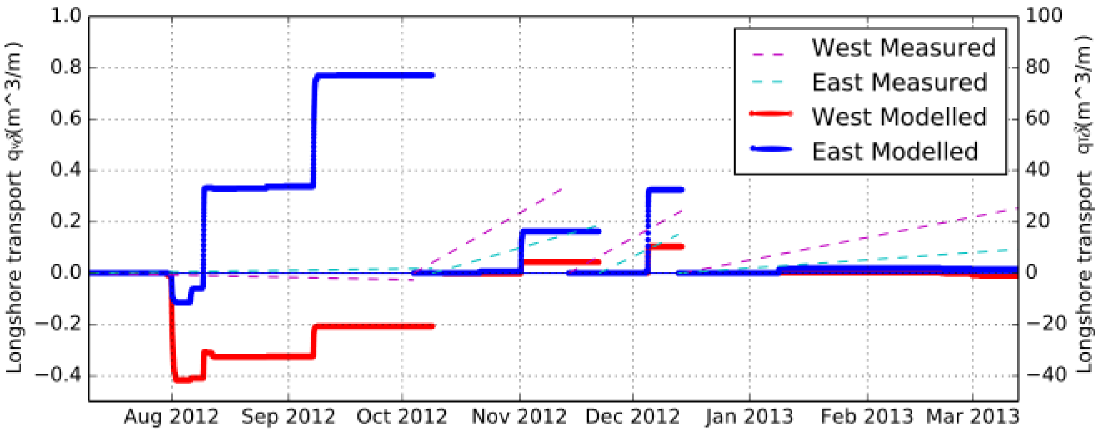


**Figure 6.10 TELEMAC modelled net longshore sediment transport $q_T\delta$ ($m^3m^{-1}$) validation against bedform tracking $q_v\delta$.**

Plotted is the longshore transport estimates from the final five surveys, which were multi-beam survey. Measured bedform (model) transport estimates correspond to left (right) vertical axis. The Dune-crest tracking and TELEMAC model output is analysed between the 12 and 16 m depth contours (see Figure 5.7).

The gridded model sediment transport ($m^3m^{-2}$) over ~3.7 yr modelling period is displayed as a streamflow plot (Figure 6.11). The majority of transport occurs between the 5 and 12 m depth contours. There is reduced transport within 100 m of the coast, due to lower modelled TELEMAC2D flow (Section 6.2). There is also more transport at the western side, which is consistent with the beach erosion (coastline rotation) experience since the opening of the channel, and the difference in the bedform transport estimates (Figure 6.10). The five multi-beam surveys and predicted bedform transport occur during an eight month period of net eastward transport, but over the entire 3.7 years the net transport is predicted to be westward. The net longshore sediment transport rate estimated by TELEMAC per year is 211,598 ($m^3yr^{-1}$) westward (Table 6-3). This is of the order of magnitude of the 100,000 $m^3yr^{-1}$ westward estimates provided in the dredge management report (GHD, 2013).

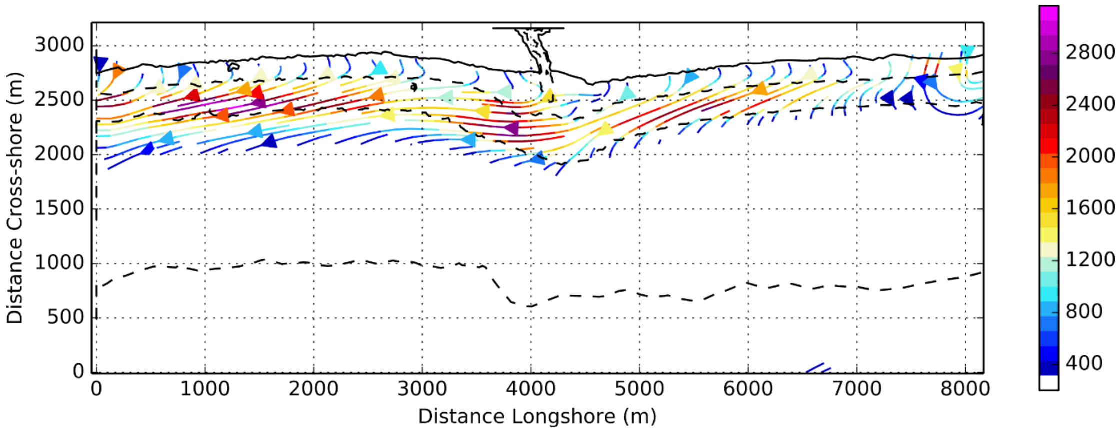


**Figure 6.11 Streamflow plot of the net sediment transport ($m^3m^{-1}$) over the ~3.7 yr TELEMAC simulations.**

The diagram shows the gridded transport, summed over the ~3.7-year period (2009-06-18 to 2013-03-13). Arrows indicate the direction the stream flow of transport and colour indicates the volume of transport per unit horizontal area. The dashed lines show the 0, 5, 12 and 20 m depth contours.

## 6.4 Empirical and Semi-empirical Estimates of Longshore Sediment Transport

The empirically fitted (calibrated) CERC equation (Equation 3-32) to the US coastline is forced with the local ~3.7 yr time-series of bulk wave parameters (CAWCR WW3). The CERC equation shows reasonable agreement with the longshore transport rate ($m^3m^{-1}yr^{-1}$) predicted by TELEMAC over the 3.7 yr simulation period (Table 6-3).

**Table 6-3 Modelled longshore sediment transport rate *Q* estimates averaged per year.**

Note the CERC estimate is calculated over a different period to (GHD, 2013) report.

| Transport per year ($m^3m^{-1}yr^{-1}$) | TELEMAC | CERC | NMB-LM |
|---|---|---|---|
| ~3.7 yr TELEMAC survey simulation period | -211,598 | -193,379 | -214,308 |
| ~32.4yr hindcast ROMs period | Not resolved. | -206,494 | -100,741 |

The time series plot of transport (Figure 6.12) shows that in the periods between storms, the CERC equation predicts more gross transport than the TELEMAC model and during storms, the CERC equation predicts less transport. Over the ~3.7 year period the cumulative effect of the CERC over prediction between storms and under prediction during storms, balances out to match the

TELEMAC storm-driven transport. The reason for the difference between CERC and TELEMAC is that TELEMAC limits transport to occur only when the non-linear combination of coastal flow and orbital wave velocity is above a critical mobility velocity (Equation 3-21). On the other hand, the CERC equation will predict transport for all wave heights. The CERC equation is based on the work of Komar (1971) and was designed for a wave-dominated coast. Komar (1971) offers a second equation that includes the superimposed to-and-fro motion of wind-generated longshore current and tide. A new semi-empirical equation (NMB-LM) is presented to include the effect of currents modelled by TELEMAC and is detailed in Section 3.7. The calibrated values of the NMB-LM model (Equation 3-24) to the TELEMAC simulations are $D_{i=1:4} = \{0.30625, 5.65716, 0.07662, 2.77079\}$. NMB-LM matches the pattern of net longshore transport modelled by TELEMAC, differing in magnitude for only a few storm events (Figure 6.12).

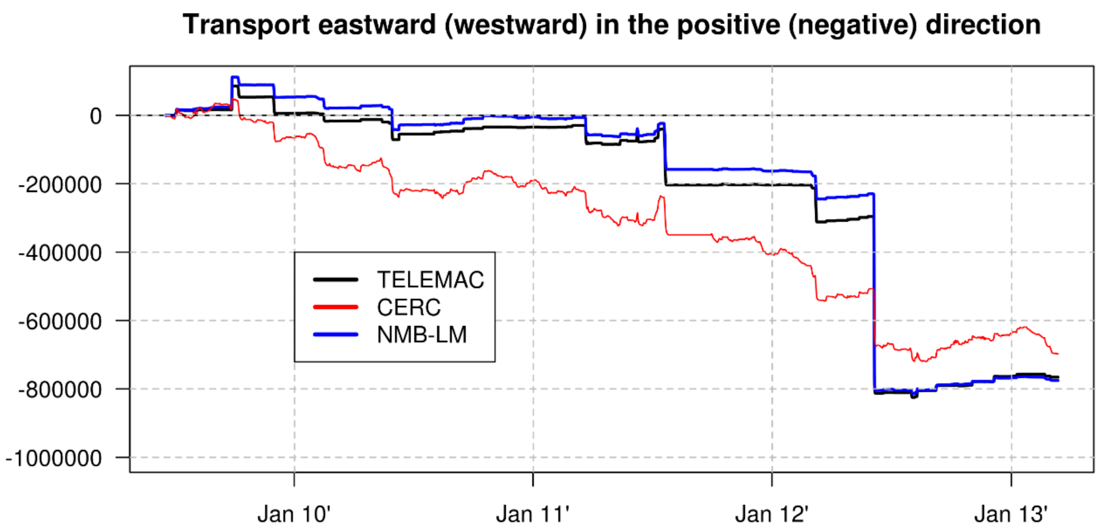


**Figure 6.12 Time series of net longshore transport (m$^3$) from TELEMAC and empirical equations.**

On the vertical axis, positive (negative) values represent transport in the eastward (westward) direction.

The empirical model estimates are listed with the top 30 TELEMAC longshore transport rates in Table 6-1 and compared in Figure 6.13. The CERC equation significantly underestimates the TELEMAC modelled longshore sediment transport rate for all events. The calibrated NMB-LM equation provides a better one-to-one estimate of the TELEMAC modelled transport rates. The largest longshore transport rate event (3$^{rd}$-4$^{th}$ June 2012) coincided with the largest wave heights, above 5 m (Table 6-1).

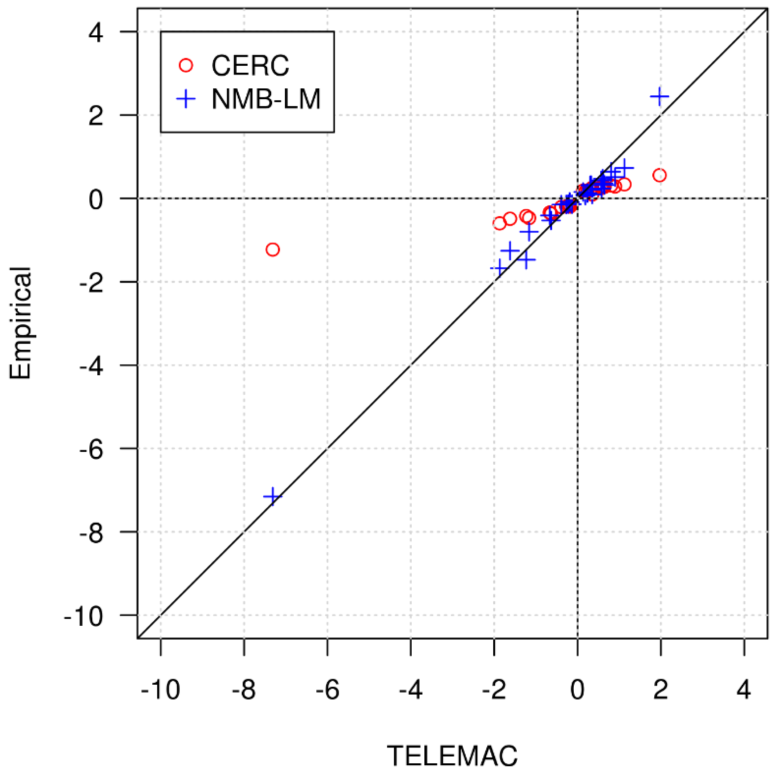


**Figure 6.13 Comparision of TELEMAC event maxima with empirical estimates.**

The empirical equations, CERC and NMB-LM, are plotted against the TELEMAC prediction of the event maxima longshore transport rate ($m^3m^{-1}s^{-1}$). (See Table 6-1 for values)

The time series plot for the period of the largest transport event displays the impact of the longshore wind-tide flow to modify the signal of the TELEMAC resolved transport (Figure 3.14). During this event, the incident wave direction was constantly from -30° (waves from the south east). The peak wave height of *Hs* ~6m, does not coincide with peak westward transport, due to the strong eastward tidal flow opposing (reducing) the westward flow. The NMB-LM equation is able to capture some of the wave-current transport non-linearity. While the NMB-LM equation matches TELEMAC at the time of peak transport, it over predicts the transport at other times during this event.

Overall, this analysis demonstrates the suitability of the one-line NMB-LM equation to capture the broad scale TELEMAC-derived bulk estimates of net longshore sediment transport (Figure 6.12). In addition, it captures the detailed transport-rates to some extent (Figure 6.13). The advantage of the simple, semi-empirical model is that it provides an efficient method for extrapolating the TELEMAC prediction to the full ~30 yr hindcast estimates of the net longshore sediment transport.

The longshore transport calculated for the NMB-LM equation over the ~30-yr hindcast estimates 100,741 $m^3m^{-1}yr^{-1}$ of westward transport (Table 6-3). This is around half the amount predicted by TELEMAC, CERC and NMB-LM over the ~3.7 yr TLEMAC simulation period. It is worth noting, that the top transport event in the NMB-LM ~30 yr hindcast occurs during the shorter ~3.7 yr period (Table 6-1), which could alter the predicted transport climate.

The ~30 yr NMB-LM hindcast transport estimate is also around half the amount predicted by CERC over the same period. This could be a result of few big storms, and more wave energy between-storms in the ~30 yr hindcast increasing the CERC-derived transport. The previous section provides validation of TELEMAC transport estimates over the bathymetric surveys. Dynamic changes to the bed elevation and transport outside the survey period are an added source of uncertainty for the ~30 yr hindcast empirical estimate.

The contribution of tidal flow to the TELEMAC modelled transport was approximated with the NMB-LM equation. The input longshore wind-and-tide- driven current (l) in the NMB-LM model (Equation 3-32) was offset by six hours, to 'reverse' the semidiurnal tidal flow. This resulted in a 2% decrease in the westward net longshore sediment transport. This result highlights the small, secondary importance of wind-tide-driven flow, compared to wave-driven transport in the full transport climate estimated by the models.

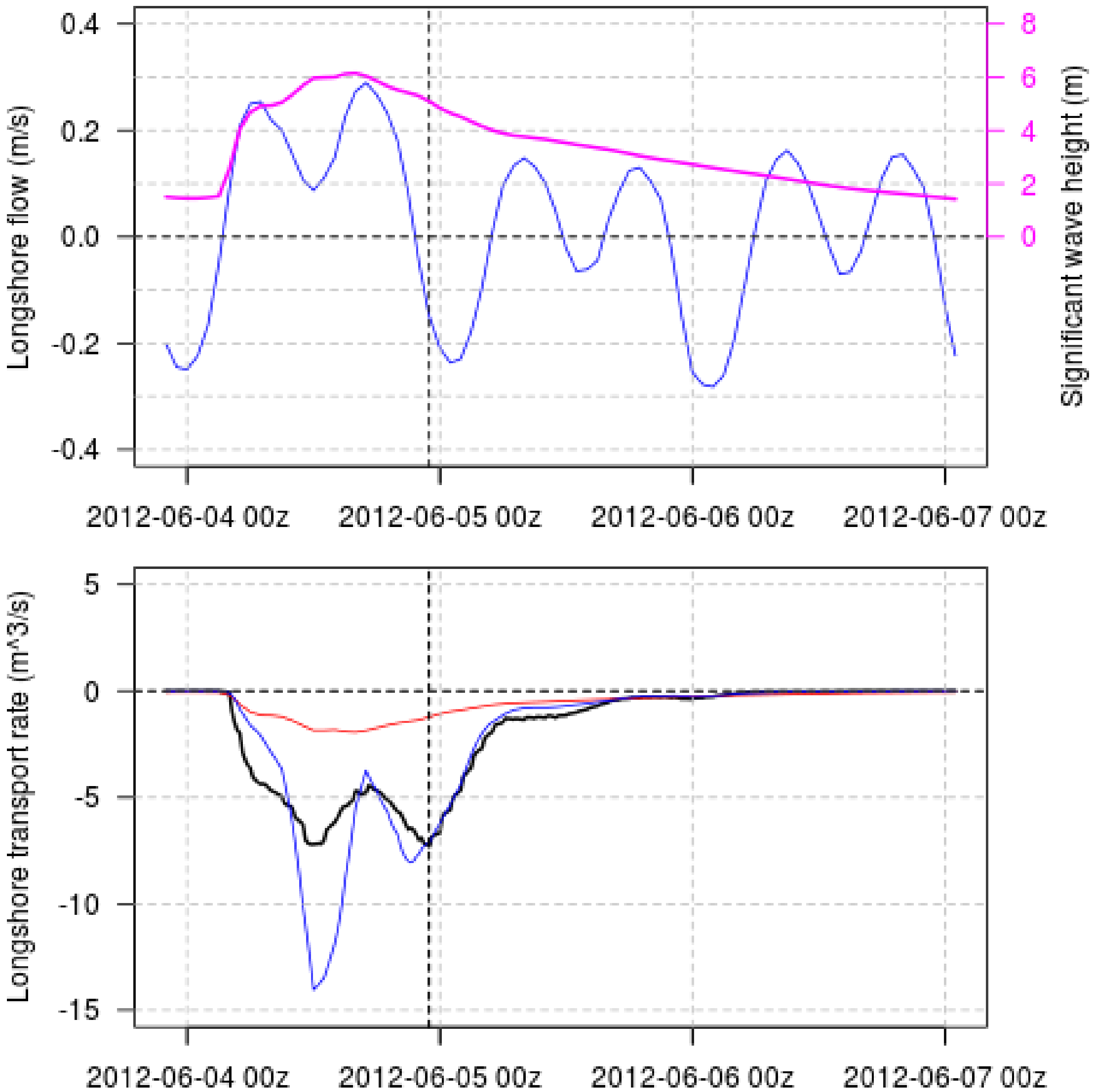


**Figure 6.14 Timeseries model comparision of the top TELEMAC modelled longshore transport rate *Q* event.**

The top plot shows the ROMS longshore boundary flow (blue; left vertical axis) and significant wave height (magenta; right vertical axis). The bottom plot is the TELEMAC longshore transport rate ($m^3s^{-1}$) estimate (black), CERC (red) and NMB-LM (blue). Transport is positive (negative) in the eastward (westward) direction.

## 6.5 Discussion

This chapter covered a number of modelling challenges. Several methods were considered to address the challenges. This was done so that the final results are clearly interpretable. To summarise:

**The challenges/questions addressed in this Chapter were:**

1) Nesting ROMS flow boundary condition in TELEMAC.
2) Identifying which wave source terms to model (e.g. triads, strong dissipation by currents).
3) How should the depth-induced wave breaking be modelled?
4) Analysing the suitability of the bedform-crest tracking method.
5) Does most of the gross transport occur during the period between storms or during storms?
6) Is the ~3.7 year TELEMAC simulation long enough to capture the present-day transport climate?

**The challenges were addressed in each case by:**

1) Validating hydrodynamic, wave and sediment transport models against the available *in-situ* measurements.
2) Where validation wasn't directly possible, questions related to model setup were explained through sensitivity experiments/simulations.
3) The sensitivity simulations were then used to quantify the model uncertainty.
4) A new semi-empirical equation was then developed to efficiently extrapolate the TELEMAC results to the ~30 yr period.

**The actions produced the following results:**

1) Validated the TELEMAC transport model with quantified uncertainty.
2) A new NMB-LM model to extrapolate to ~30 yr transport.
3) A multi-model present-day transport climate was presented.

Conclusions on the sediment transport models are provided in Section 8.3. Chapter 9 provides future opportunities for sediment transport modelling.

# 7. CLIMATE CHANGE SEDIMENT TRANSPORT SIMULATIONS

The previous chapter described the validation of the sediment transport model and provided a prediction of the longshore transport climate. In this chapter, GCM-downscaled climate Change Factors (CF) are used as boundary forcing to simulate the effect of climate change as described in Section 3.6.5. The calculated GCM ensemble monthly mean CF values for currents and waves (Equations 3-31 and 3-33) are shown in Table 7-1.

**Table 7-1 GCM ensemble monthly mean, climate CF downscaling values.**

The values were calculated by the method described in Section 3.6.5 from the hindcast monthly data and normalised climate anomalies (Figure 4.8). The negative (positive) current change values indicate that flow is towards the west (east). Negative (positive) wave-transport-directional CF values are the result of more wave energy from a westward (eastward) direction. The wave-transport-directional CF, is different to a simple change in the mean wave direction, as it takes into account changes in wave height to modify the longshore transport. The wave and current GCM ensemble mean (RCP 8.5) CF predictions are for the end of the 21st century (the years 2081-2100 relative to 1981-2000).

| **Month** | Jan | Feb | Mar | Apr | May | Jun | Jul | Aug | Sep | Oct | Nov | Dec |
|---|---|---|---|---|---|---|---|---|---|---|---|---|
| **Wave $\theta_\Delta$ (°)** | 1.1° | 3.7° | -7.3° | 3.1° | 6.8° | 11.0° | 7.9° | 8.9° | 6.6° | 4.1° | 5.9° | 3.6° |
| **Current (cm/s)** | -1.4 | -0.6 | -0.8 | -1.2 | -0.8 | -0.4 | 0.2 | 0.3 | 0.0 | 0.0 | -0.5 | -0.7 |

The analysis only allows mean changes to climate analysis. Changes to the frequency of occurrence of storms (storminess) are not modelled. The month in which the hindcast storm event occurred (Table 6-1), will impact how the monthly CF values will influence the total hindcast transport climate change.

The outcomes of this chapter demonstrate the sensitivity of the climate to different drivers of change (waves, currents and sea level). The wave and current results presented are the possible magnitude of climate change, identified by a four-member-ensemble GCM prediction, under the highest GHG forcing simulations (RCP 8.5), by the end of the 21$^{st}$ century (the years 2081-2100 relative to 1981-2000). Two time periods are used to replicate the baseline climate in the CF downscaling method. The first baseline climate, is from the ~3.7 years of the shorter validated bathymetric-survey/TELEMAC period (2009-2013). The second baseline climate, is from twenty of the longer ~30 yr hindcast (WW3 and ROMS) periods (1981-2000).

The TELEMAC hindcast simulations were rerun for five climate sensitivity simulations based on the values in (Table 7-1): The driving processes of the five sensitivity simulations were as follows:

1) The boundary water levels were increased by 0.1 m for all times.
2) The boundary water levels were increased by 0.2 m for all times.
3) There was a shift in the boundary wave 2D spectral direction by monthly mean CF value.
4) There was a shift in the boundary wave 2D spectral direction and prescribed boundary current velocity by monthly mean CF value.
5) There was a shift in the boundary wave 2D spectral direction and prescribed boundary current velocity by monthly mean CF value and an increase in the water level by 0.1m for all times.

Where possible, the CERC and NMB-LM equations were recalculated with the CF to compare with the five TELEMAC simulations. It was not possible to simulate the water level increase with the CERC and NMB-LM.

The CERC hindcast was recalculated with the monthly wave-transport-directional CF shift in the incident direction (Equation 3-33) and compared with the third TELEMAC sensitivity simulation. The CERC hindcast was also recalculated with Equation 3-34, to confirm that the monthly mean change in wave-transport-directional CF resulted in the same transport as applying the change GCM identified normalised wave transport anomaly (Figure 4.8). The NMB-LM hindcast was recalculated with the additional wave and current CF values to compare with the third and fourth TELEMAC sensitivity simulations. The CERC and NMB-LM equations were then applied to the 20 yr baseline climate with the additional monthly CF values.

## 7.1 Impact of Increased Water Levels (as an analogue to future sea level rise)

Conceptually, as the TOMAWAC modelled waves approach the shoreline, the increase in water level will not allow the waves to 'feel' the bottom and break until they are closer to the baseline shoreline (Figure 7.1) .As a result of the breaking moving shoreward, there is increased wave-driven transport near the baseline shoreline and reduced wave transport in deeper water. In TELEMAC2D, currents will also be stronger near the baseline shoreline due to less drag friction from the depth dependent Nikuradse equation (Figure 3.13). This lower drag friction, mirrored in the Soulsby-Van Rijn equation (Equation 3-21), will have the inverse effect, reducing sediment transport (stirred up by the wave orbital velocity). As a consequence, there is a competition within TELEMAC2D depth-averaged formulation, between increase flow and reduced sediment-friction, to mobilise and then transport sediments. While TELEMAC2D can model wetting and drying of the beach by the tide, surge and SLR, the ~40 m horizontal grid resolution is not able to fully represent detailed changes in the intertidal zone.

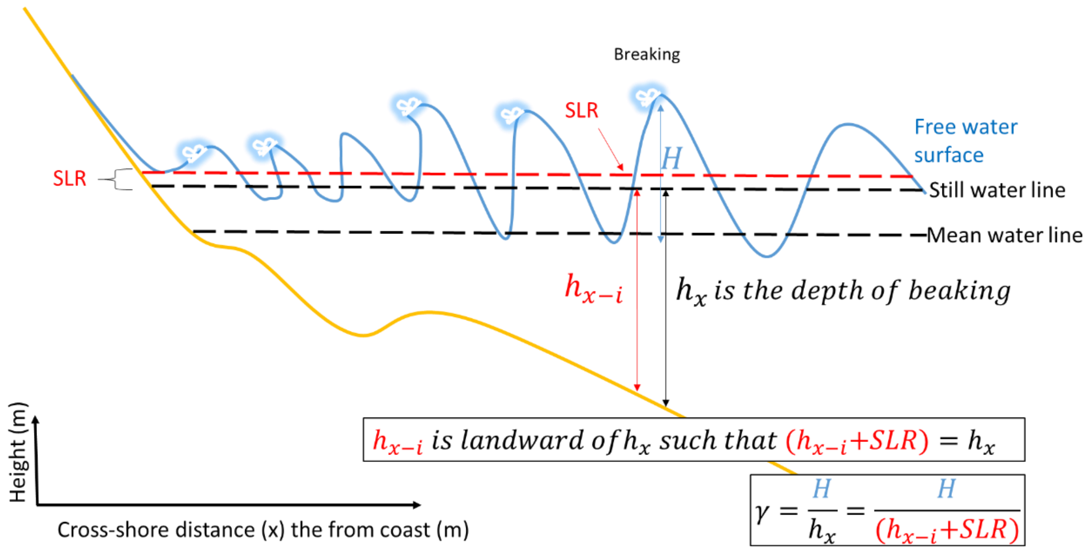


**Figure 7.1 Cross-shore diagram of the modelled impact of sea level rise on breaking.**

The position x in the cross-shore direction where wave heights $H$ (blue) break for a given depth ($h_x$) will move landward to $x$-$j$ under the influence of the increase in water level (SLR red dashed line) for an unchanged bathymetry. Diagram features corresponds to Figure 1.1.

Figure 7.2 shows a map of the changes in the net sediment transport $q_L\delta$ ($m^3m^{-1}$) in the longshore direction as a result of an increase in sea level (first two sensitivity runs). Longshore bedforms interact with the transport and show an alternating red/blue change in the longshore direction. The increase in sea level results in an eastward (coloured red) shift in the transport in waters around the 12m-depth contour. This eastward shift is a small reduction in the baseline net longshore transport westward (Figure 6.11). In waters shallower than 12 m there is a westward shift (coloured blue) in the baseline westward transport, resulting in an increase in the baseline westward transport. The changes in longshore transport show a complicated pattern of change near the ebb-tide delta, called ‘The Bar’. Overall, the transport changes are small compared to the baseline hindcast transport.

A large change is mapped in the southeast corners of Figure 7.1. This change occurred during the largest storm event (Table 6-1) when there was large circulation in the domain from the 6 m waves influencing the boundary flow conditions. This boundary inaccuracy is small compared to the baseline transport change (Figure 6.11).

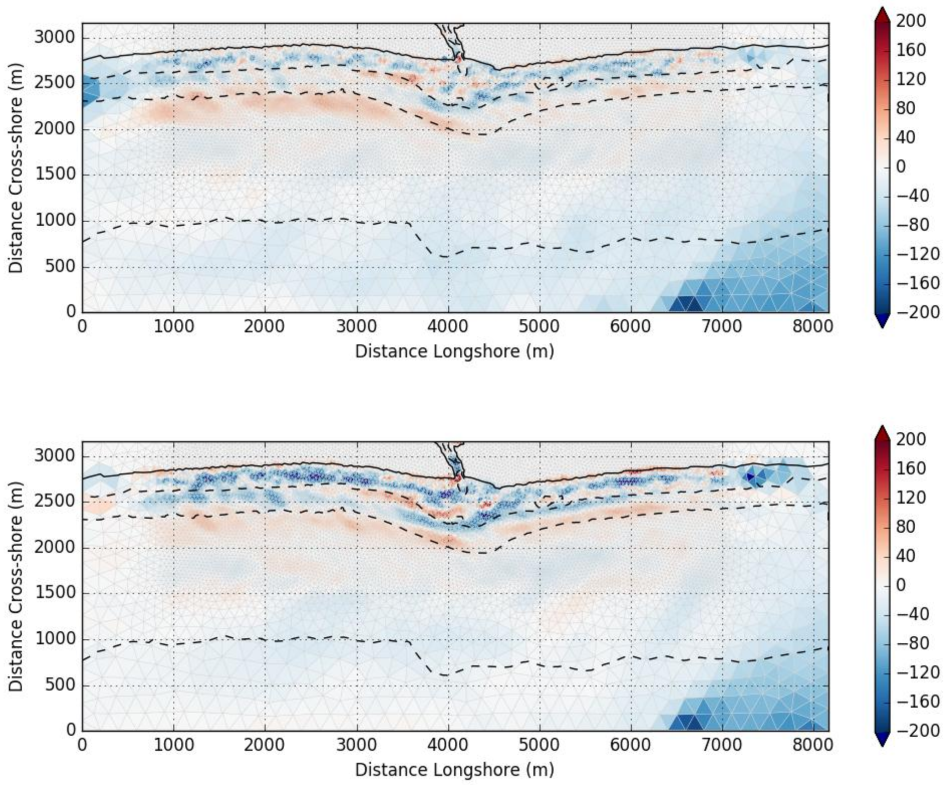


**Figure 7.2 Map of the sea level induced, change in net sediment transport $q_L\delta$ ($m^3m^{-1}$) in the longshore direction, over the TELEMAC climate sensitivity simulations.**

The top (bottom) plot shows the difference between the 0.1 m (0.2 m) increase in sea level CF simulation and the baseline simulation. The red (blue) coloured positive (negative) values are longshore sediment transport difference from the baseline (Figure 6.11), in the eastward (westward) direction. Longshore (cross-shore) direction on the horizontal (vertical) axis.

The time series of baseline, net longshore sediment transport ($m^3$) climate (Figure 6.12), is replotted with the five climate sensitivity runs in Figure 7.3. The two simulations with increased sea level (SL 0.1 m and 0.2 m), show little difference to the baseline TELEMAC simulation. The final net longshore sediment transport value from these climate sensitivity simulations is compared to the baseline in Table 7-2. The 0.1 m (0.2 m) increase in sea level results in a 1.3% (2.1%) increase in the net westward longshore transport. These values include the inaccurate transport at southeast boundary of the model domain (Figure 7.2).

**Table 7-2 GCM ensemble-mean CF climate simulations, percentage change from baseline.**

The percentages are calculated as CF future climate ($F_A$) simulation, less the baseline climate ($B_A$), divided (normalised) by the baseline. $[F_A - B_A]/B_A$. Values are based on ensemble mean CF (Table 7-1).

| Net Transport change CF method (%) | Change variable | TELEMAC | CERC | NMB-LM |
|---|---|---|---|---|
| ~3.7 yr Bathymetric survey Datasets | Wave CF | -53.1% | -49.0% | -46.6% |
| | Wave & Current CF | -54.1% | - | -45.5% |
| | Wave, Current SL+0.1 m CF | -52.4% | - | - |
| | SL+0.1 m | 1.3% | - | - |
| | SL+0.2 m | 2.1% | - | - |
| ~30 yr hindcast Dataset | Wave CF | - | -42.5% | -55.7% |
| | Wave & Current CF | - | - | -53.4% |
| | Wave, Current & SL+0.1 m CF | - | - | - |
| | SL+0.1 m | - | - | - |
| | SL+0.2 m | - | - | - |

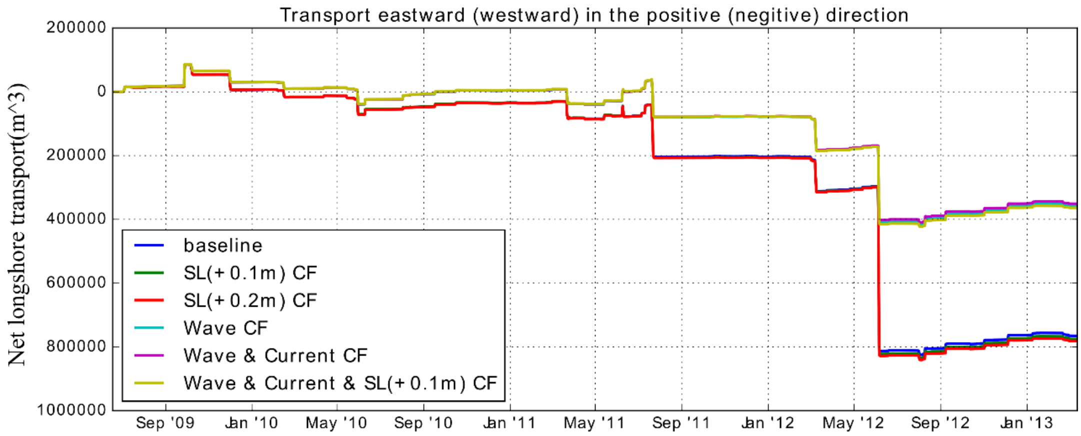


**Figure 7.3 Time series of net longshore transport $Q_{T}\delta$ (m$^3$) from different TELEMAC downscaled climate change factor (CF) forcing.**

This plot has the same format as Figure 6.12. The legend indicates which change factor (CF) sensitivity forcing has been applied, along with the baseline transport. SL is the sea level increase (0.1 or 0.2 metres).

The difference between the net longshore transports (m$^3$) modelled for the increased SL climate sensitivity runs and the baseline run is show in Figure 7.4. The two SL climate sensitivity runs show nonlinear changes during individual storm events. In other words, the increase from the 0.1 m to the 0.2 m SL simulation, does not inevitably result in exactly twice as much sediment transport.

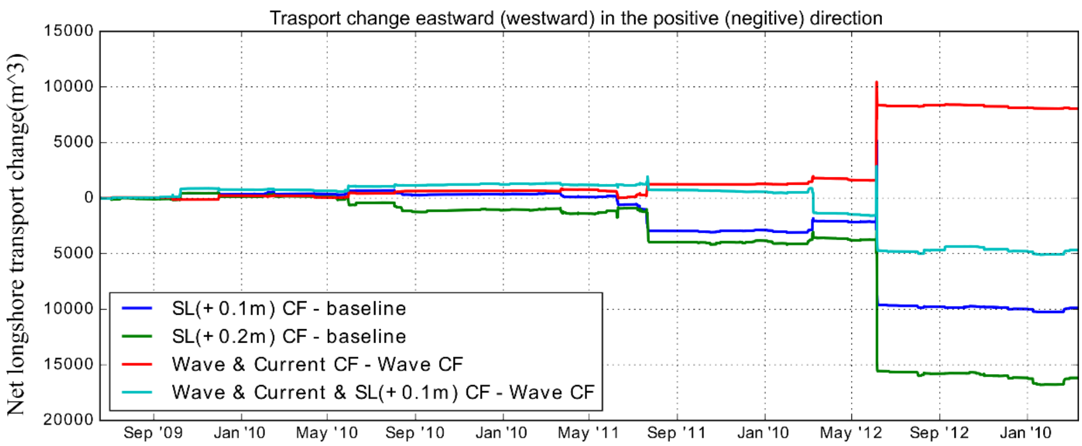


**Figure 7.4 Time series of difference in net longshore transport (m$^3$) from different TELEMAC downscaled climate change factor (CF) forcing.**

Plotted are the sea level (SL) Change Factor (CF) climate sensitivity simulations, relative to the baseline simulations. The climate sensitivity simulations with a wave CF are plotted relative to the wave CF data.

## 7.2 Impact of Wave Transport Changes

Prior to analysing the wave transport change, the wave-transport-directional CF was first checked for correctness (Section 3.6.5). The CERC-derived wave transport climate modelled with the wave-transport-directional CF in Equation 3-33, resulted in the same wave transport climate modelled with the GCM identified normalised wave transport anomaly (Figure 4.8) and Equation 3-34, confirming the wave-transport-directional CF can account for the GCM-derived changes in wave transport. In other words, it can account for the added dependence in the changes in wave height. Also, the wave CF factor applied to the NMB-LM equation and then used to rotate the TELEMAC directional spectrum resulted in similar wave change climates.

The ~30 yr CERC-derived transport climate is displayed in Figure 4.4. The CF is a clockwise shift in direction toward eastward transport (more westerly wave energy), for all months besides March (Table 7-1). The review of the top hindcast storm events (Table 6-1) indicates that the top storm event (2012-06-04), occurred in the month with the largest CF. Four of the top 30 events occurred during March when the wave-transport CF is westward. Figure 7.5 shows a map of the CF effect from the wave transport change. Between depths of around 2 m to 13 m, there is an eastward increase, in the baseline eastward transport. There is a shadow region of minimal transport change on the left (west) side of ebb-tide-delta (The Bar). This is the leeward side of baseline-westward-transport. So, while other parts of the coastline are predicted to receive reduced westward transport, west of The Bar transport is predicted to remain the same.

The time series of net longshore sediment transport ($m^3$) with the wave CF climate sensitivity runs show large differences to the baseline simulation (Figure 7.3). The TELEMAC wave CF simulation predicted that there would be a 51.1% decrease in net westward longshore transport (Table 7-2). Over the same period the CERC and NMB-LM predicted a similar 49% and 46.6% decrease respectively. The model ensemble prediction is around 50% decrease in westward longshore transport.

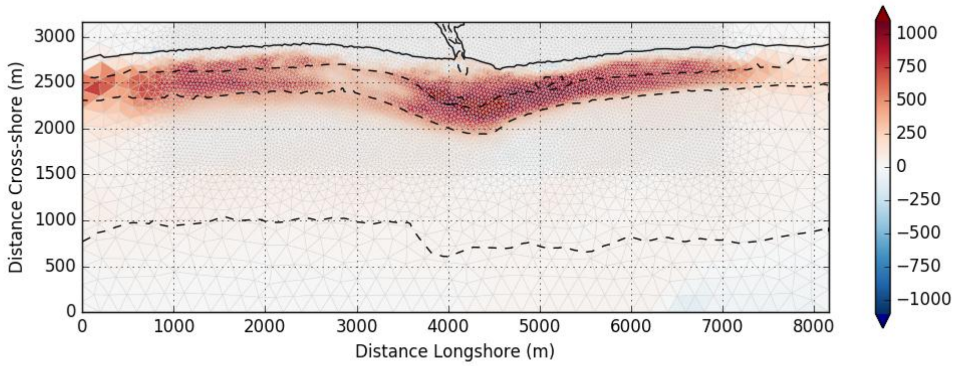


**Figure 7.5 Map of the wave CF induced change in net sediment transport $q_L\delta$ ($m^3m^{-1}$) in the longshore direction over the TELEMAC climate sensitivity simulations.**

This plot has the same format as Figure 7.2 but is for the influence of wave-transport-directional CF (not increased SL) boundary simulations.

The empirical equations were used to estimate the ensemble model spread from the different GCM-derived wave transport changes (Figure 4.8 b). Table 7-3 lists the projected future changes relative the 20 yr hindcast baseline. The HadGEM2-ES predicts the largest change (95.7%), and the INMCM4 (-14.5%) the smallest change, but all projections suggest a decrease in the baseline westward transport.

**Table 7-3 GCM four-member, wave CF simulation change from the baseline.**

Empirical estimates of wave-directional-transport CF for each of the four GCM derived transport change (Figure 4.8 b). The final column is the Empirical estimate with a single annual CF. Negative values indicate a decrease in the baseline westward transport.

| | HadGEM2-ES | ACCESS1.0 | CNRM.CM5 | INMCM4 | Single CF annual |
|---|---|---|---|---|---|
| CERC | -62.9% | -45.8% | -45.0% | -16.5% | -37.4% |
| NMB-LM | -95.7% | -59.3% | -51.2% | -14.5% | -41.6% |

Over the 20 yr hindcast period the ensemble mean CERC and NMB-LM equations predict a 42.5% and 55.7% decrease respectively (Table 7-2). This is similar to the 20 yr climates, and could suggest that the length of the TELEMAC simulations are long enough to capture the change projection. Further investigation into the monthly contribution to the annual change value is provided in Table 7-4. In the ~3.7 yr climate June is the dominant contributor to the annual change. This is true for the 20 yr climates, although these contribution to annual change are not as large. The CERC and NMB-LM equations predict 37.4% and 41.6% decreases with an average annual CF (Table 7-3). However, an average annual CF is not advisable, considering the seasonal changes that were identified in Chapter 4.

**Table 7-4 Monthly-contribution to annual wave CF forced climate change.** The percentages are the monthly wave-CF change contribution to annual wave-CF change in net longshore sediment transport ($m^3$) values. Values are calculated as future monthly wave-CF climate ($F_m$) less the baseline monthly climate ($B_m$), divided by the difference in the annual future wave CF climate ($F_a$) annual baseline ($B_a$), i.e. $[F_m - B_m]/[F_a-B_a]$. The positive (negative) values are westward (eastward) contributions to the annual westward transport.

| **Month** | Jan | Feb | Mar | Apr | May | Jun | Jul | Aug | Sep | Oct | Nov | Dec |
|---|---|---|---|---|---|---|---|---|---|---|---|---|
| **Wave$\theta_\Delta$ (°)** | 1.1° | 3.7° | -7.3° | 3.1° | 6.8° | 11.0° | 7.9° | 8.9° | 6.6° | 4.1° | 5.9° | 3.6° |
| | From the 3.7 yr period year climate | | | | | | | | | | | |
| TELEMAC | 0% | 1% | 1% | 0% | 2% | 76% | 12% | 2% | 0% | 3% | 3% | 0% |
| CERC | 1% | 2% | -6% | 3% | 10% | 32% | 16% | 12% | 11% | 8% | 7% | 4% |
| NMB-LM | 0% | 1% | -8% | 1% | 5% | 67% | 14% | 5% | 9% | 2% | 2% | 1% |
| | From the 20 yr climate | | | | | | | | | | | |
| CERC | 1% | 4% | -11% | 5% | 9% | 27% | 16% | 15% | 12% | 6% | 9% | 6% |
| NMB-LM | 1% | 2% | -10% | 6% | 7% | 31% | 18% | 12% | 11% | 7% | 11% | 5% |

## 7.3 Combined Impact of Waves, Currents and Sea Level

The applied wave-transport-directional CF, has a much greater effect on model sensitivity, than the sea level or currents (Figure 7.3). The additional effect of currents and sea level display a small non-linear addition to the wave CF climate (Figure 7.4). The TELEMAC model shows a 1% increase in westward transport from the inclusion of currents (Table 7-2). Over the same period, the NMB-LM predicts a 1% decrease in the westward transport. Over the ~30 yr hindcast NMB-LM predicts a 2.3% decrease.

## 7.4 Discussion

In this chapter, the multi-model ensemble prediction of longshore transport change is presented. The drivers of change (waves, currents and sea level) are analysed separately to determine their possible contribution to the change. A short-validated dataset and long-extrapolated dataset are analysed to investigate their impact.

It is difficult to numerically model a steady sediment transport (and bed evolution) simulation over long time scales, because of cumulative errors. As a result, it is difficult to simulate the period of predicted gradual increased sea level rise by the end of the century (i.e. a 100yr simulation) to around 0.8-1.0 m predicted by high GHG future simulations. To stabilise the TELEMAC climate sensitivity simulations, the bathymetry was reset to the measured profiles to be consistent with the baseline simulations. The modelling here showed little impact (1-2% change) on the longshore transport, for relatively large changes in sea level (0.1 m, 0.2 m over ~3.7 years). These sea level changes are unlikely to cause separation of the seabed from the sea level. The nonlinear influence of the increase in sea level means it difficult to extrapolate these changes out to the end of the 21$^{st}$ century (0.8-1.0 m) levels.

Changes over the shorter modelled TELEMAC simulation period are similar to the CERC and NMB-LM climates for the same period and the longer hindcast period. However, analysis of the monthly contribution to the change suggests that shorter sediment transport simulations (3-5 yrs) are unable to accurately represent the longer climate (20 yrs) monthly change signal.

In Chapter 4, the time series of GCM-forced COWCLIP wave output, is dynamically downscaled to the study location with the CERC model. The resulting monthly change statistics are then used as a CF downscaling method in this chapter. The directional wave CF method was applied to the CAWCR hindcast, checked against the dynamically downscaled climate, and provided the same projected monthly transport climate results. The advantage that the CF method has over the dynamically downscaled method, is that the baseline variability, and representation of extremes, are better represented in the hindcast CF dataset than in the coarse resolution GCM datasets.

Wave height and wave direction climate variables can be analysed separately to downscale wave transport with the CF method. However, caution is required to ensure that the CF wave height is not independent from CF direction. In other words, large *Hs* change projections associated with waves that are directly onshore should not be used with large direction change projections associated with periods when *Hs* is small. The CERC equation provides a method of easily combining the two wave parameters into one. Downscaling the single CERC transport equation CF was done in this study by applying a wave-transport-directional CF value, which resulted in the same normalised transport change anomaly identified in the GCM analysis. The wave-transport-directional CF is different to a change in mean wave direction, as it takes into account changes in wave height to modify the longshore transport.

Longshore transport projections, for the Spanish coastline, provided an example of how the inter-model variability of wave height and direction variables, are accentuated in terms of the single CERC transport variable (Casas-Prat et al., 2016). The study of the Spanish coastline, demonstrates how dynamically downscaling regional wave climate simulations with SWAN, further accentuates model bias and inter-model variability. Future studies of NMB, which could involve downscaling projections of wave height and direction, would likely result in further GCM-derived inter-model variability than what was presented in this study.

A review of the effect of wave direction changes on longshore transport projections, for European coastlines, highlight the relatively large impact that small projected changes in wave direction can have on longshore transport (Charles et al., 2012 and references therein). The review for the French coastline (Charles et al., 2012), used multiple GHG GCM simulations, and indicated that the inter-model variability between models with the same GHG pathway, could be larger than, the variability of a single model with different GHG pathway simulations. Future studies of NMB, which could include downscaling simulations with different GHG pathways (which are not currently available), could provide an estimate of the uncertainty associated with different global GHG, socio-economic futures.

When CF boundary currents are included in the simulations there is only a very slight influence on net transport (Figure 7.4). There were small differences between the longshore flow calculated by TELEMAC and the NMB-LM equation. In the previous chapter, the TELEMAC2D-dervied flow is forced by the gradient in the prescribed boundary water levels and modified (constrained) by the inclusion of the alternating prescribed boundary currents setup (Figure 6.1a and b). Changing the water level gradient to simulate the longshore GCM current anomaly was not possible because there is a non-linear relationship (phase lag to slack tide) between the water level gradient and longshore current velocity. This highlights a major unforeseen challenge in the model nesting setup. Therefore, because the boundary flow cannot be fully prescribed (constrained) with the boundary nesting process, the true GCM longshore flow change signal is not captured within the TELEMAC simulations. It is conceivable that the NMB-LM does a better job of downscaling the longshore current CF, because of the hindcast calibration exercise to the alternating tidal currents. Nonetheless, the difference between the TELEMAC and the NMB-LM model prediction is small compared to the influence of wave-driven flow.

Long-term cross-shore transport was not analysed in the model setup. The model setup lack the physics capability to capture transport processes in wave direction, and processes within shallow waters less than 2 m, within 100 m of the shoreline. It follows, that coastline change was not modelled in this dissertation, but is slated for future work (see Chapter 9).

The analysis shows there is a shadow region of minimal transport change on the left (west) side of 'The Bar'. This is the leeward side of baseline-westward-transport. So, while other parts of the coastline are receiving reduced westward transport, west of 'the bar' transport remains the same. This could result in continued reduction in the amount of sediments in this shadow region, and could lead to further coastline retreat, which is already occurring, west of the inlet.

# 8. CONCLUSION

This chapter summarises the approach and findings of this thesis. By considering the three themes outline in the introduction (Section 1.5), the main points contained in the results chapters (Chapters 4, 5, 6 and 7) are brought together and synthesised in three subsections.

## 8.1 Climate Variability and Change

The hindcast datasets of winds, waves and currents presented in this study have been shown to validate well against measured data at the study site on NMB and have been used to provide a quantitative description of the wave and wind-driven current climates for NMB. The length of the hindcasts also provided an opportunity to investigate the annual to decadal variability of the wind, wave and current transport and their relationship to STR-L and ENSO in greater detail than could have been possible with the *in-situ* data alone.

The eastward annual net mean direction of wind and currents opposes the annual net mean wave transport, which is westward. However, the yearly anomalies of all three parameters are typically in the same direction. The correlation coefficient between the normalised monthly waves and STR-L was considerably lower compared to the correlation of winds and wind-driven currents. This suggests that wave changes (including swell) are influenced by larger scale changes over the Southern Ocean and Tasman Sea than just local changes in the STR-L. Filtered monthly anomalies suggest that there may be a connection between SOI and the transport variables on multiyear timescales. During prolonged periods of negative (positive) SOI values the STR is located north (south) of its mean monthly position and the transport anomalies tend to be eastward (westward) of the mean. This may suggest that future changes to ENSO could influence long-term coastal dynamics in this region. Although it is noted that a more detailed analysis is necessary to comment on a possible forcing mechanism related to ENSO. At present, there remains uncertainty in how the ENSO signal will change into the future based on projections from the latest generation of GCMs (Grose et al., 2014).

There is some agreement between the four models of a projected change in the seasonal cycle (Figure 4.8) that tends to enhance the westward transport in summer. Little change is apparent for the eastward wind and wind-driven-current transport in winter. This asymmetry in projected change over the season implies that there is not a linear mean shift in the annual climate. In other words, the common practice in impact studies of simply perturbing the current climate by applying an annually-averaged change is not advisable.

The use of multiple climate models provides a range of plausible climate futures (Whetton et al., 2012) where the most likely outcome could be considered to sit near the ensemble mean. However the small ensemble size of models investigated here increases the uncertainty in the projected changes. Therefore for impact studies, it is important to consider the whole range of possible futures spanned by the results of this four-member ensemble. Indeed, utilising as large a number of GCMs to force the wave and hydrodynamic models as possible is important to better characterise the uncertainty in future climate projections.

This study highlights that potentially large changes in climate can occur in locations that lie at the boundaries of major circulation features, which are projected to undergo future shifts in location. In this study the change in mean transport, of the order of 45% of the baseline internal variability (Figure 4.8) for the transport due to wind and wind-driven currents during summer months is suggested to be as a result of the 0.59° southward movement of the STR bringing more easterly winds during summer. This connection to a large-scale climate feature is potentially significant in terms of the possible physical coastal changes that may ensue.

The TELEMAC coastal area-type model, CERC and new NMB-LM coastline-type models, predict a similar annual net longshore sediment transport of 200,000 $m^3yr^{-1}$ westward over the bathymetric survey period. Over the longer ~30 yr wave and hydrodynamic hindcast period CERC predicts similar annual transport, however, the NMB-LM predicts around half of the transport, ~100,000 $m^3yr^{-1}$. This is a similar value to one used in the dredging program used by the local port authority (GHD, 2013).

The downscaled sediment transport modelling predicts around a 50% (±40%) decrease in the westward net longshore sediment transport. The TELEMAC sediment transport climate simulations, predict a non-linear effect to increases in water levels (0.1 and 0.2 m). The sensitivity of the climate projections from the influence of increased sea level, results in only a 1-2% change.

Projected changes to wind-driven currents also resulted in a 1-2% change in the future projection of transport.

The main driver of this change is from the influence of wave-driven transport changes. The contribution from individual months was also shown to be important. While large normalised current change was captured in Chapter 4, particularly in summer months, the change associated with waves during the largest winter storms drive the overall transport climate. It is therefore difficult to associate the winter STR-L position, with the transport change.

A big focus of this dissertation was on the contribution of wind-driven currents to total transport. The TELEMAC modelled transport rates presented are dependent on wind-tide-driven currents. However the climate analysis showed small sensitivity (1-2%) from the timing, or normalised change, from the wind-driven currents. This study provides evidence, of the weak secondary importance of wind-driven currents, compared to the dominant wave-driven transport, in analysing the average sediment transport climate at NMB.

## 8.2 Morphology and Morphodynamic Measurements

In this thesis, an overview of the physical characteristics of NMB was developed by:

1) Reviewing the literature of the geological past of NMB (Section 2.2).
2) Compiling sediment-sampling data from historical field studies (Section 3.1.5).
3) Analysing the recent bathymetric surveys (Chapter 5).

The analysis of bathymetric surveys provided a measurement of the bed evolution and sediment transport morphological parameters. The large-scale survey and repeat surveys provided the spatial and temporal variability of NMB cross-shore profile respectively. Previous studies have focused on the inner surf zone (within ~100 m of the coast), where waves break every day, and there is day-to-day morphodynamic variability (Wright et al., 1982). The repeat survey measurements presented in this study, which were conducted months apart, demonstrates the variability of larger scale morphodynamic bedforms, controlled by storms. The whole of NMB LiDAR survey could present the variability that has formed over longer timescales.

Bed elevation analysis of the whole NMB coastline, indicates a large storm-bar and trough was present for the entire coastline, at the time of the survey. The storm-bar and trough was more pronounced at the eastern end of NMB compared to the western end. Bed elevation analysis of repeat surveys, at two locations near the eastern end of NMB, indicate the storm-bar and trough can be dissipated, only to reform a number of months later.

The location of storm-bar and trough is in the same position for the entire NMB coastline. It is roughly between the 2 m and 5 m depth contours and around 100 m and 300 m off the shoreline

(Figure 5.2). At greater depths, the 12 m, 15 m, 20 m contours are closer to the coastline in the eastern end and further away to the western end of NMB. The repeat surveys show little elevation changes at these depths near Lakes Entrance.

Therefore, the repeat surveys indicate that the temporal variability of the storm-bar and trough (2-5 m depth) are controlled by storms, on month-to-month time scales. The repeat surveys indicate not change in bed evolution between the 6-20 m depth contours at lakes entrance and could indicate that the spatial variability in the large-scale NMB LiDAR survey between 6-20 m depths, are controlled by longer time scales than storms (decadal to millennial and longer).

At both multi-beam survey sites, dunes were identified to be moving in the longshore direction between the 11-16 m depth contours (Figure 5.7). The dunes were also sometimes grouped on the seaward side of larger sandwaves in deeper water. Bedform tracking indicated that both survey sides tend to agree on the direction of transport. The west survey predicts more transport than the east. This could be a result of the dredge material or the interference of the large ebb-tide-delta separating the sites interfering with the longshore flow.

The dune bedforms provided an opportunity to measure sediment transport by approximating the stoss-to-lee transport (depending on flow direction) and bedform movement. Capturing the location of the crest of the somewhat-regular shaped bedforms and tracking them to the next survey provides a plausible indication of transport direction. However, it provides an inexact estimate of the magnitude of transport, particularly in an irregular flow field, which is a mixture of breaking waves, wind-tide-driven flow. Suspended sediment transport, which can be separated from the stoss-to-lee bedform transport, may lead to bedform elevation changes that are not a result of the assumed stoss-to-lee bedform process.

## 8.3 Sediment Transport Models

There are numerous sediment transport models available in the public domain. In this study of longshore sediment transport the simple coastline-type model, the CERC equation, and a detailed coastal area-type model, TELEMAC were investigated. The models resolve transport in different ways, yet came to similar conclusions on the net longshore sediment transport. The TELEMAC model configuration presented shows the importance of the contribution of storm events to transport. The CERC equation estimates more transport during the period between storms.

The scientific evidence provided by the TELEMAC model delivers a dynamical insight into when and where the transport occurs using the equation of Soulsby-Van Rijn (Equation 3-21). The more extensively validated CERC equation against empirical measurements, provides it with some credibility in the results provided. An import aspect of the TELEMAC sediment transport modelling was the representation of viscosity and diffusivity. While the 40m grid resolution allowed for a low horizontal hydrodynamic diffusivity (eddy viscosity), in the surf zone there is significant vertical eddy diffusivity as well as increased kinematic viscosity due to sediments in the water column. The calibration of predicted and measured bed evolution presented and the formulation of the Soulsby-Van Rijn equation provide some evidence of the magnitude of viscosity and diffusivity and their possible contribution to modelling transport in the surf zone (Section 3.6.4). But there are other significant improvements that can be made to the numerical modelling which are discussed in the next section (Chapter 9).

Coastal area-type models (e.g. TELEMAC or DELF3D), applied to the nearshore zone, require high resolution (tens of metres) to resolve the sharply changing bathymetry, so can only cover a small domain (kilometres wide). Therefore, coastal area models need a method of model-nesting within larger circulation simulations. This study developed a methodology of nesting within hindcasts, and downscaling GCM projections to the nearshore. Alternative methods of boundary configuration are possible. Consideration must be given on the type of downscaling, and what contribution they will make to the climate statistics.

The new NMB-LM extrapolates the TELEMAC, storm-dominated transport estimates, to the longer ~30 yr hindcast. It shows that the shorter survey period had a higher storm climate, and hence twice as large net longshore sediment transport climate. The CERC equation does not pick up this difference in climate.

Validation of the forcing waves and hydrodynamics hindcast were provided at an offshore location. Bed evolution was validated in the location of the storm-bar and trough (Figure 6.8). The bedform tracking measurements in Section 5.2.2, provides a plausible indication of the direction of longshore sediment transport, but differs by a two orders of magnitude, and shows no correlation to the modelled transport magnitude. Model accuracy/uncertainty was further investigated by model sensitivity runs. Depth-induced wave breaking was shown to be a key tuning parameter in modelling where transport occurred, and how large the transport was. However, other less obvious or studied parameters, e.g. relating to the sediment properties in the transport equation, could significantly alter the results. In the next section, the focus turns to what else is required to model transport change and future work.

# 9. FUTURE RECOMMENDED WORK

The longshore transport climate variability is dominated by wintertime wave-driven effects, which includes swell waves from the Southern Ocean and Tasman Sea. Future work is required to link the wintertime storm climate with climate indices, e.g. STR-L, SAM and SOI. The connection between the longshore transport climate indices, and how they change in GCM projections, may provide insight into how global changes will impact the local scale environment. There are a number of downscaling methods available to get the global dynamics to the nearshore zone. The advantages or disadvantages of each method are not directly apparent, and future work is required to assess each of the methodologies.

Sediment transport models have been applied to the nearshore coastal region since the 1980s. Today, there are a number of advanced PDE-based coastal area-type models, which are available to model sediment transport. Possible future additions to these models, are Lagrangian flow coordinates or adaptive grid-mesh. Arguably, more development is required on sub-grid scale parametrisations. This requires more empirical measurements which further highlights the need for continued measurements for the dredging program at Lakes Entrance.

Some important sub-grid scale parameterisations not completely addressed in this thesis are:

1) *Bathymetric slope* is critically important in determining depth-induced wave breaking, the wave-driven force applied to the hydrodynamics (Longuet-Higgins and Stewart, 1964) and the resulting sediment transport. Bathymetric slope should therefore be considered in empirical transport equations (e.g. Kamphuis, 1991; Le Méhauté and Koh,

1967). As with the NMB-LM model presented in this thesis, empirical equations are tested at one location with a single bathymetric slope. Work to test and compare equations at different locations, with differing bathymetric slopes, is required to capture its effect on internal model variability.

2) *Wave asymmetry / skewness* of individual waves can generate flow, and transport sediments in the wave direction (onshore or offshore) (Nielsen and Callaghan, 2003; Van Rijn *et al.*, 2013). They can also generate wave streaming. The shape of waves has been shown to be non-linearly dependant of ripple bedforms, which are difficult to model. The publicly available DELFT3D model appears to be further advanced in modelling these processes.
3) *Bottom roughness* was modelled with multiple coefficients and formulations by scientific-literature conventions in this study. Further work is required to bring a more consistent relationship between: the drag on the flow, the drag on the waves, drag on the sediment. Formulation would need to consider the internal model sensitivity to friction from ripple bedforms (Davies and Villaret, 1999; Nielsen, 2006; Smith et al., 2011; Villaret et al., 2011)
4) *Viscosity and diffusivity* represents a sub grid scale processes in numerical models, and vary significantly across the domain and with increasing wave action. Consideration is required to adequately represent the large amount of turbulence in the surf zone (van Rijn, 2013; Wright *et al.*, 1986).
5) *Sediment transport rate* calculated with the Soulsby-Van Rijn formulation contains many exponent-coefficients within the equations, which could significantly influence the internal model variability. This is true of most sediment transport rate formulations. Further measurements are required to validate, and provide certainty for these coefficients.

The inclusion of 3D hydrodynamics (TELEMAC3D), phase-resolved wave modelling (e.g. SWASH model), and using the tracer equation for suspended sediment concentrations, could better resolve the flow dynamics than the model setup provided in this thesis. On the other hand, the complex sub-grid scale processes in the nearshore region listed above will generally remain, and consideration must be given to the additional computational expense.

Bringing together the modelling improvements, the ultimate aim is to be able to model complex, long-term, decadal sediment transport simulations and to run models that are able to resolve the variability and change, in the advance or retreat of the coastline position.

# References

Aagaard T, Sørensen P. 2013. Sea level rise and the sediment budget of an eroding barrier on the Danish North Sea coast. *12th International Coastal Symposium* (65): 434–439. DOI: 10.2112/SI65-074.1.

Anandhi A, Frei A, Pierson DC, Schneiderman EM, Zion MS, Lounsbury D, Matonse AH. 2011. Examination of change factor methodologies for climate change impact assessment. *Water Resources Research* **47**(3): 1–10. DOI: 10.1029/2010WR009104.

Barnard P, Erikson L. 2012. Analyzing bedforms mapped using multibeam sonar to determine regional bedload sediment transport patterns in the San Francisco Bay coastal system. *Int. Assoc. Sedimentol. Spec. Publ* **44**: 273–294.

Battjes J, Janssen J. 1978. Energy loss and set-up due to breaking of random waves. *Proc. 16th Int. Conf. Coastal Eng* (1).

Bayram A, Larson M, Hanson H. 2007. A new formula for the total longshore sediment transport rate. **54**: 700–710. DOI: 10.1016/j.coastaleng.2007.04.001.

Benoit M, Marcos F, Becq F. 1996. Development of a third generation shallow-water wave model with unstructured spatial meshing. *Coastal Engineering Proceedings* 465–478.

Bird E. 1978. *The geomorphology of the Gippsland Lakes region*. Victorian Ministry for Conservation.

Bird ECF. 1994. Coastal Lagoon Processes, Chapter 2: Physical Setting and Geomorphology of Coastal Lagoons. *Elsevier oceanography series*, 9–39. DOI: 10.1016/S0422-9894(08)70007-2.

Bishop W, Womersley T. 2014. *Report 5: Coastal Monitoring: Gippsland Lakes/90 Mile Beach Local Coastal Hazard Assessment Project*. .

Black K, Rosenberg M, Hatton D, Colman R, Symonds G, G. RS, Pattiaratchi C, Nielse P. 1991. Hydrodynamic and sediment dynamic measurements in eastern Bass Strait In In situ sediment transport measurements: field data collection and analysis. *Victorian Institute of Marine Sciences* **3**(22).

Black K, Rosenberg M, Symonds G, Simons R, Pattiaratchi C, Nielsen P. 2013. Measurements of the Wave, Current and Sea Level Dynamics of an Exposed Coastal Site. *Mixing in Estuaries and Coastal Seas* **50**: 29–58. DOI: 10.1029/CE050p0029.

Black KP, Oldman JW. 1999. Wave mechanisms responsible for grain sorting and non-uniform ripple distribution across two moderate-energy, sandy continental shelves. *Marine Geology*

**162**(1): 121–132. DOI: 10.1016/S0025-3227(99)00060-2.

Bosserelle C, Pattiaratchi C, Haigh I. 2011. Inter-annual variability and longer-term changes in the wave climate of Western Australia between 1970 and 2009. *Ocean Dynamics* **62**(1): 63–76. DOI: 10.1007/s10236-011-0487-3.

Bouws E, Komen GJ. 1983. On the Balance Between Growth and Dissipation in an Extreme Depth-Limited Wind-Sea in the Southern North Sea. *Journal of Physical Oceanography*, 1653–1658. DOI: 10.1175/1520-0485(1983)013<1653:OTBBGA>2.0.CO;2.

Brent RP. 2013. *Algorithms for minimization without derivatives*. Courier Corporation.

Bruun P. 1962. Sea-level rise as a cause of shore erosion. *The Journal of Geology* 76–92.

Buijsman MC, Ridderinkhof H. 2008. Long-term evolution of sand waves in the Marsdiep inlet. I: High-resolution observations. *Continental Shelf Research* **28**(9): 1190–1201. DOI: 10.1016/j.csr.2007.10.011.

Cartier A, Larroudé P, Héquette A. 2012. Comparison of Sediment Transport Models With In-Situ Sand Flux Measurements And Beach Morphodynamic Evolution. *Coastal Engineering Proceedings* **1**(33): 8187. DOI: 10.9753/icce.v33.sediment.19.

Casas-Prat M, McInnes KL, Hemer MA, Sierra JP. 2016. Future wave-driven coastal sediment transport along the Catalan coast (NW Mediterranean). *Regional Environmental Change* **16**(6): 1739–1750. DOI: 10.1007/s10113-015-0923-x.

Charles E, Idier D, Delecluse P, Déqué M, Cozannet G. 2012. Climate change impact on waves in the Bay of Biscay, France. *Ocean Dynamics* **62**(6): 831–848. DOI: 10.1007/s10236-012-0534-8.

Charteris A, Sjerp E. 2009. Geomorphological threats of climate change on the Gippsland coast. *Coasts and Ports 2009*.

Chelliah M, Ebisuzaki W, Weaver S, Kumar A. 2011. Evaluating the tropospheric variability in National Centers for Environmental Prediction's climate forecast system reanalysis. *Journal of Geophysical Research* **116**(D17): D17107. DOI: 10.1029/2011JD015707.

Chini N, Stansby P. 2015. Broad-Scale Hydrodynamic Simulation, Wave Transformation and Sediment Pathways. In: Nicholls RJ, Dawson RJ and Day (née Nicholson-Cole) SA (eds) *Broad Scale Coastal Simulation: New Techniques to Understand and Manage Shorelines in the Third Millennium*. Springer Netherlands: Dordrecht, 103–124. DOI: 10.1007/978-94-007-5258-0_3.

Christensen JH, Kumar Krishna K, Aldrian E, An S-I, Cavalcanti IFA, de Castro M, Dong W, Goswami P, Hall A, Kanyanga JK, Kitoh A, Kossin J, Lau N-C, Renwick J, Stephenson DB, Xie S-P, Zhou T. 2013. Climate Phenomena and their Relevance for Future Regional Climate Change Supplementary Material. In: *Climate Change 2013: The Physical Science Basis. Contribution of Working Group I to the Fifth Assessment Report of the Intergovernmental Panel on Climate Change [Stocker, T.F., D. Qin, G.-K. Plattner, M. Tignor, S.K. Allen, J. Boschung, A. Nauels, Y. Xia,.*

Church JA, Clark PU, Cazenave A, Gregory JM, Jevrejeva S, Levermann A, Merrifield MA, Milne GA, Nerem RS, Nunn PD, Payne AJ, Pfeffer WT, Stammer D, Unnikrishnan AS. 2013. *Sea Level Change. In: Climate Change 2013: The Physical Science Basis. Contribution of Working Group I to the Fifth Assessment Report of the Intergovernmental Panel on Climate Change*. Cambridge University Press, Cambridge, United Kingdom and New York, NY, USA. 1137.

Church J, White N. 2011. Sea-Level Rise from the Late 19th to the Early 21st Century. *Surveys in Geophysics* **32**(4–5): 585–602. DOI: 10.1007/s10712-011-9119-1.

Colberg F, McInnes KL, O'Grady JG, Hoeke RK. 2017. Atmospheric Circulation Changes and Their Impact on Extreme Sea Levels Around Australia. *In preperation*.

CSIRO, Bureau of Meteorology. 2015. *Climate Change in Australia Information for Australia's Natural Resource Management Regions: Technical Report, CSIRO and Bureau of Meteorology, Australia.* CSIRO and Bureau of Meteorology, Australia 222 pages. http://www.climatechangeinaustralia.gov.au/en/publications-library/technical-report/.

Dalrymple RA, MacMahan JH, Reniers AJHM, Nelko V. 2011. Rip Currents. *Annual Review of Fluid Mechanics* **43**: 551–581. DOI: 10.1146/annurev-fluid-122109-160733.

Davies AG, Villaret C. 1999. Eulerian drift induced by progressive waves above rippled and very rough beds. *JOURNAL OF GEOPHYSICAL RESEARCH,* **104**: 1465–1488.

Duffy G, Hughes-Clarke J. 2012. Measurement of Bedload Transport in a Coastal Sea Using Repeat Swath Bathymetry Surveys: Assessing Bedload Formulae Using Sand Dune Migration. *Int. Assoc. Sedimentol. Spec. Publ.* **44**: 249–272.

Duffy GP, Hughes-Clarke JE. 2005. Application of spatial cross correlation to detection of migration of submarine sand dunes. *Journal of Geophysical Research* **110**(F4): F04S12. DOI: 10.1029/2004JF000192.

Durrant T, Greenslade D, Hemer H, Trenham C. 2014. *Global Wave Hindcast focussed on the Central and South Pacific*. CAWCR Report, 070.

Eldeberky Y, Battjes JA. 1995. Parameterization of triad interactions in wave energy models. *Coastal Dynamics 1995*, 140–148.

Fandry C. 1983. Model for the three-dimensional structure of wind-driven and tidal circulation in Bass Strait. *Marine and Freshwater Research* **34**(1): 121–141. DOI: 10.1071/MF9830121.

Fowler HJ, Blenkinsop S, Tebaldi C. 2007. Linking climate change modelling to impacts studies: recent advances in downscaling techniques for hydrological modelling. *International Journal of Climatology* **27**(12): 1547–1578. DOI: 10.1002/joc.1556.

GHD. 2013. *Gippsland Lakes Ocean Access Program 2012 TSHD Maintenance Program Final*. Gippsland Ports.

Grose MR, Brown JN, Narsey S, Brown JR, Murphy BF, Langlais C, Gupta A Sen, Moise AF, Irving DB. 2014. Assessment of the CMIP5 global climate model simulations of the western tropical Pacific climate system and comparison to CMIP3. *International Journal of Climatology*. DOI: 10.1002/joc.3916.

Harley MD, Turner IL, Short AD, Ranasinghe R. 2010. Interannual variability and controls of the Sydney wave climate. *International Journal of Climatology* **30**: 1322–1335. DOI: 10.1002/joc.1962.

Harris P, Heap A, Passlow V, Sbaffi L, Fellows M, Porter-smith R, Buchanan C, Daniell J. 2005. *Geomorphic Features of the Continental Margin of Australia Geomorphic Features of the Continental Margin of Australia*. .

Hemer MA, Church JA, Hunter JR. 2009. Variability and trends in the directional wave climate of the Southern Hemisphere. *International Journal of Climatology* **30**: 475–491. DOI: 10.1002/joc.1900.

Hemer MA, Fan Y, Mori N, Semedo A, Wang XL. 2013a. Projected changes in wave climate from a multi-model ensemble. *Nature Climate Change*. Nature Publishing Group **3**(5): 471–476. DOI: 10.1038/nclimate1791.

Hemer MA, Katzfey JJ, Trenham CE. 2013b. Global dynamical projections of surface ocean wave climate for a future high greenhouse gas emission scenario. *Ocean Modelling*. Elsevier Ltd **70**: 221–245. DOI: 10.1016/j.ocemod.2012.09.008.

Hemer MA, McInnes KL, Ranasinghe R. 2013c. Projections of climate change-driven variations in the offshore wave climate off south eastern Australia. *International Journal of Climatology* **33**(7): 1615–1632. DOI: 10.1002/joc.3537.

Hervouet J-M. 2007. *Hydrodynamics of free surface flows: modelling with the finite element* *method*. John Wiley & Sons.

Holdgate GR, Wallace MW, Gallagher SJ, Smith AJ, Keene JB, Moore D, Shafik S. 2003. Plio-Pleistocene tectonics and eustacy in the Gippsland Basin, southeast Australia: evidence from magnetic imagery and marine geological data. *Australian Journal of Earth Sciences* **50**(2003): 403–426.

Holthuijsen LH. 2007. *Waves in oceanic and coastal waters*. Cambridge University Press. DOI: https://doi.org/10.1017/CBO9780511618536.

Houston JR, Dean RG. 2014. Shoreline Change on the East Coast of Florida. *Journal of Coastal Research*. The Coastal Education and Research Foundation.

IPCC. 2014. *Synthesis Report. Contribution of Working Groups I, II and III to the Fifth Assessment Report of the Intergovernmental Panel on Climate Change [Core Writing Team, R.K. Pachauri and L.A. Meyer (eds.)]*. Geneva, Switzerland.

Izumiya T, Horikawa K. 1984. Wave energy equation applicable in and outside the surf zone. *Coastal Engineering in Japan* **27**: 119–137.

Jones H, Davies P, Bladon G. 1983. *Superficial sediments of the Tasmanian continental shelf and part of Bass Strait*. Australian Government Publishing Service.

Kamphuis JW. 1991. Alongshore Sediment Transport Rate. *Journal of Waterway, Port, Coastal, and Ocean Engineering* **117**(6): 624–640. DOI: 10.1061/(ASCE)0733-950X(1991)117:6(624).

Kamphuis JW, Davies MH, Nairn RB, Sayao OJ. 1986. CALCULATION OF LITTORAL SAND TRANSPORT RATE. *Coastal Engineering* **10**: 1–21.

Katzfey J, McInnes K. 1996. GCM simulations of eastern Australian cutoff lows. *Journal of climate* **9**: 2337–2355.

Kent DM, Kirono DGC, Timbal B, Chiew FHS. 2011. Representation of the Australian sub-tropical ridge in the CMIP3 models. *International Journal of Climatology* **33**(1): 48–57. DOI: 10.1002/joc.3406.

Komar PD. 1971. The mechanics of sand transport on beaches. *Journal of Geophysical Research* **76**(3): 713. DOI: 10.1029/JC076i003p00713.

Le Méhauté B, Koh RCY. 1967. On The Breaking Of Waves Arriving At An Angle To The Shore. *Journal of Hydraulic Research* **5**(1): 67–88. DOI: 10.1080/00221686709500189.

Longuet-Higgins M, Stewart R. 1964. Radiation stresses in water waves; a physical discussion, with applications. *Deep Sea Research and Oceanographic Abstracts* **11**(4): 529–562.

Longuet-Higgins MS. 1970. Longshore currents generated by obliquely incident sea waves: 1. *Journal of Geophysical Research* **75**(33): 6778. DOI: 10.1029/JC075i033p06778.

McInnes KL, Erwin TA, Bathols JM. 2011. Global Climate Model projected changes in 10 m wind speed and direction due to anthropogenic climate change. *Atmospheric Science Letters* **12**(4): 325–333. DOI: 10.1002/asl.341.

McInnes KL, Hubbert GD. 2001. The impact of eastern Australian cut-off lows on coastal sea levels. *Meteorological Applications* **8**: 229–244.

McInnes KL, Hubbert GD. 2003. A numerical modelling study of storm surges in Bass Strait. *Australian Meteorological Magazine* **52**: 143–56.

Miche A. 1944. Mouvements ondulatoires de la mer en profondeur croissante ou decroissante. *Annales des Ponts et Chaussees* **144**: 369–406.

Mil-homens J, Ranasinghe R, Vries JSMVT De, Stive MJF. 2013. Re-evaluation and improvement of three commonly used bulk longshore sediment transport formulas. *Coastal Engineering*. Elsevier B.V. **75**: 29–39. DOI: 10.1016/j.coastaleng.2013.01.004.

Mitchell JK, Holdgate GR, Wallace MW. 2007. Pleistocene history of the Gippsland Basin outer shelf and canyon heads, southeast Australia. *Australian Journal of Earth Sciences* **54**(1): 49–64. DOI: 10.1080/08120090600981442.

Munk WH. 1949. The solitary wave theory and its application to surf problems. *Annals of the New York Academy of Sciences* **51**(3): 376–424. DOI: 10.1111/j.1749-6632.1949.tb27281.x.

Nelder JA, Mead R. 1965. A simplex algorithm for function minimization. *Computer Journal* **7**: 308–313.

Nicholls RJ, Larson M, Capobianco M, Birkemeier W a. 1998. Depth of closure: Improving understanding and prediction. *Proceedings of the Coastal Engineering Conference* **3**: 2888–2901.

Nielsen P. 1992. *Coastal bottom boundary layers and sediment transport*. World Scientific.

Nielsen P. 2006. Dynamics and geometry of wave-generated ripples. **86**(1): 6467–6472.

Nielsen P, Callaghan DP. 2003. Shear stress and sediment transport calculations for sheet flow under waves. *Coastal Engineering* **47**: 347–354.

Nikuradse J. 1933. Laws of flow in rough pipes. *VDI Forschungsheft* **361**(In translation, NACA TM 1292, 1950.).

O'Grady JG, McInnes KL. 2010. Wind waves and their relationship to storm surges in northeastern Bass Strait. *Australian Meteorological and Oceanographic Journal* **60**(4): 265–275.

Putzar B, Malcherek AM. 2012. Development of a long-term morphodynamic model for the German Bight. In: Bourban S, Durand N and Hervouet J-M (eds) *XIXth TELEMAC-MASCARET User Conference*. Oxford, UK, 47–52.

Ranasinghe R, McLoughlin R, Short A, Symonds G. 2004. The Southern Oscillation Index, wave climate, and beach rotation. *Marine Geology* **204**(3–4): 273–287. DOI: 10.1016/S0025-3227(04)00002-7.

Regression N. 1996. *Book Reviews Nonparametric Regression and Generalized Linear Models : A Roughness Penalty Approach*. .

Riahi K, Rao S, Krey V, Cho C, Chirkov V, Fischer G, Kindermann G, Nakicenovic N, Rafaj P. 2011. RCP 8.5—A scenario of comparatively high greenhouse gas emissions. *Climatic Change* **109**(1–2): 33–57. DOI: 10.1007/s10584-011-0149-y.

Riedel P, Sjerp E. 2007. *Erosion history of Ninety Mile Beach, Gippsland.* Report for Parks Victoria.

Roelvink D, Reniers A. 2011. *A guide to modelling coastal morphology*. World Sci., Singapore.

Russell K, Rennie J, Sjerp E. 2013. *Gippsland State of the Coast Update*. Report by Water Technology Pty. Ltd. for Gippsland Coastal Board.

Saha S, Moorthi S, Pan H-L, Wu X, Wang J, Nadiga S, Tripp P, Kistler R, Woollen J, Behringer D, Liu H, Stokes D, Grumbine R, Gayno G, Wang J, Hou Y-T, Chuang H-Y, Juang H-MH, Sela J, Iredell M, Treadon R, Kleist D, Van Delst P, Keyser D, Derber J, Ek M, Meng J, Wei H, Yang R, Lord S, Van Den Dool H, Kumar A, Wang W, Long C, Chelliah M, Xue Y, Huang B, Schemm J-K, Ebisuzaki W, Lin R, Xie P, Chen M, Zhou S, Higgins W, Zou C-Z, Liu Q, Chen Y, Han Y, Cucurull L, Reynolds RW, Rutledge G, Goldberg M. 2010. The NCEP Climate Forecast System Reanalysis. *Bulletin of the American Meteorological Society*. Research Data Archive at the National Center for Atmospheric Research, Computational and Information Systems Laboratory: Boulder, CO **91**(8): 1015–1057. DOI: 10.1175/2010BAMS3001.1.

Saint-Venant BD. 1871. Theory of unsteady water flow, with application to river floods and to propagation of tides in river channels. *French Academy of Science* **73**: 237–240.

Samaras AG, Gaeta MG, Miquel AM, Archetti R. 2016. High-resolution wave and hydrodynamics modelling in coastal areas: operational applications for coastal planning, decision support and assessment. *Nat. Hazards Earth Syst. Sci* **16**: 1499–1518. DOI: 10.5194/nhess-16-1499-2016.

Sandery PA, Kämpf J. 2007. Transport timescales for identifying seasonal variation in Bass Strait, south-eastern Australia. *Estuarine, Coastal and Shelf Science* **74**(4): 684–696. DOI: 10.1016/j.ecss.2007.05.011.

Shchepetkin AF, McWilliams JC. 2005. The regional oceanic modeling system (ROMS): a split-explicit, free-surface, topography-following-coordinate oceanic model. *Ocean Modelling* **9**(4): 347–404. DOI: 10.1016/j.ocemod.2004.08.002.

Short AD. 2006. Australian Beach Systems—Nature and Distribution. *Journal of Coastal Research* **221**(1): 11–27. DOI: 10.2112/05A-0002.1.

Sinclair MJ, Quadros N. 2010. Airborne Lidar Bathymetric Survey for Climate Change Airborne Lidar Bathymetric Survey for Climate Change. (April): 11–16.

Smith GA, Babanin A V., Riedel P, Young IR, Oliver S, Hubbert G. 2011. Introduction of a new friction routine into the SWAN model that evaluates roughness due to bedform and sediment size changes. *Coastal Engineering*. Elsevier B.V. **58**(4): 317–326. DOI: 10.1016/j.coastaleng.2010.11.006.

Soulsby RL. 1997. *Dynamics of marine sands*. Thomas Telford.

Splinter KD, Turner IL, Davidson MA, Barnard P, Castelle B, Oltman-shay J. 2014. A generalized equilibrium model for predicting daily to interannual shoreline response. *JournalofGeophysicalResearch: EarthSurface* 1936–1958. DOI: 10.1002/2014JF003106.Received.

Szmytkiewicz M, Biegowski J, Kaczmarek LM, Okroj T, Ostrowski R, Pruszak Z, Różyńsky G, Skaja M. 2000. Coastline changes nearby harbour structures: Comparative analysis of one-line models versus field data. *Coastal Engineering* **40**(2): 119–139. DOI: 10.1016/S0378-3839(00)00008-9.

Taylor KE, Stouffer RJ, Meehl G a. 2012. An Overview of CMIP5 and the Experiment Design. *Bulletin of the American Meteorological Society* **93**(4): 485–498. DOI: 10.1175/BAMS-D-11-00094.1.

Thom B. 1984. Transgressive and regressive stratigraphies of coastal sand barriers in southeast Australia. *Marine Geology* **56**(1983): 137–158.

Thompson DWJ, Solomon S. 2002. Interpretation of recent Southern Hemisphere climate change. *Science (New York, N.Y.)* **296**(5569): 895–9. DOI: 10.1126/science.1069270.

Tolman H. 2009. User manual and system documentation of WAVEWATCH III TM version 3.14. *Technical note, MMAB Contribution* (276).

Tomasicchio GR, Alessandro FD, Barbaro G, Malara G. 2013. General longshore transport model. *Coastal Engineering*. Elsevier B.V. **71**: 28–36. DOI: 10.1016/j.coastaleng.2012.07.004.

Tonk AM. 2004. Longshore sediment transport driven by sea breezes on low-energy sandy beaches, Southwestern Australia. https://dspace.lboro.ac.uk/2134/7644, Loughborough University.

Trenham CE, Hemer MA, Durrant TH, Greenslade DJM. 2013. PACCSAP Wind-wave Climate : High resolution wind-wave climate and projections of change in the Pacific region for coastal hazard assessments. *CAWCR Technical Report* (68): CAWCR Technical Report 068. 44 pp.

Troup A. 1965. The "southern oscillation." *Quarterly Journal of the Royal Meteorological Society* **91**: 490–506.

U. S. Army corps of Engineers. 1984. SHORE PROTECTION MANUAL - Volume I. *Coastal Engineering Research Center* **1**(4th ed., ed.2 Vol): 652. DOI: 10.5962/bhl.title.47830.

Van Der Westhuysen AJ. 2012. Spectral modeling of wave dissipation on negative current gradients. *Coastal Engineering*. Elsevier B.V. **68**: 17–30. DOI: 10.1016/j.coastaleng.2012.05.001.

Van Rijn L. 2007. Unified view of sediment transport by currents and waves. I: Initiation of motion, bed roughness, and bed-load transport. *Journal of Hydraulic Engineering* (June): 649–667.

Van Rijn L. 2014. A simple general expression for longshore transport of sand, gravel and shingle. *Coastal Engineering*. Elsevier B.V. **90**: 23–39. DOI: 10.1016/j.coastaleng.2014.04.008.

van Rijn L. 2013. *SIMPLE GENERAL FORMULAE FOR SAND TRANSPORT IN RIVERS, ESTUARIES AND COASTAL WATERS*. *www.leovanrijn-sediment.com*, 1–20.

Van Rijn L, Ribberink JS, van der Werf JJ, Walstra DJR. 2013. Coastal sediment dynamics : recent advances and future research needs. **51**(5): 475–493. DOI: 10.1080/00221686.2013.849297.

Villaret C, Hervouet J-M, Kopmann R, Merkel U, Davies AG. 2013. Morphodynamic modeling using the Telemac finite-element system. *Computers & Geosciences*. Elsevier **53**: 105–113. DOI: 10.1016/j.cageo.2011.10.004.

Villaret C, Huybrechts N, Davies AG, Way O. 2011. Effect of bed roughness prediction on morphodynamic modelling : Application to the Dee estuary ( UK ) and to the Gironde estuary ( France ). *34th IAHR World Congress*. Brisbane, Australia, 1149–1156.

Wandres M, Pattiaratchi C, Hetzel Y. 2017. The response of the southwest Western Australian wave climate to Indian Ocean climate variability. *Climate Dynamics*. Springer Berlin Heidelberg **0**(0): 1–25. DOI: 10.1007/s00382-017-3704-z.

Wheeler P, Peterson J, Gordon-Brown L. 2010. Flood-tide Delta Morphological Change at the Gippsland Lakes Artificial Entrance, Australia (1889–2009). *Australian Geographer* **41**(2): 183–216. DOI: 10.1080/00049181003742302.

Whetton P, Hennessy K, Clarke J, McInnes K, Kent D. 2012. Use of Representative Climate Futures in impact and adaptation assessment. *Climatic Change* **115**(3–4): 433–442. DOI: 10.1007/s10584-012-0471-z.

Wijeratne EMS, Pattiaratchi CB, Eliot M, Haigh ID. 2012. Tidal characteristics in Bass Strait, south-east Australia. *Estuarine, Coastal and Shelf Science*. Elsevier Ltd **114**: 156–165. DOI: 10.1016/j.ecss.2012.08.027.

Wong P, Lonsada I, Gattuso J, Hinkel J, Burkett V, Codignotto J. 2014. Coastal Systems and Low-Lying Areas - AR5. (October 2013): 1–85.

Wright L, Nielsen P, Shi N, List J. 1986. Morphodynamics of a bar-trough surf zone. *Marine geology* **70**(1233): 251–285.

Wright L, Short A. 1984. Morphodynamic variability of surf zones and beaches: a synthesis. *Marine geology* **56**(1135): 93–118.

Wright LD, Nielsen P, Short AD, Coffey FC, Green MO. 1982. Nearshore and surfzone morphodynamics of a storm wave environment : eastern Bass Strait, Australia (No. CSU-TR-82/3). Sydney Univ, Australian Coastal Studies Unit.

Young IR, Vinoth J, Zieger S, Babanin a. V. 2012. Investigation of trends in extreme value wave height and wind speed. *Journal of Geophysical Research* **117**: 1–13. DOI: 10.1029/2011JC007753.

# List of Publications

O'Grady JG, McInnes KL, Colberg F, Hemer MA, Babanin AV (2015) Longshore wind, waves and currents: climate and climate projections at Ninety Mile Beach, southeastern Australia. Int J Climatol 35(14):4079–4093

Abstract:

It is shown that Lakes Entrance, a township located at the northern end of Ninety Mile Beach in southeastern Australia, is situated in a region that may experience noticeable changes in longshore wind, wave and ocean currents compared to present day climate variability as a consequence of the southward shifting subtropical ridge (STR) predicted in global climate change models. These changes could modify sediment transport in the littoral zone and impact the coastline position. Thirty-year hindcasts of winds, coastal currents and waves are shown to agree well with available observations and provide a long-term dataset of the climate variability. Hindcasts of coastal ocean currents and waves indicate that while the annual net mean wave and current transport are in opposing directions, their seasonal adjusted monthly anomalies are positively correlated. Furthermore they are also correlated with the position of the STR location index. On seasonal to annual time scales a weak connection between the transport variables and Southern Oscillation Index (SOI) is found. It appears that during multiple years of positive (negative) SOI conditions the STR is located north (south) of its mean monthly position, resulting in anomalous eastward (westward) transport. The four climate models used in this study indicate a southward shift in the STR for most months under a high emission future. In summer months the shift in the STR results in both increased summer westward wind-driven currents and westward wave forcing. Changes in winter months are less related to the STR location and it is discussed that the contraction and increased intensity of the westerly storm belt linked to Southern Annular Mode could possibly influence the transport. The analysis is presented at the coastal scale to provide insights into how these changes may affect net transport across the littoral zone in more detailed numerical nearshore sediment transport modelling.